INAUGURAL - DISSERTATION

zur
Erlangung der Doktorwürde
der
Naturwissenschaftlich-Mathematischen Gesamtfakultät
der
Ruprecht-Karls-Universität
Heidelberg

vorgelegt von
Diplom-Mathematiker Sebastian Bönisch
aus München

Tag der mündlichen Prüfung: 20.12.2006

Adaptive Finite Element Methods for Rigid Particulate Flow Problems

Gutachter: **Prof. Dr. Rolf Rannacher**

Prof. Dr. Dr. h. c. mult. Willi Jäger

Abstract

Subject of this work is the numerical simulation of the motion of rigid particles in an incompressible viscous or viscoelastic fluid. What makes this task especially challenging is the fact that two different physical models are *coupled*: The fluid motion is described by a system of partial differential equations ('Navier-Stokes equations'), while the dynamics of the rigid particles is determined as the solution of a system of ordinary differential equations (Newton's laws of motion).

In this work, numerical methods for some prototypical situations are developed, analyzed and validated; all of them are based on the finite element method (FEM). In this context, special emphasis is given to local grid adaptation. The goal is to obtain a high accuracy and, at the same time, to keep the computational effort as low as possible.

Zusammenfassung

Gegenstand dieser Arbeit ist die numerische Simulation der Bewegung starrer Teilchen in einer inkompressiblen viskosen bzw. viskoelastischen Flüssigkeit. Die besondere Schwierigkeit ergibt sich hierbei daraus, daß zwei verschiedene physikalische Modelle miteinander *gekoppelt* sind: Die Bewegung der Flüssigkeit wird durch ein System partieller Differentialgleichungen beschrieben ('Navier-Stokes Gleichungen'), wogegen die Dynamik der starren Teilchen als Lösung eines Systems gewöhnlicher Differentialgleichungen gegeben ist (Newtonsche Gesetze).

Basierend auf der Methode der Finiten Elemente (FEM), werden in dieser Arbeit numerische Lösungsansätze für verschiedene prototypische Fälle entwickelt, analysiert und durch Beispielrechnungen validiert. Ein besonderer Schwerpunkt liegt dabei auf der Verwendung lokal adaptierter Gitter, um mit einem Minimum an Rechenaufwand eine größtmögliche Genauigkeit zu erzielen.

Contents

1 Introduction

The subject of this work is the numerical simulation of the motion of rigid particles in viscous liquids ('particulate flows') by means of the adaptive finite element method. The presence of the particles affects the flow of the liquid, and this, in turn, affects the motion of the particles. Particulate flows hence belong to the (much broader) class of so-called *fluid-structure interaction* problems. It is currently one of the major focal points of applied research to design numerical algorithms for simulating such problems in an accurate and efficient way. However, this is a very challenging task due to the fact that the combined motion of fluid and structure is described by highly coupled systems of differential equations.

In this first chapter we would like to motivate our study by introducing some selected problems of practical interest where particulate flows play a major role. Furthermore, we wish to describe the structure and the main results of this work.

As a matter of fact, the prediction of particle motion in liquids of different nature is a key issue in many fields of research, such as process (or chemical) engineering, medical sciences and biology/bionics. Let us collect some important examples (cf. Galdi [Gal01] and references cited therein):

① **Composite materials**
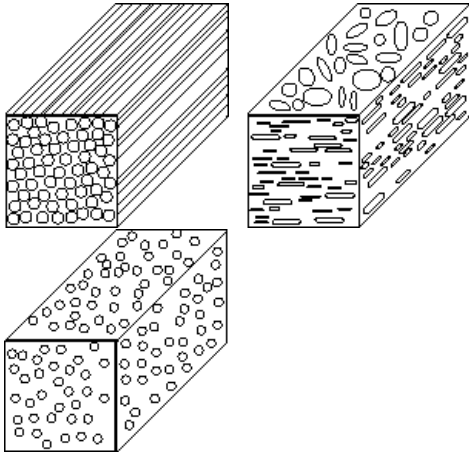
Figure 1.1:
Schematic view of some typical composite materials.

The addition of fiber-like particles to a polymer matrix (see picture on the left) is well-known to enhance the mechanical properties of the composite material: The matrix accepts the load over a large surface area and transfers it to the reinforcement which is stiffer and increases the strength of the overall material. Typical sizes of a fiber are a hundred micrometers in diameter and a centimeter in length. The degree of enhancement depends strongly on the *orientation of the fibers* and the fiber orientation is in turn caused by the flow occurring in the mold. Therefore, a better knowledge of the motion of fibers in polymer (viscoelastic) liquids is important for the design of molding equipment and determining the optimal processing conditions, see e.g. Lee et al. [LYH⁺97].

② Proppant transport in hydraulic fracturing applications

Hydraulic fracturing is often used to increase the productivity of a hydrocarbon well (see picture on the right). A slurry of sand in a highly viscous fluid is pumped into the well and exceeds, at sufficient pressure, the horizontal stresses in the rock. This opens a fracture, penetrating from the well bore far into the pay zone. When the pumping pressure is removed, the sand acts to prop the fracture open. Productivity is enhanced because the sand-filled fracture offers a higher-conductivity path for fluids to enter the well than through the bulk rock. For a successful stimulation job there must be a *continuous sand-filled path*. Furthermore, the sand must be placed within *productive formations*. Controlling and exploiting the proppant migration requires an understanding of the *relationship between fluid properties and particle migration* (see Joseph [Jos00] for more details).
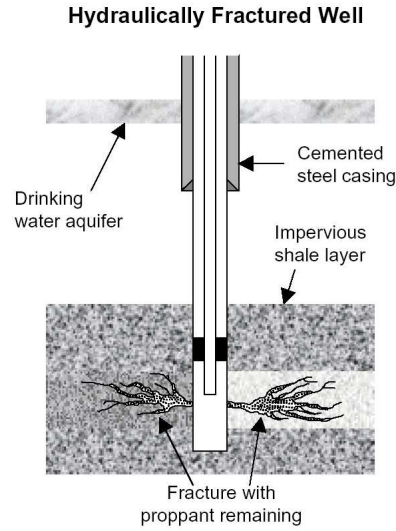

Figure 1.2:
Schematic view of a hydraulically fractured well.

③ Separation of macro-molecules by electrophoresis

Electrophoresis is a powerful separation technique in the biological sciences whose applications include weight determination of proteins, DNA sequencing and diagnosis of genetic diseases (see e.g. Trainor [Tra90]). Electrophoresis involves the motion of charged particles in
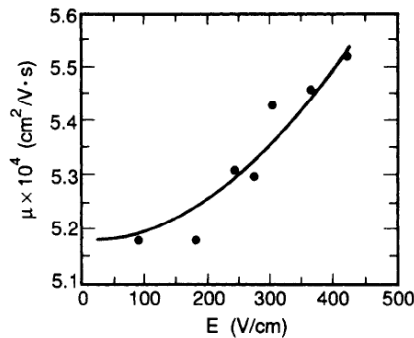
Figure 1.3:
Electrophoretic mobility of the TM virus vs. electrical field strength (see [GS90]).

solution, under the action of an electric field. Certain types of macromolecules are nearly perfectly symmetric and rod-shaped, like e.g. the Tobacco Mosaic Virus (TMV). The *orientation* of such molecules during electrophoresis plays an important role since it is responsible for the loss of separability. An interesting observation in this direction was made by Grossman/Soane [GS90]: They found that the electrophoretic mobility (particle velocity divided by field strength) increases with increasing strength of the electric field, see Figure 1.3. It turns out that this characteristic behavior can be explained by an *orientation effect*: With increasing field strength the virus becomes more and more aligned with the direction of motion. As a consequence, the drag is reduced and the virus is moving faster.

Other significant examples include the modeling of blood flow (see e.g. Schmid-Schönbein/Wells [SW69]), the understanding of locomotion of macroscopic objects (birds, fishes, airplanes

etc.) by self-propulsion (see e.g. Gray [Gra68]), as well as applications in meteorology and sedimentology (see e.g. Kajikawa [Kaj82] and Allen [All84], respectively).

There are several fundamental aspects related to particulate flows and it is important to notice that not all of them are equally relevant for each application. For example, if one is only interested in the *orientation* of rigid particles in fluid flows (see applications ① and ③ above), it is reasonable to restrict the attention to a *single particle*. If, in addition, wall effects are expected to play no role, the problem can be further simplified by assuming that the fluid is filling up the whole space. Such considerations naturally lead to the following classification of particulate flow configurations, giving rise to a *hierarchy of models* with increasing complexity:

- **Single rigid body in a fluid filling the whole space.** This is certainly the right model to study 'pure' particle-liquid interaction, in absence of particle collisions or wall effects. An important example of high practical relevance is, as we have seen, the examination of the orientation of a rigid body in a liquid.

- **Single rigid body in a bounded fluid.** This model is appropriate when one is mainly interested in the impact of rigid walls on the motion of particles. For example, this is the case when one wants to understand the relationship between fluid properties and particle migration in a fluid-filled channel (see ② above).

- **Multiple particles.** In many situations it is possible to generalize conclusions from single-particle studies in order to predict the behavior of a group of particles. Sometimes this is not possible, however, because the (flow-induced) interactions between different particles may lead to microstructures which are relevant for the global behavior of the liquid-particle mixture. Examples include the design of sedimentation columns, see e.g. Wigle et al. [WFS83].

The importance of such a classification lies not only in the fact that it allows for a conceptual separation of the different phenomena related to particulate flows. It is also crucial when it comes to designing numerical algorithms: only a method which *exploits the special structure* of the considered problem can be efficient.

The organization of this work reflects the classification introduced above:

In **Chapter 2** we propose a method for simulating the motion of a single rigid body which is moving, under the action of gravity, through an incompressible viscous fluid filling the whole space. Our numerical method is based on the solution of the incompressible Navier-Stokes equations in body-fixed coordinates and uses a finite element discretization with mesh adaptation based on the DWR (Dual Weighted Residual) concept described in Becker/Rannacher [BeR01], see also Bönisch et al. [BHR05, BDR06]. It works for two- as well as three-dimensional configurations. The performance of the current implementation of this method will be illustrated by the results of some two-dimensional (stationary and non-stationary) simulations. We investigate the existence of quasi-stationary states for symmetric bodies and the dynamic stability of these solutions. Severe difficulties arise from the fact that the unbounded domain has to be truncated for numerical purposes. This introduces 'artificial' boundaries; it turns out that the 'right' choice of the boundary conditions on these artificial boundaries is crucial for the whole solution process.

For this reason, **Chapter 3** is devoted to the issue of finding appropriate artificial boundary conditions for numerically solving exterior flow problems. This topic is of general interest, not only in the context of particulate flow simulations. It has only recently been treated in the mathematics literature (see for example Nazarov/Specovius-Neugebauer [NS03]), but has not led to explicit enough prescriptions to be used in numerical work. Following Wittwer [Wit02, Wit03] and Bönisch et al. [BHW05, BHW06] we provide a vector field describing the leading asymptotic behavior of the solution. This vector field is given in the form of an explicit expression depending on a real parameter. We show that this parameter can be determined from the total drag exerted on the body. Using this fact we set up a novel self-consistent numerical scheme that determines the parameter, and hence the boundary conditions and the drag, as part of the solution process. We compare the results obtained using the traditional homogeneous Dirichlet boundary conditions with those obtained from using our adaptive scheme. The difference is impressive: for a given precision the adaptive boundary conditions allow us to take the domain approximately ten times smaller which results in computation times that are more than a factor of hundred shorter.

In **Chapter 4** we go one step further in the 'model hierarchy' introduced above and treat the motion of a single symmetric particle in a viscoelastic fluid bounded by two parallel walls. More specifically, we consider a cylinder which is moving under the action of gravity in a vertical channel through a Poiseuille flow which may be directed either in the same or in opposite direction of the gravitational force. Our main goal is to find 'steady' solutions to the fluid-particle system and to determine all possible equilibrium positions of the particle with respect to the walls. We use a method recently introduced by Galdi (see Galdi/Heuveline [GH06] and Bönisch/Galdi [BG06]) to investigate these equilibrium positions, *at first order in Re and We*, as well as at *at third order in Re*, where Re is a suitable Reynolds number and We is the Weissenberg number. Comprehensive numerical experiments show the potential of the method.

Chapter 5 is then devoted to the general case: We discuss possibilities to simulate the motion of an arbitrary number of rigid particles in a fluid filling a domain with arbitrary geometry. We give an overview of different numerical approaches proposed for this problem during the past years. We then present an adaptive fictitious-domain method to simulate rigid particulate flow problems. Our algorithm is based on the stress-DLM approach originally proposed by Patankar et al. [PSJ+00]. However, the consequent use of *adaptivity* (adapted meshes, selective quadrature) makes our method much more accurate and efficient, see also Bönisch et al. [BDR06, Boe06]. To show the potential of our approach we first solve a well-known benchmark problem; huge savings in terms of the number of needed mesh cells are achieved. Then, different configurations involving the motion of multiple particles, also with non-smooth boundaries, are simulated.

2 Motion of a single particle in a fluid filling the whole space

The motion of a single rigid body in a viscous fluid filling the whole space is the most fundamental example of a particulate flow. Particularly for rotationally symmetric bodies several theoretical results concerning the existence of quasi-stationary states and their stability are available; see e.g. Weinberger [Wei73], Hu et al. [Hu96, HJC92], Unverdi/Tryggvason [UT92], Desjardin/Esteban [DE99], Glowinski et al. [GPH+01], Burger et al. [BLW01], and Conca et al. [CMT00], Hoffmann/Starovoitov [HS00], Gunzburger et al. [GLS00], Galdi [Gal99, Gal01], Galdi/Vaidya [GV01], and the references cited therein. For general non-symmetric and non-convex bodies these questions seem to be largely open. Here, numerical experiments may be able to guide theoretical analysis. Despite its simplicity the numerical solution of the underlying model equations poses severe difficulties. The conceptually unbounded domain has to be truncated and appropriate artificial boundary conditions are needed. The dynamic behavior of the orientation of the body and the speed and direction of fall is determined by the quantities drag, lift, and torque, the accurate computation of which is rather delicate. The coupling of the relevant quantities in the model is highly nonlinear. The reliable computation of drag, lift, and torque requires a sufficiently large computational domain as well as local mesh refinement along the body's surface.

This chapter is organized as follows: In Section 2.1 we state the equations describing the coupled motion of a single rigid body and a fluid filling the whole space. By choosing a coordinate frame attached to the mass center of the body, we get rid of the time-dependence of the fluid domain. In Section 2.2 we present a finite element scheme for the detailed simulation of the free fall of a single rigid body in a viscous fluid. Numerical results are presented for two-dimensional configurations which allow for stable and unstable quasi-stationary as well as non-stationary solutions. By residual-controlled adaptation of the mesh and the size of the computational domain the method achieves a high degree of flexibility and accuracy.

2.1 Problem formulation

We consider the free fall of a solid body $\mathcal{S} \subset \mathbb{R}^d$ $(d = 2, 3)$ in an incompressible liquid $\mathcal{L}$ filling the whole space $\mathbb{R}^d \setminus \mathcal{S}$. The solid body $\mathcal{S}$ is assumed to be a bounded domain and the velocity of its mass center C (resp. its angular velocity) is denoted by $\mathcal{V}_C$ (resp. Ω) in the inertial frame $\mathcal{F}$. The region occupied by $\mathcal{S}$ at time t is denoted by $S(t)$ and the corresponding attached frame is $\mathcal{R}(t)$. The fluid-body coupling occurs through Dirichlet boundary conditions. In the inertial frame $\mathcal{F}$ the equations of conservation of

momentum and mass of the fluid as well as of linear and angular momentum of the body in their non-conservative form together with their natural boundary conditions are given by

$$\text{Fluid} \quad \begin{cases} \rho\partial_t \mathrm{v} + \rho(\mathrm{v}\cdot\nabla)\mathrm{v} = \rho g + \nabla\cdot\sigma(\mathrm{v},\mathrm{p}), \\ \nabla\cdot\mathrm{v} = 0, \quad \text{for } (x,t)\in\bigcup_{t>0} S(t)^c\times\{t\}, \\ \mathrm{v}(x,0) = 0, \quad \lim_{|x|\to\infty}\mathrm{v}(x,t) = 0, \\ \mathrm{v}(x,t) = \mathcal{V}_C(t) + \Omega(t)\times(x - x_C(t)), \quad \text{for } x\in\partial S(t). \end{cases} \tag{2.1.1}$$

$$\text{Body} \quad \begin{cases} d_t(m_S\mathcal{V}_C) = m_S g - \int_{\partial S(t)}\sigma(\mathrm{v},\mathrm{p})\cdot N\, do, \\ d_t(J_{S(t)}\cdot\Omega) = -\int_{\partial S(t)}(x - x_C)\times[\sigma(\mathrm{v},\mathrm{p})\cdot N]\, do. \end{cases} \tag{2.1.2}$$

Here, ρ is the constant density of $\mathcal{L}$, v and p are the Eulerian velocity field and pressure associated with $\mathcal{L}$, σ is the Cauchy stress tensor and ρg is the force of gravity which is assumed to be the only external force. In the case of a Navier-Stokes liquid model, the Cauchy stress tensor is given by $\sigma(\mathrm{v},\mathrm{p}) = -\mathrm{p}\mathbf{1} + \mu(\nabla\mathrm{v} + (\nabla\mathrm{v})^T)$, where μ is the shear viscosity. Further, m_S is the mass of the body, N is the unit normal to $\partial S(t)$ oriented toward the body and J_S the inertia tensor with respect to the mass center C. We assume $\mathcal{V}_C(0) = 0$ and $\Omega(0) = 0$.

The straightforward formulation (2.1.1-2.1.2) has the disadvantage that the region $S(t)$ occupied by the liquid is time-dependent. This can be avoided by reformulating these equations in the body-attached frame $\mathcal{R}(t)$. If y denotes the position of a point P in the frame $\mathcal{R}(t)$ and x is the position of the same point in $\mathcal{F}$, we have

$$x = Q(t)y + x_C(t), \quad Q(0) = I, \quad x_C(0) = 0, \tag{2.1.3}$$

with Q an orthogonal linear transformation. In addition, we introduce the following transformed fields:

$$v(y,t) := Q^T\mathrm{v}(Qy + x_C, t), \quad p(y,t) := \mathrm{p}(Qy + x_C, t), \quad G := Q^T g, \tag{2.1.4}$$

$$V(y,t) := Q^T(\mathcal{V}_C + \Omega\times Qy), \quad \sigma(v,p) := Q^T\sigma(Q\mathrm{v},\mathrm{p})Q, \quad \omega := Q^T\Omega, \tag{2.1.5}$$

and

$$V_C := Q^T\cdot\mathcal{V}_C, \quad n := Q^T\cdot N, \quad I_S := Q^T\cdot J_S\cdot Q, \quad S := S(0). \tag{2.1.6}$$

Using the transformations (2.1.3-2.1.6), we can reformulate the system of equations (2.1.1-2.1.2) in the following form:

$$\text{Fluid} \quad \begin{cases} \rho\partial_t v + \rho((v - V)\cdot\nabla)v + \rho\omega\times v = \nabla\cdot\sigma(v,p) + \rho G(t), \\ \nabla\cdot v = 0, \quad \text{for } (y,t)\in S^c\times(0,\infty), \\ v(y,0) = 0, \quad \lim_{|y|\to\infty}v(y,t) = 0, \\ v(y,t) = V_C(t) + \omega(t)\times y, \quad \text{for } y\in\partial S. \end{cases} \tag{2.1.7}$$

$$\text{Body} \quad \begin{cases} m_S\dot{V}_C + m_S(\omega\times V_C) = m_S G(t) - \int_{\partial S}\sigma(v,p)\cdot n\, do, \\ I_S\cdot\dot{\omega} + \omega\times(I_S\cdot\omega) = -\int_{\partial S}y\times[\sigma(v,p)\cdot n]\, do, \\ \dot{G} - G\times\omega = 0. \end{cases} \tag{2.1.8}$$

In order to keep compatible notations for both the two and three-dimensional case, we assume for $d = 2$ that $\omega := (0, 0, \boldsymbol{\omega})$ and similarly $y \times [\sigma \cdot n] = (0, 0, -y_2(\sigma \cdot n)_1 + y_1(\sigma \cdot n)_2)$. For $d = 2$, the second equation in (2.1.8) reduces to a scalar equation. The additional term $\omega \times v$ in the momentum equation in (2.1.7) corresponds to the *Coriolis force* induced by the frame transformation (2.1.3). In the body frame $\mathcal{R}(t)$ the direction of the gravitational force G depends on time t and therefore becomes an unknown to be computed. The third additional equation of (2.1.8) provides the equation needed for describing its variation. Its derivation relies on simple calculus related to the transformation (2.1.3). For more details regarding the derivation of these equations, we refer to Galdi [Gal01] or Bönisch et al. [BHR05].

The solid body $\mathcal{S}$ is said to undergo a *free steady fall* if the translational and angular velocity V_C and ω are constant and if the motion of the liquid $\mathcal{L}$ is stationary in the frame $\mathcal{R}(t)$. The study of such a configuration is of great interest since it corresponds to so called *terminal state* motions of sedimenting particles for which many questions still remain open, e.g. the number of possible terminal states for a given body geometry, the orientation of the solid body, the stability of the corresponding solution (see Galdi [Gal01] and references therein).

The free steady fall equations are obtained by requiring that v, p, V_C, ω, and G are time independent. Comparing with (2.1.7-2.1.8), this leads us to the following system of equations:

$$
\text{Fluid} \quad
\begin{cases}
\rho((v - V) \cdot \nabla)v + \rho \omega \times v = \nabla \cdot \sigma(v, p) + \rho G, \\
\nabla \cdot v = 0, \quad \text{for } y \in \mathbb{R}^d \setminus S, \\
v(y, 0) = 0, \quad \lim_{|y| \to \infty} v(y) = 0, \\
v(y) = V(y) := V_C + \omega \times y \quad \text{for } y \in \partial S.
\end{cases}
\tag{2.1.9}
$$

$$
\text{Body} \quad
\begin{cases}
m_S(\omega \times V_C) = m_S G - \int_{\partial S} \sigma(v, p) \cdot n \, do, \\
\omega \times (I_S \cdot \omega) = - \int_{\partial S} y \times [\sigma(v, p) \cdot n] \, do, \\
G \times \omega = 0.
\end{cases}
\tag{2.1.10}
$$

For the most general setup, we assume $\omega \neq 0$. Due to the third equation in (2.1.10), this configuration can be attained only for $d = 3$. Further it imposes G parallel to ω. The free steady fall problem can then be stated as follows:

Problem 2.1 (*Stationary fall in 3D*). Assume $d = 3$. Given ρ, $\sigma = \sigma(v, p)$, $|G| = |g|$, I_S, and m_S, find v, p, V_C, ω, and G, where $G = |g||\omega|^{-1}\omega$ if $\omega \neq 0$ (see Table 2.1), such that equations (2.1.9-2.1.10) hold.

An important subclass of free steady fall problems is given by the case $\omega = 0$ describing a solid body $\mathcal{S}$ which undergoes a purely *translational* motion. The problem formulation for this case is subtle since it depends not only on the dimension d of the problem but also on the geometrical properties of the solid.

At first, we assume that the equation $G \times \omega = 0$ has to be enforced and cannot be eliminated by means of any special geometrical properties of the solid $\mathcal{S}$ or on the flow configuration. For $d = 3$ such a translational problem is overdetermined and will therefore not be further considered (see Table 2.1). For $d = 2$, however, this problem is well formulated in the sense that it involves six unknowns associated to six scalar equations. It can be stated as follows:

Problem 2.2 (*Stationary fall in 2D*). Assume $d = 2$. Given ρ, $\sigma = \sigma(v, p)$, $|G| = |g|$, I_S, m_S, and $\omega := 0$, find v, p, V_C, and the direction $\hat{G}$ of $G := |g|\hat{G}$, such that equations (2.1.9-2.1.10) hold.

The system of equations (2.1.9-2.1.10) describe different classes of free-fall regimes and configurations which are outlined in Table 2.1.

Table 2.1: Number of physical unknowns in the fluid-rigid body interaction problem depending on the setup. The body/fluid setup is said to be 'general' if no additional a-priori assumption on the body geometry is made which eliminates the third equation in (2.1.10) directly.

Dimension	ω	Body-fluid setup	Formulation	Number of unknowns	Number of scalar equations
3	$\neq 0$	general	Problem 2.1	10	10
2	$\neq 0$	general	not possible	-	-
3	$= 0$	general	overdetermined	9	10
2	$= 0$	general	Problem 2.2	6	6
3	$= 0$	symmetric	Problem 2.3	5	5
2	$= 0$	symmetric	Problem 2.3	4	4

From the physical point of view, the overdetermination of the translational free steady fall for $d = 3$ can be interpreted by the fact that additional geometric properties of the solid body $\mathcal{S}$ have to prevent it from rotating (see Galdi/Vaidya [GV01]). Following Galdi [Gal01], we consider now translational free steady fall problems for solid bodies with symmetry properties. Let $\{e_1, e_2, e_3\}$ be the canonical basis of $\mathbb{R}^3$. Assume that the solid body is homogeneous and symmetric with respect to the axis e_2. Likewise, the velocity field v and the pressure p describing the terminal state of the fluid $\mathcal{L}$ are assumed to be symmetric with respect to the axis e_2. Under these assumptions, one can show (see Galdi/Vaidya [GV01]) that every sufficiently smooth pair $\{v, p\}$ satisfies the following equations:

$$\int_{\partial S} \sigma(v, p) \cdot n = \eta \, e_2, \quad \eta \in \mathbb{R}, \tag{2.1.11}$$

$$\int_{\partial S} y \times [\sigma(v, p) \cdot n] = 0, \tag{2.1.12}$$

$$V = \alpha_V e_2, \; \alpha_V \in \mathbb{R}. \tag{2.1.13}$$

Therefore, for the symmetric case equations (2.1.10) reduce to the following scalar equation:

$$\left\{ \int_{\partial S} \sigma(v, p) \cdot n \, ds \right\}_2 + m_S |g| = 0, \tag{2.1.14}$$

since comparing the first equation of (2.1.10) with (2.1.11) implies $G = \pm|g|e_2$. We choose the orientation $G = -|g|e_2$ for the force of gravity. Under these assumptions of symmetry, the steady free fall problem can be formulated as follows:

Problem 2.3 (Symmetric steady fall in 2D/3D). Given ρ, $\sigma = \sigma(v,p)$, $G = -|g|e_2$, I_S, m_S, and $\omega := 0$, find v, p, and the scalar quantity α_V defining $V := \alpha_V e_2$, such that equations (2.1.9) and (2.1.14) hold.

Problem 2.3 is well formulated for both two- and three-dimensional problems.

2.2 Numerical approximation

Our numerical method is based on the solution of the incompressible Navier-Stokes equations in body-fixed coordinates and uses a finite element discretization with mesh adaptation based on the DWR (Dual Weighted Residual) concept described in Becker/Rannacher [BeR01]. By systematic mesh refinement the quantities of interest, such as the free fall velocity, the orientation of the body and the acting hydrodynamic force and torque, can be computed to any prescribed accuracy. This works for two- as well as three-dimensional configurations. An additional feature is the monitoring of the stability of quasi-stationary solutions by computing critical eigenvalues. The performance of the current implementation of this method will be illustrated by the results of some simulations for two-dimensional configurations with stationary as well as non-stationary solutions. We investigate the existence of quasi-stationary states for symmetric bodies and the dynamic stability of these solutions. More details on the numerical methodology and the computational examples can be found in Bönisch/Heuveline [BH04a] and Bönisch et al. [BHR05]. These 'experimental' observations may serve as stimulus for further theoretical analysis.

2.2.1 The general non-stationary case

We first consider the setting of formulation (2.1.7-2.1.8) for the solution of the general free-fall problem. The unbounded domain $\mathbb{R}^d \backslash S$ filled by the liquid $\mathcal{L}$ is replaced by a bounded domain $D \subset \mathbb{R}^d \backslash S$ which is chosen to be large enough in order that the liquid may be assumed to be at rest on Γ which denotes the boundary of D without ∂S. In the remainder of this paper, D is chosen such that the impact of this simplification on the quantities of interest is smaller than the discretization error. We refer to Section 2.2.3 and to Chapter 3 for a detailed discussion of this issue, see also Bönisch et al. [BHW05, BHW06].

We begin with some standard notation. For a domain $\Omega \subset \mathbb{R}^d$, let $L^2(\Omega)$ denote the Lebesgue space of square-integrable functions on Ω equipped with the inner product and norm

$$(f,g)_\Omega := \int_\Omega fg\,dx, \quad \|f\|_\Omega := (f,f)^{1/2}.$$

Analogously, $L^2(\partial\Omega)$ denotes the space of square integrable functions defined on the boundary $\partial\Omega$. The L^2 functions with generalized (in the sense of distributions) first-order derivatives in $L^2(\Omega)$ form the Sobolev space $H^1(\Omega)$, while $H_0^1(\Omega) = \{v \in H^1(\Omega), v_{|\partial\Omega} = 0\}$ and $L_0^2(\Omega) := \{q \in L^2(\Omega) : (q, 1)_\Omega = 0\}$.

The key ingredient for the derivation of a weak form of the equations is an adequate choice of the velocity space allowing to eliminate the explicit formulation of the hydrodynamic force and torque on the solid body needed for the kinematic equations (2.1.10). This can be obtained by including the no-slip Dirichlet condition in the velocity space:

$$\mathcal{H}_1(D) := \left\{(v, V, \omega) : v \in [H^1(D)]^d, V, \omega \in \mathbb{R}^d, v_{|\partial S} = V + \omega \times y\right\}.$$

The pressure p, defined only modulo constants, is assumed to lie in the space $L_0^2(D)$. For $U := \{(v, V_C, \omega), p, G\}$, $\Phi := \{(\varphi, \varphi_1, \varphi_2), q, \gamma\} \in \mathcal{H}_1(D) \times L_0^2(D) \times \mathbb{R}^d$, we define the semilinear form

$$\begin{aligned}
A(U)(\Phi) := {} & \rho(((v - (V_C + \omega \times y)) \cdot \nabla)v, \varphi)_D + \rho(\omega \times v, \varphi)_D \\
& - (p, \nabla \cdot \varphi)_D + 2\mu(\mathcal{D}(v), \mathcal{D}(\varphi))_D - (\rho G, \varphi)_D \\
& - \varphi_1 \cdot [m_S(G - \omega \times V_C)] + \varphi_2 \cdot [\omega \times (I_S \cdot \omega)] - (\nabla \cdot v, q)_D,
\end{aligned}$$

which is obtained by testing the equations (2.1.9-2.1.10) with $\Phi \in \mathcal{H}_1(D) \times L_0^2(D) \times \mathbb{R}^d$ and by integration by parts of the diffusive terms and the pressure gradient. Here, $\mathcal{D}(v) := \frac{1}{2}(\nabla v + (\nabla v)^T)$ is the deformation tensor. The equations (2.1.9) modeling the balance of the linear and angular momentum can obviously be recovered by testing $A(U)(\Phi)$ with the functions $\Phi = \{(0, \varphi_1, 0), 0, 0\}$ and $\Phi = \{(0, 0, \varphi_2), 0, 0\})$, respectively. Further, we will use the bilinear form

$$m(\partial_t U, \Phi) := (\rho\partial_t v, \varphi) + (m_S \dot{V}_C, \varphi_1) + (I_S \cdot \dot{\omega}, \varphi_2) + (\dot{G}, \gamma).$$

Then, the variational formulation of the general non-stationary problem reads as follows:

Problem 2.4. Find a time-differentiable field $U(t) = \{(v(t), V_C(t), \omega(t)), p(t), G(t)\} \in \mathcal{H}_1(D) \times L_0^2(D) \times \mathbb{R}^d$, such that

$$m(\partial_t U, \Phi) + A(U)(\Phi) = 0 \quad \forall \Phi \in \mathcal{H}_1(D) \times L_0^2(D) \times \mathbb{R}^d. \tag{2.2.1}$$

Remark 2.2.1. The advantages of the formulation (2.2.1) rely on the fact that the force and torque on the solid body do not need to be computed explicitly. Numerical instabilities arising for the computation of these lower dimensional integrals can therefore be avoided (see Hu et al. [HJC92]).

Problem 2.4 is discretized in time by the so-called *Fractional-Step-θ scheme* described, e.g. in Rannacher [Ran00] and Turek [Tur99]. The fluid-body interaction is handled by operator splitting leading to the following time-stepping process:

(1) Extrapolate $V_C^{n-1}, \omega^{n-1}, G^{n-1}$ to $\tilde{V}_C^n, \tilde{\omega}^n, \tilde{G}^n$ (*explicit*).

(2) For $A(v) := -\mu\Delta v + \rho((v - \tilde{V}_C^n - \tilde{\omega}^n \times y) \cdot \nabla)v + \rho\,\tilde{\omega}^n \times v$, compute v^n, p^n from the Navier-Stokes system (2.1.7) by solving the following three substeps using the Newton method with geometric multigrid solution of the linear subsystems (*implicit*):

(2a)

$$\rho v^{(n-1+\theta)} + \alpha\theta k A(v^{(n-1+\theta)}) + \theta k \nabla p^{(n-1+\theta)} = \rho v^{(n-1)} - \beta\theta k A(v^{(n-1)}) + \rho\theta k \tilde{G}^n,$$

$$\nabla \cdot v^{(n-1+\theta)} = 0,$$

(2b)

$$\rho v^{(n-\theta)} + \beta\theta' k A(v^{(n-\theta)}) + \theta' k \nabla p^{(n-\theta)} = \rho v^{(n-1+\theta)} - \alpha\theta' k A(v^{(n-1+\theta)}) + \rho\theta' k \tilde{G}^n,$$

$$\nabla \cdot v^{(n-\theta)} = 0,$$

(2c)

$$\rho v^{(n)} + \alpha\theta k A(v^{(n)}) + \theta k \nabla p^{(n)} = \rho v^{(n-\theta)} - \beta\theta k A(v^{(n-\theta)}) + \rho\theta k \tilde{G}^n,$$

$$\nabla \cdot v^{(n)} = 0.$$

In order to ensure second-order accuracy and strong A-stability we choose $\theta = 1 - \frac{\sqrt{2}}{2}$, $\theta' = 1 - 2\theta$, $\alpha = \frac{1-2\theta}{1-\theta}$ and $\beta = 1 - \alpha$ (see e.g. Turek [Tur99]).

(3) Compute the hydrodynamic forces acting on the body.

(4) Update V_C^n, ω^n, G^n by applying one step of a higher-order explicit scheme to the corresponding ODEs (*explicit*).

Remark 2.5. A few comments on the proposed splitting scheme are in order. It employs an *explicit* treatment of the fluid-body coupling. An intrinsic difficulty of this approach is related to the fact that the 'data' $\tilde{V}_C^n, \tilde{\omega}^n, \tilde{G}^n$ occurring in the substep problems (2a),(2b),(2c) are generally *non-smooth* with regard to the time variable due to the explicit update. It is well known that non-smooth data may drastically reduce the accuracy of a discretization scheme or even lead to divergence unless certain precautions are taken (see e.g. Luskin/Rannacher [LR81] and Rannacher [Ran84]). More precisely, the time-stepping scheme should be *strongly A-stable* and have the full *smoothing property* (for these notions we refer the reader to Rannacher [Ran00] and Turek [Tur99]). The importance of this property is illustrated in Figure 2.1 where the values of the drag, lift and torque acting on a falling body in a fluid are plotted. It shows a comparison between the Fractional-Step-θ scheme (which *is* strongly A-stable) and the popular Crank-Nicolson method (which is *not* strongly A-stable). From Figure 2.1 it becomes clear that the strong A-stability of the time stepping scheme is a key issue in our context. In fact, the use of the Crank-Nicolson method leads to the divergence of the overall algorithm. Following the idea of Rannacher [Ran84], an alternative to using the Fractional-Step-θ scheme is to use a *damped Crank-Nicolson method* which combines adequately two implicit (smoothing) Euler steps with one Crank-Nicolson step. The resulting scheme possesses all needed smoothing properties and performs excellently well in our context, see Figure 2.1.

The stationary subproblems within this scheme are discretized in space by the finite element method on a triangulation of the domain $D = \cup\{K \in \mathbb{T}_h\}$, using the Q_2/Q_1 Taylor-Hood element on a quadrilateral mesh with hanging nodes for local mesh refinement (see e.g. Girault/Raviart [GR86]). The finite element spaces are given by

$$W_1^h := \big\{((v, V, \omega), p) \in ([C(\overline{D})]^d \times \mathbb{R}^d \times \mathbb{R}^d) \times C(\overline{D}),$$

$$v|_K \in [Q_2]^d, p|_K \in Q_1, v|_{\partial S} = V + \omega \times y\big\},$$
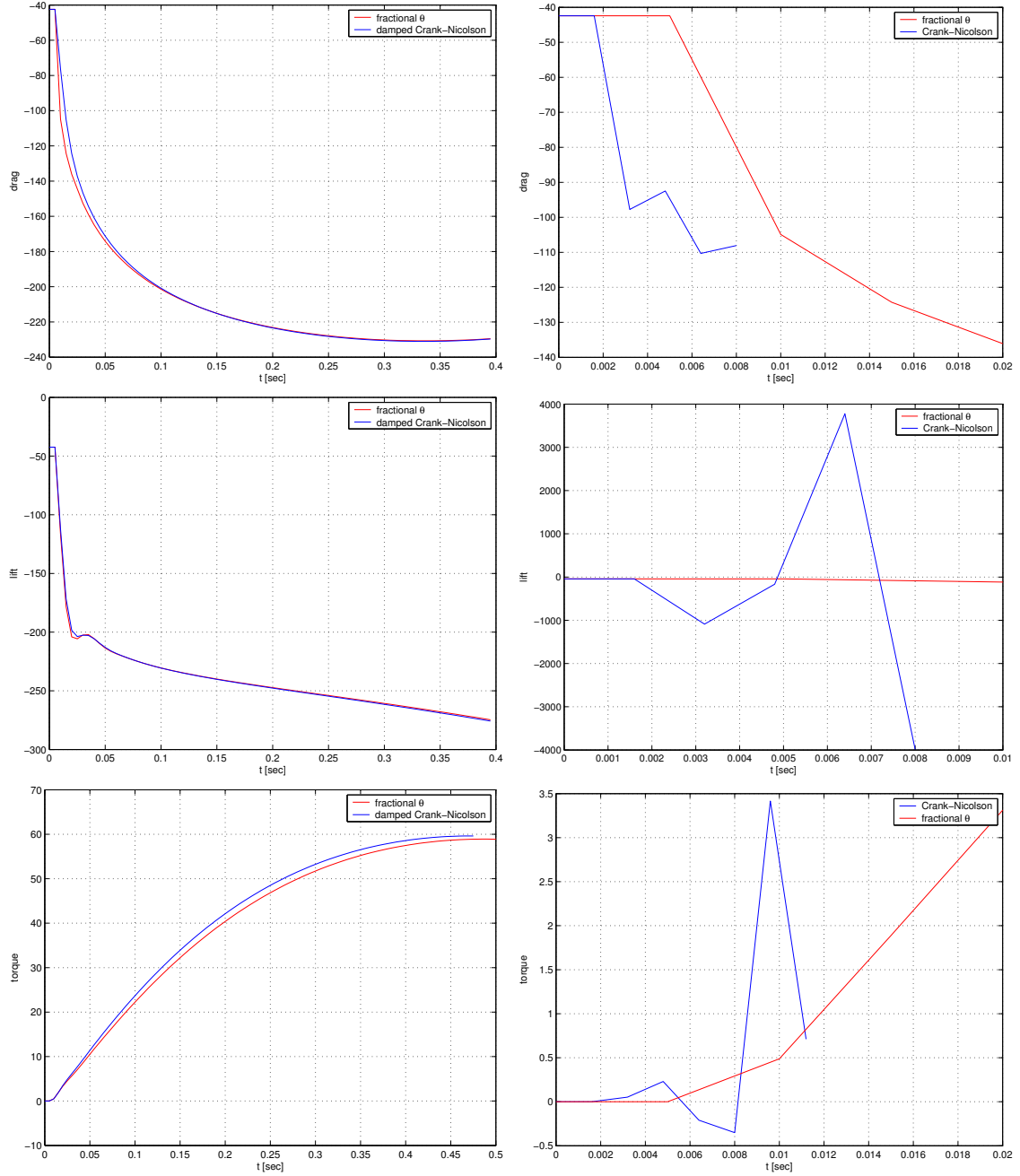
Figure 2.1: Plots of the drag (**upper row**), lift (**middle row**) and torque (**lower row**) acting on a falling rectangle in a fluid. **Left:** Comparison of the 'Fractional-Step-θ scheme' [Tur99] and the 'damped Crank-Nicolson' method [Ran84]. Both methods possess the smoothing property needed in order to handle correctly non-smooth data which occur due to the explicit update strategy used in our splitting scheme. **Right:** Comparison of the Fractional-Step-θ scheme and the popular Crank-Nicolson method. The lack of smoothing property of the Crank-Nicolson method leads to the divergence of the solution process.

in which the no-slip Dirichlet condition is included, in order to avoid the explicit formulation of the hydrodynamic force and torque on the solid body needed for the kinematic equations. This approximation is consistent with third-order, i.e., there holds $\|v - I_h v\| = \mathcal{O}(h^3)$ for the nodal interpolant $I_h v$ of a sufficiently smooth velocity field. The implementation of the algorithm was carried out within the **HiFlow** framework (see [Heu06]).

To show the potential of our approach we would like to report on some computational results obtained by the numerical method described above. In a two-dimensional setting, we simulate the free fall of a (symmetric) rigid rod in a viscous liquid. We are interested in the different types of steady and unsteady fall patterns for varying Reynolds numbers. This question has been extensively studied in the experimental literature, see e.g. Field et al. [FKM+97] and Belmonte et al. [BEM98]. The observations of Field et al. lead to the classification in four distinct types of motion for such a setup, see also Bönisch/Heuveline [BH04a]:

- **Quasi-steady falling**, observed at low Reynolds numbers; a rod, dropped with any initial orientation, quickly settles down to a steady fall with horizontal orientation (cf. also Galdi and Galdi/Vaidya [Gal01, GV01]).

- **Periodic oscillating motion**, observed at higher Reynolds numbers and low moment of inertia. Such rods oscillate with a well-defined period after initial transients have died down.

- **'Chaotic' motion**, found when both, the Reynolds number and the moment of inertia, are moderately large.

- **Tumbling motion**, found at very large moments of inertia. Here, the disk turns continuously end-over-end while drifting in one direction.

As shown in Figure 2.2, all four types of motion could be reproduced by the numerical simulation. On the one hand, this can be seen as a validation of our numerical method. On the other hand, it gives an impression how numerical simulation can be successfully used to replace 'real' experiments by computations and maybe to lead beyond classical experiments.

2.2.2 The special stationary problems

The particular features of the various formulations of the *stationary* free-fall problem result in correspondingly simplified approximate problems. We first consider the most general setup of Problem 2.1, i. e., $\omega \neq 0$ and the related equations (2.1.9-2.1.10). For $U := \{(v, V_C, \omega), p\}$, $\Phi := \{(\varphi, \varphi_1, \varphi_2), q\} \in \mathcal{H}_1(D) \times L_0^2(D)$, we define the semi-linear form

$$
\begin{aligned}
A_1(U)(\Phi) := {} & \rho(((v - (V_C + \omega \times y)) \cdot \nabla)v, \varphi)_D + \rho(\omega \times v, \varphi)_D \\
& - (p, \nabla \cdot \varphi)_D + 2\mu(\mathcal{D}(v), \mathcal{D}(\varphi))_D - (\rho|g|\|\omega|^{-1}\omega, \varphi)_D \\
& - \varphi_1 \cdot [m_S(|g|\|\omega|^{-1}\omega - \omega \times V_C)] + \varphi_2 \cdot [\omega \times (I_S \cdot \omega)] - (\nabla \cdot v, q)_D.
\end{aligned}
$$

A weak form of Problem 2.1 reads as follows:

Problem 2.6. Find $U := \{(v, V_C, \omega), p\} \in \mathcal{H}_1(D) \times L_0^2(D)$, such that

$$
A_1(U)(\Phi) = 0 \quad \forall \Phi \in \mathcal{H}_1(D) \times L_0^2(D). \tag{2.2.2}
$$

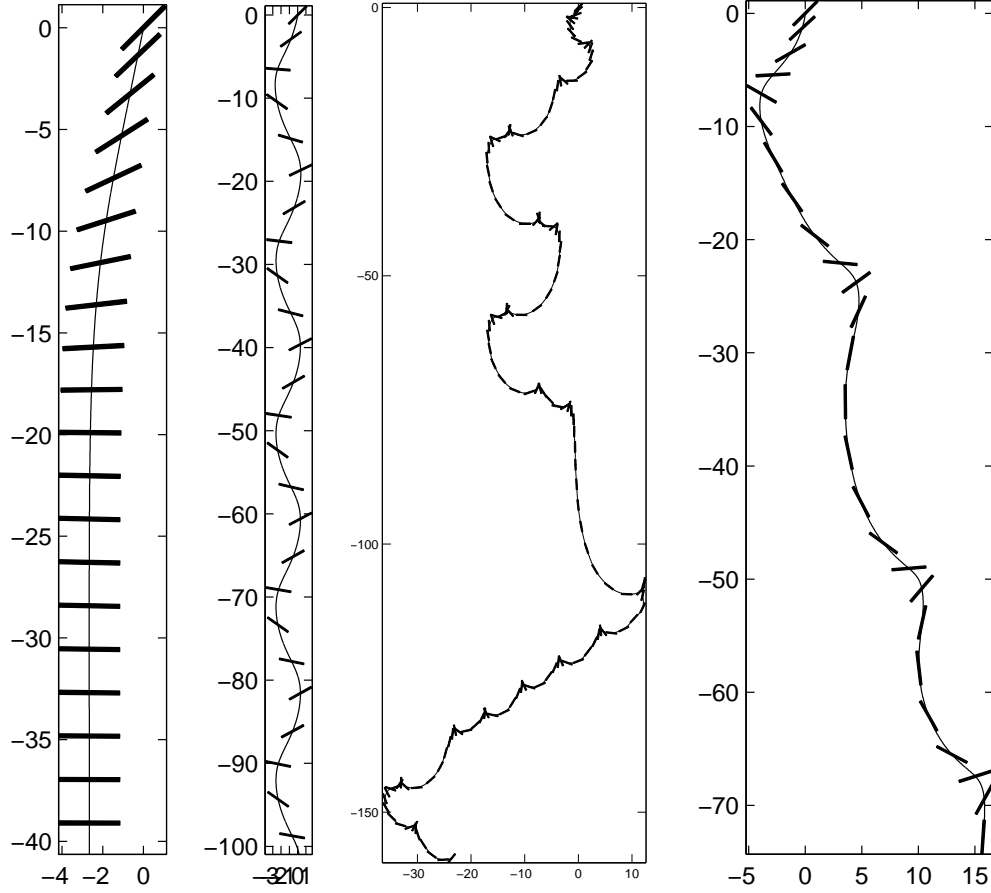**Figure 2.2:** 'Free-fall' patterns of symmetric bodies (from left to right): quasi-steady, oscillatory, 'chaotic' and tumbling motion. See also Figure 2.3 below.
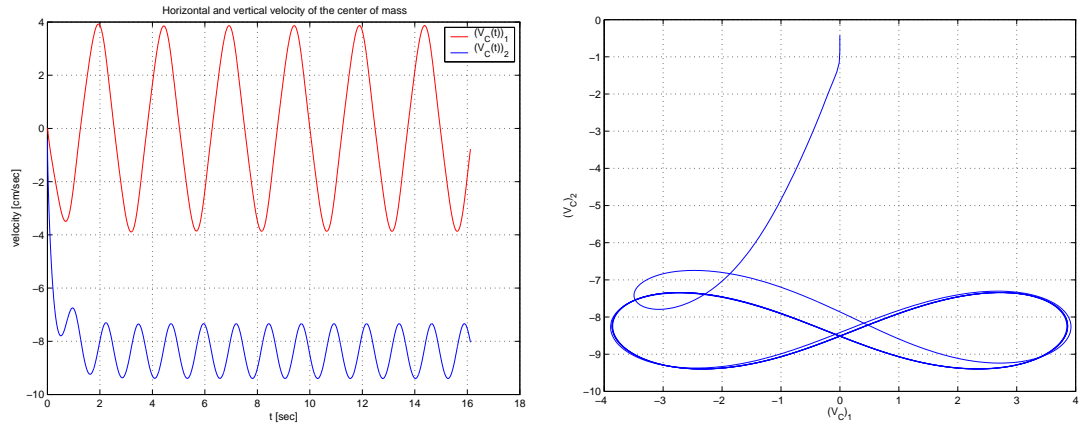

Figure 2.3: Periodic oscillating motion. **Left**: The two components of the translational velocity $V_C(t)$ are plotted vs. time. **Right**: The velocity components $(V_C(t))_1$ and $(V_C(t))_2$ are plotted against each other.

For the weak formulation of Problem 2.2 and Problem 2.3, the formulation (2.2.2) simplifies greatly since the free steady fall is then assumed to be translational. For the velocity field we define
$$\mathcal{H}_2(D) := \left\{ (v, V) : v \in [H^1(D)]^d, V \in \mathbb{R}^d, v = V \text{ on } \partial S \right\}.$$

For $U := \{(v, V_C), p, \theta\} \in \mathcal{H}_2(D) \times L_0^2(D) \times \mathbb{R}$ and $\Phi := \{(\varphi, \varphi_1), q, \varphi_2\} \in \mathcal{H}_2(D) \times L_0^2(D) \times \mathbb{R}$, we define the semi-linear form

$$\begin{aligned}
A_2(U)(\Phi) := {} & \rho(((v - V_C) \cdot \nabla)v, \varphi)_D - (p, \nabla \cdot \varphi)_D + 2\mu(\mathcal{D}(v), \mathcal{D}(\varphi))_D \\
& - (\nabla \cdot v, q)_D - \rho(G, \varphi) - m_S G \cdot \varphi_1 \\
& + (-y_2 \{\sigma(v, p) \cdot n\}_1 + y_1 \{\sigma(v, p) \cdot n\}_2, \varphi_2)_{\partial S},
\end{aligned}$$

where G is assumed to be $G := |g| \binom{\cos \theta}{\sin \theta}$. The weak formulation of Problem 2.2 may then be stated as follows:

Problem 2.7. Find $U := \{(v, V_C), p, \theta\} \in \mathcal{H}_2(D) \times L_0^2(D) \times \mathbb{R}$, such that
$$A_2(U)(\Phi) = 0 \quad \forall \Phi \in \mathcal{H}_2(D) \times L_0^2(D) \times \mathbb{R}. \tag{2.2.3}$$

For Problem 2.3 the direction of the gravitation force G is not a variable anymore. Furthermore, due to equation (2.1.13) the direction of V_C is known to be collinear to e_2. For this configuration, we therefore define the following space
$$\mathcal{H}_3(D) := \left\{ (v, \alpha_V) : v \in [H^1(D)]^d, \alpha_V \in \mathbb{R}, v = \alpha_V e_2 \text{ on } \partial S \right\}, \tag{2.2.4}$$

for the velocity field. For $U := \{(v, \alpha_V), p\}, \Phi := \{(\varphi, \varphi_1), q\} \in \mathcal{H}_3(D) \times L_0^2(D)$, we define the semi-linear form

$$\begin{aligned}
A_3(U)(\Phi) := {} & \rho(((v - \alpha_V e_2) \cdot \nabla)v, \varphi)_D - (p, \nabla \cdot \varphi)_D + 2\mu(\mathcal{D}(v), \mathcal{D}(\varphi))_D \\
& - (\nabla \cdot v, q)_D - (\rho G, \varphi)_D - m_S \varphi_1 e_2 \cdot G.
\end{aligned}$$

The weak formulation for Problem 2.3 may then be stated as follows:

Problem 2.8. Find $U := \{(v, \alpha_V), p\} \in \mathcal{H}_3(D) \times L_0^2(D)$, such that
$$A_3(U)(\Phi) = 0 \quad \forall \Phi \in \mathcal{H}_3(D) \times L_0^2(D). \tag{2.2.5}$$

Using the finite element spaces W_1^h defined above, the discrete counterpart of Problem 2.6 reads as follows:

Problem 2.9. Find $U_h \in W_1^h$, such that
$$A_1(U_h)(\Phi_h) = 0 \quad \forall \Phi_h \in W_1^h. \tag{2.2.6}$$

Analogously, we define for Problem 2.7 and Problem 2.8, respectively, the following finite element spaces

$$\begin{aligned}
W_2^h &:= \left\{ (v, V, p, \theta) \in [C(\overline{D})]^d \times \mathbb{R}^d \times C(\overline{D}) \times \mathbb{R}, v_{|K} \in [Q_2]^d, p_{|K} \in Q_1, v_{|\partial S} = V \right\}, \\
W_3^h &:= \left\{ (v, \alpha_V, p) \in [C(\overline{D})]^d \times \mathbb{R} \times C(\overline{D}), v_{|K} \in [Q_2]^d, p_{|K} \in Q_1, v_{|\partial S} = \alpha_V e_2 \right\}.
\end{aligned}$$

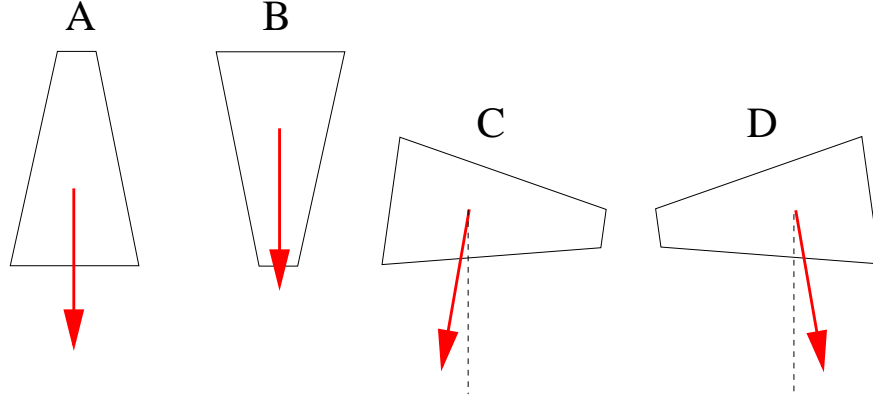The discrete counterpart of Problem 2.7 reads

Figure 2.4: All possible orientations corresponding to a steady free fall of a trapezoidal body. The red arrow shows the direction of the translational velocity. Only configurations **C** and **D** are physically meaningful; the 'symmetry solutions' **A** and **B** are unstable under small perturbations.

Problem 2.10. Find $U_h \in W_2^h$, such that

$$A_2(U_h)(\Phi_h) = 0 \quad \forall \Phi_h \in W_2^h. \tag{2.2.7}$$

Analogously, the discrete counterpart of Problem 2.8 reads

Problem 2.11. Find $U_h \in W_3^h$, such that

$$A_3(U_h)(\Phi_h) = 0 \quad \forall \Phi_h \in W_3^h. \tag{2.2.8}$$

We close this section by showing a two-dimensional computational result obtained by the numerical method presented above. We ask for all possible steady solutions of the free fall problem for a trapezoidal body. We found that there are four different orientations corresponding to a steady translational fall which are depicted in Figure 2.4. Note that only two of these are physically meaningful, i.e. attainable as limit solutions of the unsteady problem; to test the stability of a steady solution we simply ran the non-stationary version of our solver (cf. Section 2.2.1) with a slightly perturbed initial orientation of the body. Figure 2.5 clearly shows the (dynamical) instability of one of the steady solutions. (For another possibility to check the stability of solutions, please refer to Section 2.2.5.) The two components of the velocity of one of the (stable) solutions are depicted in Figure 2.5.

2.2.3 The issue of domain truncation

The truncation of the unbounded exterior domain to a bounded computational domain with artificial (homogeneous) 'outflow' boundary conditions creates errors which may be of significant size. To illustrate this point, we consider the particular situation with the parameters body length $l = 6$, body width $w = 1$, shear viscosity $\mu = 0.1$, and density $\rho = 1$. Figure 2.6 shows the dependence of the free-fall velocity on the diameter d_D of the

Figure 2.5: Left: The non-stationary solver is applied with an initial orientation of the trapezoidal body corresponding to orientation A in Fig. 2.4, but slightly perturbed. Rapidly the body turns towards a steady orientation corresponding to case D in Fig. 2.4 which 'proves' the dynamical instability of solution A. **Right:** visualization of the two components of the fluid velocity.
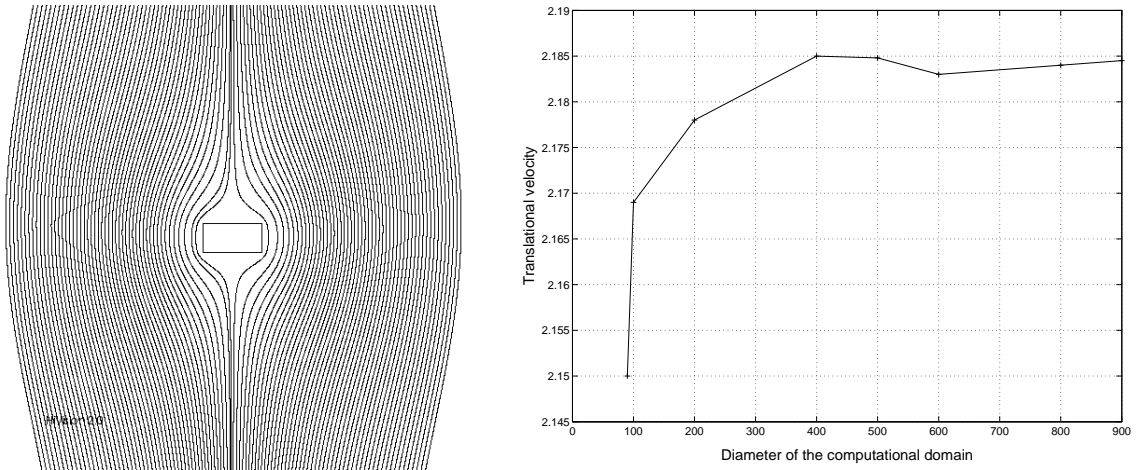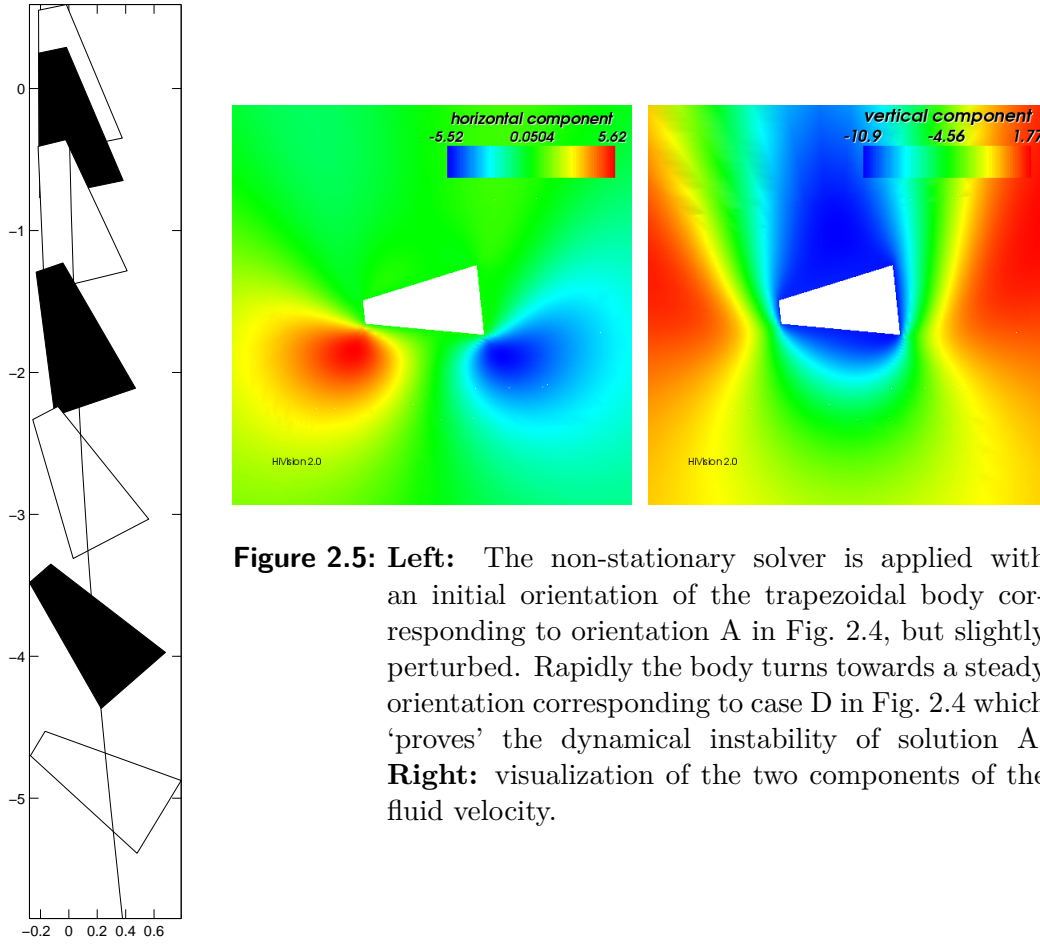

Figure 2.6: Effect of the domain truncation (**right**) on the free-fall velocity of a steady, translational motion (**left**).

truncated computational domain when homogeneous Dirichlet conditions are prescribed on the artificial boundaries. We see that satisfactory accuracy is achieved only for $d_D \geq 400$ units.

Asymptotic analysis shows that a 'parabolic wake' develops upstream and in the crosswind direction the flow behaves like potential flow. Hence for modeling the far field behavior of the flow, one may use 'outflow' boundary conditions governed by the Gaussian (heat) kernel,

$$v \sim \left(\frac{1}{2} C x_1 x_2^{-3/2} \, e^{-\frac{U x_1^2}{4\nu x_2}}, C x_2^{-1/2} \, e^{-\frac{U x_1^2}{4\nu x_2}} \right)^T, \quad C := -\frac{Q\sqrt{U}}{2\sqrt{\pi\nu}},$$

and by the derivative of the Green's function,

$$v(x) \sim \frac{Q}{4\pi} \frac{x}{|x|^2}.$$

On this basis, improved non-homogeneous artificial boundary conditions can be derived for the truncated computational domain which allow for a significant reduction of its size without sacrificing accuracy. For a detailed discussion of this subject, we refer to Chapter 3 and to Wittwer [Wit02, Wit03] and Bönisch et al. [BHW05, BHW06]. Other approaches for treating unbounded domains are discussed in Tsynkov [Tsy98, Tsy99].

2.2.4 Towards economical meshes: a weighted a-posteriori error estimator

Our goal in this section is to derive an a posteriori error estimator to control the accuracy of the most important output quantities in the free-fall problem, namely the velocity and the orientation of the falling body. At the same time this gives us strategies for an adequate mesh adaptation in order to obtain economical meshes. The derivation of a posteriori error estimates for the approximation of the continuous equation (2.2.2) by means of equation (2.2.6) relies on their interpretation as an optimal control problem and their embedding into the framework described in Becker/Rannacher [BeR01].

At first we recall from Becker/Rannacher [BeR01] an abstract framework for the a posteriori error analysis of Galerkin approximation of general nonlinear variational equations; see also Becker et al. [BeHR02] and Bangerth/Rannacher [BaR03]. Let $A(\cdot)(\cdot)$ be a differentiable semi-linear form defined on a function space W. The derivatives of $A(\cdot)(\cdot)$ at a point u in direction $\delta u, \delta v, \delta w$ are denoted by $A'(u)(\delta u, \cdot)$, $A''(u)(\delta u, \delta v, \cdot)$, and $A'''(u)(\delta u, \delta v, \delta w, \cdot)$, e.g.,

$$A'(u)(\delta u, \varphi) := \lim_{\tau \to 0} \frac{1}{\tau} \big\{ A(u + \tau \delta u)(\varphi) - A(u)(\varphi) \big\}, \quad \varphi \in W.$$

Here, we use the convention that the dependence on the variables in the second round brackets is always linear while that with respect to the variable in the first brackets may be nonlinear. We assume that the variational equation

$$A(u)(\varphi) = 0 \quad \forall \varphi \in W, \tag{2.2.9}$$

has a solution $u \in W$. Suppose that the goal is to compute a certain physical quantity related to u by a differentiable functional $J(\cdot)$ with derivatives denoted by $J'(u)(\delta u)$,

$J''(u)(\delta u, \delta v)$, and $J'''(u)(\delta u, \delta v, \delta w)$. Problem (2.2.9) is thought to be approximated by a Galerkin method using finite dimensional subspaces $W_h \subset W$ parametrized by $h \in \mathbb{R}_+$. We assume that the associated discrete problems

$$A(u_h)(\varphi_h) = 0 \quad \forall \varphi_h \in W_h, \tag{2.2.10}$$

also possess solutions $u_h \in W_h$ with $J(u_h)$ being the approximation to the target quantity $J(u)$.

The aim is now to derive a posteriori estimates for the error $J(u) - J(u_h)$. To this end, we employ the Euler-Lagrange approach of optimal control theory. The problem of computing $J(u)$ from the solution of (2.2.9) can be equivalently formulated as computing stationary points $\{u, z\} \in W \times W$ of the Lagrangian functional

$$L(u)(z) := J(u) - A(u)(z), \tag{2.2.11}$$

with the adjoint variable $z \in W$. Hence we seek solutions $\{u, z\} \in W \times W$ to the Euler-Lagrange system

$$A(u)(\varphi) = 0 \quad \forall \varphi \in W, \tag{2.2.12}$$
$$A'(u)(\varphi, z) = J'(u)(\varphi) \quad \forall \varphi \in W. \tag{2.2.13}$$

Notice that the first equation of this system is just the considered variational equation (2.2.9). The Galerkin approximation of system (2.2.12-2.2.13) in the subspace $W_h \subset W$ seeks pairs $\{u_h, z_h\} \in W_h \times W_h$ satisfying

$$A(u_h)(\varphi_h) = 0 \quad \forall \varphi_h \in W_h, \tag{2.2.14}$$
$$A'(u_h)(\varphi_h, z_h) = J'(u_h)(\varphi_h) \quad \forall \varphi_h \in W_h. \tag{2.2.15}$$

To the approximate solutions $u_h \in W_h$, we associate the residual

$$\rho(u_h)(\cdot) := -A(u_h)(\cdot), \tag{2.2.16}$$

which is defined on all of W.

Proposition 2.2.2. For the Galerkin approximation (2.2.14-2.2.15) of the Euler-Lagrange system (2.2.12-2.2.13), we have the a posteriori error representation

$$J(u) - J(u_h) = \rho(u_h)(z - \varphi_h) + R_h \tag{2.2.17}$$

for arbitrary elements $\varphi_h \in W_h$. The remainder R_h is quadratic in the error $e := u - u_h$ and given by

$$R_h = \int_0^1 \left\{ A''(u_h + se)(e, e, z) - J''(u_h + se)(e, e) \right\} s\,ds. \tag{2.2.18}$$

Proof. The proof which relies on standard differential calculus can be found in Becker/Rannacher [BeR01]. $\square$

This general approach will now be applied to the (steady) free-fall problem. We recall the governing semi-linear form

$$A_1(U)(\Phi) := \rho(((v - (V_C + \omega \times y)) \cdot \nabla)v, \varphi)_D + \rho(\omega \times v, \varphi)_D$$
$$- (p, \nabla \cdot \varphi)_D + 2\mu(\mathcal{D}(v), \mathcal{D}(\varphi))_D - (\rho|g||\omega|^{-1}\omega, \varphi)_D$$
$$- \varphi_1 \cdot [m_S(|g||\omega|^{-1}\omega - \omega \times V_C)] + \varphi_2 \cdot [\omega \times (I_S \cdot \omega)] - (\nabla \cdot v, q)_D,$$

for arguments $U = \{(v, V_C, \omega), p\}$ and $\Phi = \{(\varphi, \varphi_1, \varphi_2), q\}$. The corresponding derivative which occurs in the dual problem has the form

$$A_1'(U)(\Psi, \Phi) := \rho(((\psi - (\psi_1 + \psi_2 \times y)) \cdot \nabla)v, \varphi))$$
$$+ \rho(((v - (V_C + \omega \times y)) \cdot \nabla)\psi, \varphi) + \rho(\omega \times \psi, \varphi) + \rho(\psi_2 \times v, \varphi)$$
$$- (r, \nabla \cdot \varphi) + 2\mu(D(\psi), D(\varphi)) + \varphi_1 \cdot (\psi_2 \times V_C + \omega \times \psi_1)$$
$$+ \varphi_2 \cdot (\psi_2 \times (I_S \cdot \omega) + \omega \times (I_S \cdot \psi_2)) - (\nabla \cdot \psi, q),$$

for arguments $U = \{(v, V_C, \omega), p\}$, $\Phi = \{(\varphi, \varphi_1, \varphi_2), q\}$, and $\Psi = \{(\psi, \psi_1, \psi_2), r\}$. At first, in order to avoid an overload of technicalities for the derivation, we consider the setup of the simplest Problem 2.8 with the governing semi-linear form

$$A_3(U)(\Phi) := \rho(((v - \alpha_V e_2) \cdot \nabla)v, \varphi)_D - (p, \nabla \cdot \varphi)_D + 2\mu(\mathcal{D}(v), \mathcal{D}(\varphi))_D$$
$$- (\nabla \cdot v, q)_D - (\rho G, \varphi)_D - m_S \varphi_1 e_2 \cdot G.$$

For $U := \{(v, \alpha_V), p\} \in \mathcal{H}_3(D) \times L_0^2(D)$, the target functional for the control of the fall velocity of the body $\mathcal{S}$ is chosen as

$$J_3(U) := \alpha_V, \quad U \in \mathcal{H}_3(D) \times L_0^2(D). \tag{2.2.19}$$

The associated dual problem is given by

$$A_3'(U)(\Phi, Z) = J_3'(U)(\Phi) \quad \forall \Phi \in \mathcal{H}_3(D) \times L_0^2(D), \tag{2.2.20}$$

with the discrete analogue

$$A_3'(U_h)(\Phi_h, Z_h) = J_3'(U_h)(\Phi_h) \quad \forall \Phi_h \in W_3^h. \tag{2.2.21}$$

To the approximate solution $U_h \in W_3^h$ of the discrete Problem 2.11, we associate the residual

$$\rho_3(U_h)(\cdot) := -A_3(U_h)(\cdot). \tag{2.2.22}$$

Then, Proposition 2.2.2 gives us the following result:

Proposition 2.2.3. Let $U := \{(v, \alpha_V), p\} \in \mathcal{H}_3(D) \times L_0^2(D)$ and $Z := \{(z^v, z^\alpha), z^p\} \in \mathcal{H}_3(D) \times L_0^2(D)$ be the solutions of (2.2.5) and (2.2.20), respectively. Further, let U_h and Z_h be their discrete counterparts, i.e., the solutions of (2.2.8) and (2.2.21), respectively. Then, there holds the error representation

$$\alpha_V - \alpha_V^h = \rho_3(U_h)(Z - Z_h) + R_3, \tag{2.2.23}$$

where the remainder R_3 is quadratic in the errors $e^v := v - v_h$ and $e^\alpha := \alpha_V - \alpha_V^h$,

$$R_3 := \rho((e^v \cdot \nabla)e^v, z^v)_D - \rho e^\alpha((e_2 \cdot \nabla)e^v, z^v)_D.$$

Proof. The identity (2.2.23) is a direct consequence of the general error representation (2.2.17) of Proposition 2.2.2. To identify the remainder R_3, we note that

$$A_3''(U_h + sE)(E, E, Z) = 2\rho(((e^v - e^\alpha e_2) \cdot \nabla)e^v, z^v)_D$$
$$J_3''(U_h + sE)(E, E) = 0.$$

This completes the proof. $\qquad\square$

Remark 2.2.4. The dual problem associated to equation (2.2.20) possesses, despite its linear character, a structure similar to the primal Problem 2.8. The natural boundary condition of (2.2.20) is indeed

$$\int\limits_{\partial S} [\sigma(z^v, z^p) \cdot n] \cdot e_2 \, d\sigma = 1. \tag{2.2.24}$$

which should be compared to (2.1.14).

For the more complex setup of Problem 2.6, one can derive an error representation similar to (2.2.23). In that context, however, due to the existence of additional nonlinear terms for the description of the gravitation force $G := |g||\omega|^{-1}\omega$, the remainder becomes much more complicated. In order to control the fall velocity of the solid body $\mathcal{S}$, we choose the functional

$$J_1(U) := \tfrac{1}{2}|V_C|^2, \quad U := \{(v, V_C, \omega), p\} \in \mathcal{H}_1(D) \times L_0^2(D).$$

The associated dual problem is defined as

$$A_1'(U)(\Phi, Z) = J_1'(U)(\Phi) \quad \forall \Phi \in \mathcal{H}_1(D) \times L_0^2(D), \tag{2.2.25}$$

with its discrete analogue

$$A_1'(U_h)(\Phi_h, Z_h) = J_1'(U_h)(\Phi_h) \quad \forall \Phi_h \in W_1^h. \tag{2.2.26}$$

To the approximate solution $u_h \in W_1^h$ of the discrete Problem 2.9, we associate the residual

$$\rho_1(U_h)(\cdot) := -A_1(U_h)(\cdot).$$

Analogously to Proposition 2.2.3, we obtain the following result.

Proposition 2.2.5. Let $U := \{(v, V_C, \omega), p\}$, $Z := \{(z^v, z^{V_C}, z^\omega), z^p\} \in \mathcal{H}_1(D) \times L_0^2(D)$ be the solutions of (2.2.2) and (2.2.25), respectively. Further, let U_h and Z_h be their discrete counterparts in W_1^h, i.e., the solutions of (2.2.6) and (2.2.26), respectively. Then, we have the error representation

$$J_1(U) - J_1(U_h) = \rho_1(U_h)(Z - Z_h) + R_1, \tag{2.2.27}$$

with a remainder R_1 quadratic in the errors $e^v := v - v_h$, $e^{V_C} := V_C - V_C^h$, and $e^\omega := \omega - \omega_h$,

$$\begin{aligned} R_1 :=& \rho((e^v \cdot \nabla)e^v, z^v)_D - \rho((e^{V_C} \cdot \nabla)e^v, z^v)_D - \rho(((e^\omega \times y) \cdot \nabla)e^v, z^v)_D \\ &+ (e^\omega \times e^v, z^v)_D - z^{V_C} \cdot [e^\omega \times e^{V_C}] + z^\omega \cdot [e^\omega \times (I_S \cdot e^\omega)] \\ &- \tfrac{1}{2}|e^{V_C}|^2 + O(|e^\omega|^2). \end{aligned}$$

The term $O(|e^\omega|^2)$ is due to the unknown direction of the gravitational force.

Proof. The error representation (2.2.27) is derived in the same way as that of Proposition 2.2.3. It follows from the error representation derived in Proposition 2.2.2. The expression of the remainder R_1 follows from

$$
\begin{aligned}
A_1''(U_h + sE)(E, E, Z) &= \rho(([e^v - (e^{V_C} + e^\omega \times y)] \cdot \nabla)e^v, z^v)_D \\
&\quad - 2z^{V_C} \cdot [e^\omega \times e^{V_C}] + 2z^\omega \cdot [e^\omega \times (I_S \cdot e^\omega)] + O(|e^\omega|^2), \\
J_1''(U_h + sE)(E, E) &= |e^{V_C}|^2.
\end{aligned}
$$

This completes the proof. □

Notice that Proposition 2.2.5 can be trivially extended to the configuration of Problem 2.7. In that context however, especially for stability analysis of the terminal state, the error control of the orientation of the solid body may be of great interest. Our proposed approach allows indeed to control the orientation of the solid body by means of the functional

$$
J_2(U) := \theta, \quad U := \{(v, V_C), p, \theta\} \in \mathcal{H}_2(D) \times L_0^2(D) \times \mathbb{R}.
$$

The associated dual problem is defined as

$$
A_2'(U)(\Phi, Z) = J_2'(U)(\Phi) \quad \forall \Phi \in \mathcal{H}_2(D) \times L_0^2(D) \times \mathbb{R}, \tag{2.2.28}
$$

as well as its discrete analogue

$$
A_2'(U_h)(\Phi_h, Z_h) = J_2'(U_h)(\Phi_h) \quad \forall \Phi_h \in W_2^h. \tag{2.2.29}
$$

To the approximate solution $U_h \in W_2^h$ of the discrete problem 2.10 we associate the residual

$$
\rho_2(U_h)(\cdot) := -A_2(U_h)(\cdot). \tag{2.2.30}
$$

The discretization error on the orientation of the solid body $\mathcal{S}$ can be estimated by means of the following proposition:

Proposition 2.2.6. Let $U := \{(v, V_C), p, \theta\}$, $Z := \{(z^v, z^{V_C}), z^p, z^\theta\} \in \mathcal{H}_2(D) \times L_0^2(D) \times \mathbb{R}$ be the solutions of (2.2.3) and (2.2.28), respectively. Further, let U_h and Z_h be their discrete counterparts, i.e., the solutions of (2.2.7) and (2.2.29), respectively. Then, there holds

$$
\theta - \theta_h = \rho_2(U_h)(Z - Z_h) + R_2, \tag{2.2.31}
$$

with a remainder R_2 quadratic in the errors $e^v := v - v_h$, $e^{V_C} := V_C - V_C^h$, and $e^\theta := \theta - \theta_h$,

$$
\begin{aligned}
R_2 &:= \rho(((e^v - e^{V_C}) \cdot \nabla)e^v, z^v)_D \\
&\quad + \tfrac{1}{2}|g|\left\{\rho\left(\begin{pmatrix}\cos\theta \\ \sin\theta\end{pmatrix}, z^v\right)_D + m_S\left(\begin{pmatrix}\cos\theta \\ \sin\theta\end{pmatrix} \cdot z^{V_C}\right)\right\}|e^\theta|^2.
\end{aligned}
$$

Proof. The error representation (2.2.31) is a direct consequence of Proposition 2.2.2. To identify the remainder R_2, we note that

$$
\begin{aligned}
A_2''(U_h + sE)(E, E, Z) &= 2\rho(((e^v - e^{V_C}) \cdot \nabla)e^v, z^v)_D \\
&\quad + \rho|g|\left\{\left(\begin{pmatrix}\cos\theta \\ \sin\theta\end{pmatrix}, z^v\right)_D + \rho^{-1}m_S\begin{pmatrix}\cos\theta \\ \sin\theta\end{pmatrix} \cdot z^{V_C}\right\}|e^\theta|^2, \\
J_2''(U_h + sE)(E, E) &= 0.
\end{aligned}
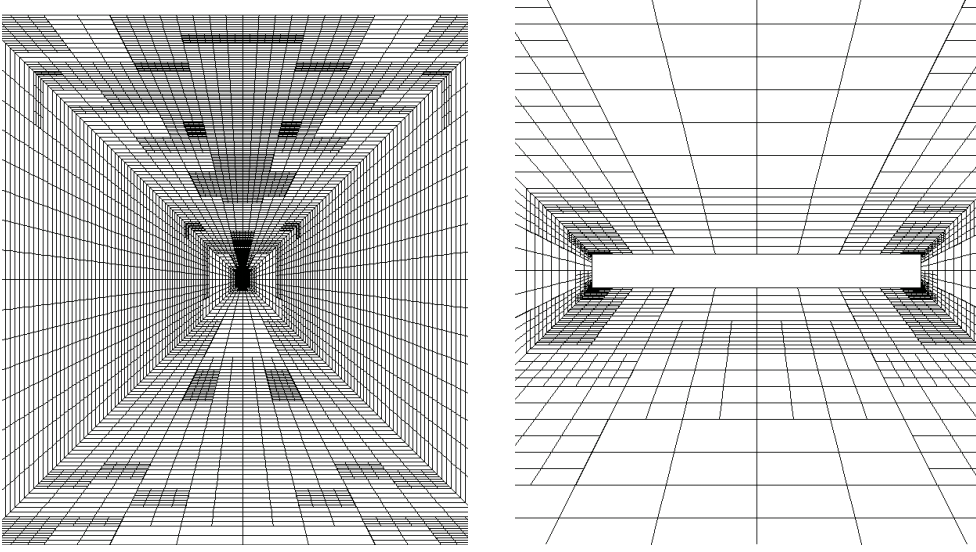$$

This completes the proof. □

Figure 2.7: Adapted meshes - horizontal fall (**left:** D=800, **right:** D=100 (zoom)).

Remark 2.2.7. We note that by the same approach as used above, goal-oriented a posteriori error estimates can also be derived for the hydrodynamical force and torque acting on the solid body $\mathcal{S}$,

$$J_{\psi_1}(U) := \int_{\partial S} [\sigma(v,p) \cdot n] \cdot \psi \, do, \qquad J_{\psi_2 \times y}(U) := \int_{\partial S} y \times [\sigma(v,p) \cdot n] \cdot \psi \, do.$$

This allows for a control of any weighted combination of both quantities. This can be done by an adequate definition of the weights ψ_1 and ψ_2 of the trace $\psi = \psi_1 + \psi_2 \times y$, which determines the Dirichlet boundary condition for the corresponding dual solution, $z^v|_{\partial S} = \psi$.

Figure 2.7 shows some typical adapted meshes obtained by using the DWR approach in the simulation of the 'steady fall problem'.

2.2.5 Hydrodynamic (linear) stability

The stability of solutions $\hat{U} = \{\hat{v}, \hat{p}\}$ of the steady free fall problem can be investigated by the linearized stability theory, i.e., by checking the eigenvalues of the corresponding linearized stability eigenvalue problem,

$$A_1'(\hat{U})(U, \Phi) = \lambda(U, \Phi) \quad \forall \Phi \in \mathcal{H}_1(D) \times L_0^2(D). \tag{2.2.32}$$

If one eigenvalue has real part $\operatorname{Re} \lambda \leq 0$, then the steady-state solution is (dynamically) unstable, i.e., it will not persist under arbitrarily small perturbations. Otherwise, if all eigenvalues have real parts $\operatorname{Re} \lambda > 0$, then the steady-state solution is called 'linearly stable'; see Heuveline/Rannacher [HR06]. The results for the 'free-fall problem' are shown in Table 2.2.

Table 2.2: Results of the stability analysis of the steady-free fall problem for a symmetric rigid rod.

2D case: $\mu = 0.1$	Real part of the critical eigenvalue	
domain diameter	vertical orientation	horizontal orientation
200	-0.82	0.81
800	-1.91	0.61
1000	-1.94	0.84

We see that in the 2D symmetric case for moderate Reynolds number ($\mu = 0.1$), there is one stable (horizontal body orientation) and one unstable (vertical body orientation) solution. For very small Reynolds number, i.e., for $\mu \geq 10^6$ all orientations correspond to (numerically) stable solutions. These findings are in perfect agreement with experimental as well as with theoretical results (see e.g. Galdi [Gal01] and Galdi/Vaidya [GV01] and references cited therein).

3 Artificial boundary conditions for exterior flow problems

The simulation of the motion of a rigid body in a fluid filling the whole space basically requires the solution of the incompressible Navier-Stokes equations in an exterior domain (see Chapter 2). As pointed out in Section 2.2.3, the necessity to truncate for numerical purposes the infinite exterior domain to a finite computational domain leads to the need for artificial boundary conditions on the surface of the truncated domain. Since this problem is of general interest (not only in the context of particulate flow simulations), we devote this chapter to the issue of finding appropriate artificial boundary conditions for exterior flow problems. Following Wittwer [Wit02, Wit03] and Bönisch et al. [BHW05, BHW06] we provide a vector field describing the leading asymptotic behavior of the solution. This vector field is given in the form of an explicit expression depending on a real parameter. We show that this parameter can be determined from the total drag exerted on the body. Using this fact we set up a novel self-consistent numerical scheme that determines the parameter, and hence the boundary conditions and the drag, as part of the solution process.

The chapter is organized as follows: In Section 3.1 we state the (two-dimensional, symmetric) exterior flow problem. In Section 3.2 we show how the results from Wittwer [Wit02, Wit03] can be used to construct an explicit vector field on the artificial boundary and relate the occurring unknown multiplicative constant to the total drag exerted on the body. In Section 3.3 we describe the numerical algorithm that has been used in Bönisch et al. [BHW05, BHW06] to determine the artificial boundary conditions and to solve the exterior flow problem in a consistent way. In Section 3.4 we compare the results obtained using the traditional homogeneous Dirichlet boundary conditions with those obtained from using our adaptive scheme. The difference is impressive: for a given precision the adaptive boundary conditions allow us to take the domain approximately ten times smaller which results in computation times that are more than a factor of hundred shorter. We then use the adaptive boundary conditions to compute the drag for several values of the viscosity, solving in particular also cases which require ridiculously large domains when treated using homogeneous Dirichlet boundary conditions. Section 3.5 briefly discusses how the techniques presented in the previous sections can be extended to the general situation of non-symmetric flows, see also Bönisch et al. [BHW06].
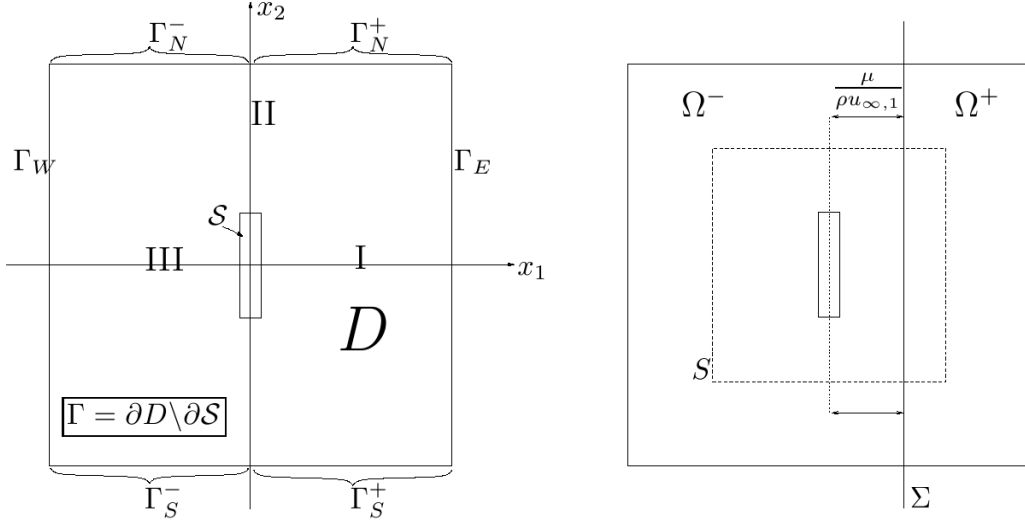
Figure 3.1: Description and notations of the considered exterior flow problem.

3.1 Problem formulation

Consider first a rigid body that is placed into a uniform stream of a homogeneous incompressible fluid, filling all of $\mathbb{R}^2$. This situation is modeled by the Navier-Stokes equations

$$
\begin{aligned}
\rho(u \cdot \nabla)u - \mu \Delta u + \nabla p &= 0 \ , \\
\nabla \cdot u &= 0 \ ,
\end{aligned}
\tag{3.1.1}
$$

in $\Omega = \mathbb{R}^2 \backslash \mathcal{S}$, with $\mathcal{S}$ a compact domain (the body), subject to the boundary conditions $u|_{\partial \mathcal{S}} = 0$ and $\lim_{|x| \to \infty} u(x) = u_\infty$. Here, u is the velocity field, p is the pressure and u_∞ is some constant non-zero vector field which we choose without restriction of generality to be parallel to the x_1-axis, i.e., $u_\infty = (u_{\infty,1}, 0)$ and $u_{\infty,1} > 0$. The density ρ and the dynamic viscosity μ are arbitrary positive constants. For simplicity, we restrict ourselves here to domains and flows that are symmetric with respect to the x_1-axis. The asymmetric case (case with lift) is more complicated (see Section 3.5 and Bönisch et al. [BHW06]).

When solving problem (3.1.1) numerically one is confronted with the necessity to truncate the exterior infinite domain Ω to a finite domain $D \subset \Omega$ (see Figure 3.1). This means, however, that appropriate boundary conditions have to be found on the surface $\Gamma = \partial D \setminus \partial \mathcal{S}$ of the truncated domain. The problem of choosing these so called artificial boundary conditions has only recently been treated in the mathematics literature (see for example Nazarov/Specovius-Neugebauer [NS03]), but has not led to explicit enough prescriptions to be used in numerical work.

Here, using recent results in Wittwer [Wit02, Wit03] we construct an explicit vector field which we use on the boundary of the truncated domain. This vector field involves an unknown multiplicative constant; to fix this constant we use a 'fact' that is well known in the engineering literature, see e.g. Batchelor [Bat67]. Namely, we show that the unknown
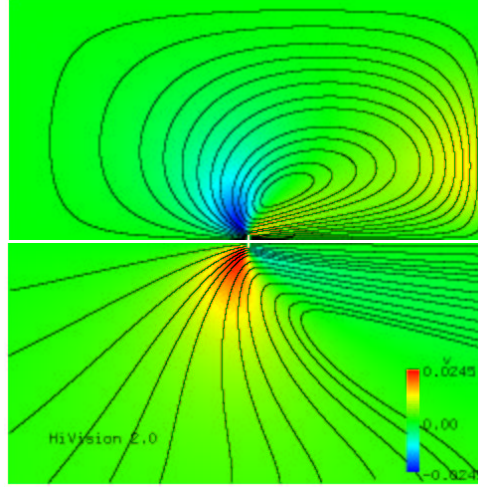
Figure 3.2: Streamlines, upper half: the typical non-physical backflow in the velocity field when imposing homogeneous Dirichlet boundary conditions. Streamlines, lower half: no backflow is created with adaptive boundary conditions. In the background the horizontal component of the flow field is shown.

multiplicative constant is in appropriate units equal to the total drag exerted on the body and can therefore be computed along with the vector field using a self-consistency condition between the imposed boundary condition and the resulting drag. It is this idea that is put into practice below.

The connection of formulation (3.1.1) with particulate flow problems can be readily established as follows: We define $V := -u_\infty$ and $v := u + V$. Then (3.1.1) is obviously equivalent to

$$
\begin{aligned}
\rho((v - V) \cdot \nabla)v - \mu \Delta v + \nabla p = 0 \ , \\
\nabla \cdot v = 0 \ ,
\end{aligned}
\tag{3.1.2}
$$

subject to the boundary conditions $v|_{\partial \mathcal{S}} = V = (-u_{\infty,1}, 0)$ and $\lim_{|x| \to \infty} v(x) = 0$. Hence, (3.1.2) models the purely translational motion of a rigid body in negative x_1-direction through an otherwise quiescent fluid. In the following we will always refer to formulation (3.1.2).

We would like to motivate the study we are going to present in the subsequent sections by showing what happens when homogenous Dirichlet conditions are used for simulating problem (3.1.2) on the truncated computational domain $D \subset \Omega$, see Figure 3.2: An artificial backflow (of small amplitude) has to be created on a big portion of the domain D in order to accommodate for the zero flux condition enforced by homogeneous Dirichlet boundary conditions (see upper half of Figure 3.2). With our adaptive boundary conditions (to be defined later on) the flux through D is 'exactly right', and no portion of the volume D is lost for the computation of a non-physical backflow: the fluid is transported within the wake towards the body, and this fluid is then 'radiated away' from the body by a source-like contribution in the velocity field (see lower half of Figure 3.2), cf. also Batchelor [Bat67].

3.2 Boundary conditions

Let A be a 'typical' length scale of the domain $\mathcal{S}$ (its maximal diameter for example). For bodies $\mathcal{S}$ with smooth boundary $\partial\mathcal{S}$, and for small enough Reynolds number

$$Re = A\rho u_{\infty,1}/\mu \ , \tag{3.2.1}$$

equation (3.1.2) is known to have a (strong) solution $v = (v_1, v_2), p$, see e.g. Galdi [Gal98b]. If $\mathcal{S}$ is symmetric with respect to the x_1-axis this solution is symmetric, i.e., v_1 and p are even functions of x_2 for fixed x_1, and v_2 is an odd function of x_2 for fixed x_1. For large Reynolds numbers there is still no complete answer to the existence problem. Solutions still exist in these cases in a weak sense. These solutions can be constructed by considering equation (3.1.2) on a nested sequence of finite domains D with homogeneous Dirichlet boundary conditions on Γ (see Figure 3.1), see also Nazarov/Specovius-Neugebauer [NS03]. By choosing a convergent subsequence one obtains a limit that satisfies equation (3.1.2) in a weak sense, but not necessarily the boundary condition at infinity.

In Section 3.4 we will numerically solve (3.1.2) for a rectangular body on a nested sequence of square domains with homogeneous Dirichlet boundary conditions. The sequence of these numerical solutions is then compared with solutions obtained using the adaptive boundary conditions that we are going to construct next.

3.2.1 Asymptotic behavior of the solution

Let v be the vector field and p the pressure introduced in (3.1.2). We then scale to dimensionless coordinates $\tilde{x} = x/\ell$, with

$$\ell = \frac{\mu}{u_{\infty,1}\rho} \tag{3.2.2}$$

the viscous length scale of the problem, and introduce the dimensionless vector field $\tilde{v}$ and a dimensionless pressure $\tilde{p}$ by defining $v(x) = u_{\infty,1}\tilde{v}(\tilde{x})$ and $p(x) = \left(\rho u_{\infty,1}^2\right)\tilde{p}(\tilde{x})$. In dimensionless variables equation (3.1.2) becomes

$$\begin{aligned}
((\tilde{v} + e_1)\cdot\nabla)\tilde{v} - \Delta\tilde{v} + \nabla\tilde{p} &= 0 \ , \\
\nabla\cdot\tilde{v} &= 0 \ ,
\end{aligned} \tag{3.2.3}$$

with the Cartesian unit vector $e_1 = (1, 0)^T$. (Derivatives are now taken with respect to the variable $\tilde{x}$.) In Wittwer [Wit02, Wit03] these equations have been studied in the half-space $\Omega^+ = \{(\tilde{x}_1, \tilde{x}_2)\in\mathbb{R}^2\,|\,\tilde{x}_1\geq 1\}$ (see Figure 3.1). Under certain smallness assumptions on the vector field $\tilde{v}$ on Σ (which we expect in particular to be valid for small enough Reynolds numbers), it has been proved that there are numbers c and d and functions $\tilde{v}_1^{(0)}$, $\tilde{v}_2^{(0)}$,

$$\tilde{v}_1^{(0)}(\tilde{x}_1, \tilde{x}_2) = \frac{c}{2\sqrt{\pi}}\frac{1}{\sqrt{\tilde{x}_1}}e^{-\frac{\tilde{x}_2^2}{4\tilde{x}_1}} + \frac{d}{\pi}\frac{\tilde{x}_1}{\tilde{x}_1^2 + \tilde{x}_2^2} \ , \tag{3.2.4}$$

$$\tilde{v}_2^{(0)}(\tilde{x}_1, \tilde{x}_2) = \frac{c}{4\sqrt{\pi}}\frac{\tilde{x}_2}{\tilde{x}_1^{3/2}}e^{-\frac{\tilde{x}_2^2}{4\tilde{x}_1}} + \frac{d}{\pi}\frac{\tilde{x}_2}{\tilde{x}_1^2 + \tilde{x}_2^2} \ , \tag{3.2.5}$$

such that

$$\lim_{\tilde{x}_1 \to \infty} \tilde{x}_1^{1/2} \left(\sup_{\tilde{x}_2 \in \mathbb{R}} |(\tilde{v}_1 - \tilde{v}_1^{(0)})(\tilde{x}_1, \tilde{x}_2)| \right) = 0 \; , \tag{3.2.6}$$

$$\lim_{\tilde{x}_1 \to \infty} \tilde{x}_1 \left(\sup_{\tilde{x}_2 \in \mathbb{R}} |(\tilde{v}_2 - \tilde{v}_2^{(0)})(\tilde{x}_1, \tilde{x}_2)| \right) = 0 \; . \tag{3.2.7}$$

Moreover,

$$\int_{\mathbb{R}} \tilde{v}_1(\tilde{x}_1, \tilde{x}_2) \, d\tilde{x}_2 = \int_{\mathbb{R}} \tilde{v}_1^{(0)}(\tilde{x}_1, \tilde{x}_2) \, d\tilde{x}_2 = c + d \; , \tag{3.2.8}$$

independently of $\tilde{x}_1 \geq 1$. Equations (3.2.6) and (3.2.7) express the fact that asymptotically, for large values of $\tilde{x}_1$, the vector field $\tilde{v} = (\tilde{v}_1, \tilde{v}_2)$ is to leading order given by the vector field $\tilde{v}^{(0)} \equiv (\tilde{v}_1^{(0)}, \tilde{v}_2^{(0)})$, and (3.2.8) shows that the flux through vertical lines is constant and entirely described by the dominant term $\tilde{v}_1^{(0)}$. The vector field $\tilde{v}^{(0)}$ therefore gives an explicit description of the asymptotic flow downstream of the body as the sum of two divergence-free contributions: a parabolic wake term (multiplied by c), and a compensating source term (multiplied by d). Note that the asymptotic behavior $\tilde{v}^{(0)}$ is *universal* in the sense that this asymptotic is independent of the geometry of the body, except for the amplitudes c and d. In original coordinates x we get

$$v_1^{(0)}(x_1, x_2) = \left(u_{\infty,1} \sqrt{\ell} \right) \frac{c}{2\sqrt{\pi}} \frac{1}{\sqrt{x_1}} e^{-\frac{x_2^2}{4\ell x_1}} + (u_{\infty,1} \ell) \frac{d}{\pi} \frac{x_1}{x_1^2 + x_2^2} \; , \tag{3.2.9}$$

$$v_2^{(0)}(x_1, x_2) = \left(u_{\infty,1} \sqrt{\ell} \right) \frac{c}{4\sqrt{\pi}} \frac{x_2}{x_1^{3/2}} e^{-\frac{x_2^2}{4\ell x_1}} + (u_{\infty,1} \ell) \frac{d}{\pi} \frac{x_2}{x_1^2 + x_2^2} \; . \tag{3.2.10}$$

Remark 3.1. The expressions (3.2.9),(3.2.10) for $v_1^{(0)}$ and $v_2^{(0)}$ are not yet applicable for practical numerical computations since the two constants c and d are still unknown. In the next section we will show that asymptotically, $d = -c/2$ and that the constant c can be related to the total drag exerted on the body.

3.2.2 Adaptive boundary conditions

We now define the vector field $v^{ABC} = (v_1^{ABC}, v_2^{ABC})$ that we use on the boundary $\Gamma = \bigcup_X \Gamma_X$ (see Figure 3.1). Namely, for $(x_1, x_2) \in D$, $x_1 > 0$ (and therefore in particular on Γ_E and on Γ_N^+ and Γ_S^+) we set

$$v_1^{ABC}(x_1, x_2) = v_1^{(0)}(x_1, x_2) \; , \tag{3.2.11}$$

$$v_2^{ABC}(x_1, x_2) = v_2^{(0)}(x_1, x_2) \; , \tag{3.2.12}$$

with $v_1^{(0)}$ and $v_2^{(0)}$ as defined in (3.2.9), (3.2.10), while for $(x_1, x_2) \in D$, $x_1 \leq 0$ (and therefore in particular on Γ_W and on Γ_N^- and Γ_S^-) we set

$$v_1^{ABC}(x_1, x_2) = (u_{\infty,1} \ell) \frac{d}{\pi} \frac{x_1}{x_1^2 + x_2^2} \; , \tag{3.2.13}$$

$$v_2^{ABC}(x_1, x_2) = (u_{\infty,1} \ell) \frac{d}{\pi} \frac{x_2}{x_1^2 + x_2^2} \; . \tag{3.2.14}$$

This definition of the artificial boundary conditions is well motivated by (3.2.6), (3.2.7) on Γ_E^+ and on those parts of the boundary Γ_N^+ and Γ_S^+ where $x_1 \gg 1$. For large enough domains D, the contribution of the wake-term (term multiplied by c) on Γ_N^+ and Γ_S^+ is negligible with respect to the source term (term multiplied by d), so that asymptotically v^{ABC} is given by (3.2.13), (3.2.14) on all of $\Gamma \setminus \Gamma_E$. The wake term on Γ_N^+ and Γ_S^+ interpolates smoothly between the asymptotic behavior for large values of x_1 and the boundary conditions on Γ_N^- and Γ_S^-.

We now determine the unknown multiplicative constants occurring in (3.2.9),(3.2.10). To this end we consider as in Figure 3.1, an arbitrary rectangle $[-l, l] \times [-L, L]$ with surface $S = S(l, L)$ containing the body $\mathcal{S}$. Since the total flux of the constant vector field $v|_{\partial \mathcal{S}} = -u_\infty$ through $\partial \mathcal{S}$ is zero and since the vector field v is divergence-free, it follows using Gauß's theorem that the total flux through S has to be zero as well. For the vector field v^{ABC} (which is divergence-free, too) we must therefore impose that $\int_{S(l,L)} v^{ABC} \cdot n \, do = 0$ for all l, L. Keeping l fixed while letting L tend to infinity, we find using (3.2.8), that

$$
\begin{aligned}
0 &= \lim_{L \to \infty} \int_{S(l,L)} v^{ABC} \cdot n \, do \\
&= \lim_{L \to \infty} [\int_{-L}^{L} (v_1^{ABC}(l, x_2) - v_1^{ABC}(-l, x_2)) \, dx_2 \\
&\quad + \int_{-l}^{l} (v_2^{ABC}(x_1, L) - v_2^{ABC}(x_1, -L)) \, dx_1] \\
&= \lim_{L \to \infty} \int_{-L}^{L} (v_1^{ABC}(l, x_2) - v_1^{ABC}(-l, x_2)) \, dx_2 \\
&= (u_{\infty,1} \ell)(c + 2d) .
\end{aligned}
\tag{3.2.15}
$$

We obtain from (3.2.15) that the two constants c and d in (3.2.9),(3.2.10) are connected by the relation

$$
d = -\frac{c}{2}.
\tag{3.2.16}
$$

To get an expression for c we integrate the Navier-Stokes equation over S (see Batchelor [Bat67]). We assume that $v - v^{ABC}$ satisfies a bound similar to (3.2.6), (3.2.7) not only in the wake region but everywhere on S, and that[1] $p \approx p^{ABC} = -\frac{1}{2}\left((v_1^{ABC})^2 + (v_2^{ABC})^2\right)$, asymptotically as S converges to infinity. For the total drag F on the body we get that

---

[1] The following expression for p^{ABC} is a consequence of *Bernoulli's* theorem for inviscid irrotational flows. It is applicable in the region outside the wake because the flow there is close to potential flow.

(terms that vanish as $l \to \infty$ are omitted)

$$F = \lim_{L \to \infty} - \int_{-L}^{L} \left[\left(p^{ABC}(l, x_2) + \rho \, v_1^{ABC}(l, x_2)^2 \right) \right.$$
$$\left. - \left(p^{ABC}(-l, x_2) + \rho \, v_1^{ABC}(-l, x_2)^2 \right) \right] \, dx_2$$
$$= -2 \left(\rho u_{\infty,1}^2 \ell \right) \, (c + d)$$
$$= - \left(\rho u_{\infty,1}^2 \ell \right) \, c \, ,$$

in other words:

$$c = -\frac{1}{\rho \ell u_{\infty,1}^2} F \, . \tag{3.2.17}$$

This completes the definition of the adaptive boundary conditions.

3.3 Solution process

The specificity of our approach to solve exterior flow problems like (3.1.2) is to prescribe artificial boundary conditions which depend on the drag, cf. the previous section. The drag however, and therefore the adequate boundary conditions, are clearly not known at the beginning of the solution process. Therefore we embed the solution of the Navier-Stokes equations in an additional fixed-point iteration which determines the drag through successive updates of the boundary conditions based on the previously computed drag. This adaptive procedure yields a consistent approximation of the boundary conditions and the flow field.

In the following we describe the two main components of this algorithm. The solution of the Navier-Stokes problem (3.1.2) on a truncated computational domain by means of the Galerkin finite element method is explained in Section 3.3.1. The accurate computation of the drag exerted by the fluid on the body (which is clearly a crucial issue in our scheme) is treated in Section 3.3.2.

3.3.1 Galerkin finite element discretization

We begin with some standard notation. For a domain $\Omega \subset \mathbb{R}^2$, let $L^2(\Omega)$ denote the Lebesgue space of square-integrable functions on Ω equipped with the inner product and norm

$$(f, g)_\Omega = \int_\Omega fg \, dx, \qquad ||f||_\Omega = (f, f)_\Omega^{1/2}.$$

The pressure is assumed to lie in the space $L_0^2(\Omega) := \left\{ q \in L^2(\Omega) : \int_{\Omega'} q = 0, \text{ for all bounded } \Omega' \subset \Omega \right\}$, which defines it uniquely. The $L^2(\Omega)$ functions with generalized (in the sense of distributions) first-order derivatives in $L^2(\Omega)$ form the Sobolev space $H^1(\Omega)$, while $H_0^1(\Omega) = \left\{ v \in H^1(\Omega), v|_{\partial \Omega} = 0 \right\}$.

The Galerkin finite element discretization of problem (3.1.2) starts from a variational formulation. Let $W = [H_{loc}^1(\Omega)]^2 \times L_0^2(\Omega)$. For $U = \{v, p\} \in W$ and $\Phi = \{\varphi, q\} \in W$, we define the semi-linear form

$$A(U)(\Phi) := \rho(((v - V) \cdot \nabla)v, \varphi)_\Omega - (p, \nabla \cdot \varphi)_\Omega + 2\mu(\mathcal{D}(v) : \mathcal{D}(\varphi))_\Omega - (\nabla \cdot v, q)_\Omega, \quad (3.3.1)$$

where $\mathcal{D}$ denotes the deformation tensor, i.e. $\mathcal{D}(v) = \frac{1}{2}(\nabla v + (\nabla v)^T)$. A weak form of the equations (3.1.2) then reads as follows:

Find $U = \{v, p\} \in W$, such that

$$A(U)(\Phi) = 0, \quad \forall \Phi \in W. \tag{3.3.2}$$

In order to solve (3.3.2) numerically by a Galerkin finite element method, the unbounded domain Ω is replaced by a bounded domain $D \subset \Omega$. The discretization uses a conforming finite element space $W_h \subset W$ defined on quasi-uniform triangulations $\mathbb{T}_h = \{K\}$ consisting of quadrilateral (or hexahedral in 3D) cells K covering the domain D (see Figure 3.3). For the trial and test spaces $W_h \subset [H_0^1(D)]^2 \times L_0^2(D)$ we consider the standard 'Hood-Taylor' finite element, see Hood/Taylor [HT73], i.e., we define

$$W_h := \left\{ (v, p) \in [C(\overline{D})]^3; \quad v|_K \in [Q_2]^2, p|_K \in Q_1 \right\},$$

where Q_r describes the space of isoparametric tensor-product polynomials of degree r (for a detailed description of this standard construction process see for example Brenner/Scott [BS94]). This choice for the trial and test functions has the advantage that it guarantees a stable approximation of the pressure since the *Babuska-Brezzi* ('inf-sup') stability condition is satisfied uniformly in h (see e.g. Brezzi/Falk [BF91] and references therein). The advantage, when compared to equal order function spaces for the pressure and the velocity is that no additional stabilization terms are needed. The discrete counterpart of problem (3.3.2) then reads:

Find $U_h = \{v_h, p_h\} \in \left[v_h^\partial + H_0^1(D)^2\right] \times L_0^2(D)$, such that

$$A(U_h)(\Phi_h) = 0, \quad \forall \Phi_h \in W_h. \tag{3.3.3}$$

Here v_h^∂ denotes the prescribed Dirichlet data on the boundary $\Gamma \cup \partial \mathcal{S}$ of the domain D. It has been the goal of the discussion in Section 3.2 to formulate adequate non-homogeneous Dirichlet boundary conditions on Γ which correspond to the asymptotic behavior of v. As already mentioned, these boundary conditions are independent of the details of the geometry of the body, but depend on the drag. The accurate computation of this quantity is therefore an important issue, cf. the next section.

The nonlinear algebraic system (3.3.3) is solved implicitly in a fully coupled manner by means of a damped Newton method. Denoting the derivative of $A(\cdot)(\cdot)$ at a discrete function $U_h \in W_h$ in direction w by $A'(U_h)(w, \cdot)$, the linear system arising at the Newton step number k has the following form,

$$A'(U_h^{(k)})(w_h^{(k)}, \Phi_h) = (r_h^{(k)}, \Phi_h), \quad \forall \Phi_h \in W_h, \tag{3.3.4}$$

where $r_h^{(k)}$ is the equation residual of the preceding approximation $U_h^{(k)}$, and $w_h^{(k)}$ corresponds

to the correction. The updates $U_h^{(k+1)} = U_h^{(k)} + \alpha^{(k)} w_h^{(k)}$ with a relaxation parameter $\alpha^{(k)}$ chosen by means of Armijo's rule are carried out until convergence. It is well known that the ability of the Newton iteration to converge quadratically greatly depends on the quality of the initial approximation. In order to find such an initial approximation, we consider a mesh hierarchy $\{\mathbb{T}_{h_l}\}_l$ with $\mathbb{T}_{h_l} \subset \mathbb{T}_{h_{l+1}}$, and the corresponding system of equations (3.3.3) is successively solved by taking advantage of the previously computed solution, i.e., the nonlinear Newton steps are embedded in a *nested iteration* process (see e.g. Wesseling [Wes92], Chapter 8).

The linear subproblems (3.3.4) are solved by the *Generalized Minimal Residual Method (GMRES)* (see Saad [Saa96]) preconditioned by means of multigrid iteration (see Wesseling [Wes92] and references therein for the description of the different multigrid techniques for flow simulations). For further algorithmic details we refer the reader to Bönisch et al. [BHW05, BHW06]. The implementation was done with **HiFlow**, see [Heu06].

3.3.2 Accurate computation of the drag

Let $\sigma(v, p) = -pI + 2\mu \mathcal{D}(v)$ denote the stress tensor. The force acting on the rigid body $\mathcal{S}$ in direction ψ on $\partial \mathcal{S}$ is given by

$$N_\psi(U) = \int_{\partial \mathcal{S}} (\sigma(v, p) \cdot n) \cdot \psi \, do, \qquad (3.3.5)$$

where $U = (v, p)$, $\psi \in [H^{1/2}(\partial \mathcal{S})]^2$ and n is the unit outward normal to $\partial \mathcal{S}$. If ψ is a unit vector parallel (resp. perpendicular) to the flow direction, then $N_\psi(U)$ is referred to as the drag (resp. lift). Let $\tilde{\psi} \in H^1(D)$ be defined such that

$$\tilde{\psi} = \psi \ \text{ on } \ \partial \mathcal{S}, \qquad \tilde{\psi} = 0 \ \text{ on } \ \Gamma. \qquad (3.3.6)$$

Applying Green's identity to the integral (3.3.5) leads to the equality

$$N_\psi(U) = A(U)(\tilde{\psi}). \qquad (3.3.7)$$

Expression (3.3.7) holds for any smooth U and for any choice of $\tilde{\psi}$ fulfilling the condition (3.3.6). We impose $\tilde{\psi} \in W_h$. Motivated by formula (3.3.7) we define the discrete counterpart N_ψ^h of N_ψ by

$$N_\psi^h(U_h) := A(U_h)(\tilde{\psi}). \qquad (3.3.8)$$

Again, under assumption (3.3.6), the right-hand side of (3.3.8) is independent of the choice of $\tilde{\psi} \in W_h$ and N_ψ^h is therefore well-defined. It is important to note that, in general,

$$N_\psi^h(U_h) \neq N_\psi(U_h).$$

Based on the Babuška-Miller trick [BM84a, BM84b, BM84c], Giles et al. proved in [GLL$^+$97] that $N_\psi^h(U_h)$ is indeed the adequate formulation for the computation of the drag. Assuming boundaries which are sufficiently smooth, they show that the order of convergence of $N_\psi^h(U_h)$ to $N_\psi(U)$ is $O(h^4)$ which is to be compared to an order of convergence of typically $O(h^2)$ for the direct approximation of N_ψ. A typical example is shown in Table 3.1 which makes clear that the evaluation of the drag via formulation (3.3.8) is essential in order to attain the desired high accuracy at reasonable computational costs.

Level	# Unknowns	drag computed by means of	
		$N_{\psi}^h(U_h)$	$N_{\psi}(U_h)$
3	18,592	0.0504563	0.0522906
4	74,048	0.0503341	0.0516217
5	295,552	0.0503143	0.0512033
6	1,180,928	0.0503102	0.0509204

Table 3.1: Convergence records of the drag computed using formulations $N_{\psi}^h(U_h)$ and $N_{\psi}(U_h)$, resp. We refer to Section 3.4 for the description of the considered configuration. The computational domain has a diameter that is eight hundred times bigger than that of the rigid body.

3.4 Numerical experiments

The goal of this section is twofold. On one hand we compare, for a given configuration of the flow, the solution obtained by means of the newly proposed boundary conditions (see Section 3.2) with the solution obtained by means of homogeneous Dirichlet boundary conditions. This first step confirms the theoretical results in Wittwer [Wit02, Wit03] and gives numerical evidence of the validity of our approach. On the other hand, quantitative results depicted for different Reynolds numbers clearly show the generally drastic improvements in numerical efficiency when using the proposed boundary conditions.

As a model problem we consider a rectangle $[-0.1, 0.1] \times [-0.5, 0.5]$ which is moving through a homogeneous incompressible fluid with density $\rho = 1$ and dynamic viscosity $\mu = 0.1$. Further we impose a translational velocity $V = (-0.1, 0)$, i.e. $u_{\infty,1} = 0.1$. With $A = 1$ being the length of the rectangle, we find from (3.2.1) for the Reynolds number corresponding to this configuration,

$$Re = \frac{A \, \rho \, u_{\infty,1}}{\mu} = 1. \tag{3.4.1}$$

Concerning the computational domain D we restrict ourselves to square-shaped domains. Due to limitations inherent to the solver, the aspect ratio τ of the considered meshes does not exceed $\tau = 30$. Typical meshes corresponding to this setup are depicted in Figure 3.3.

We now discuss various ways of comparing the numerical solutions $v = (v_1, v_2)$ of (3.1.2) (obtained with Dirichlet and adaptive boundary conditions) with the theoretical predictions. We start by considering the wake region, where we have the most precise results (see Wittwer [Wit03]). A quantity which has been intensively studied (see for example Stewartson [Ste57]) is the so called centerline velocity $v(x_1, 0)$ (see Figure 3.1 for the definition of the cut-lines 'cut I', 'cut II', and 'cut III'). Since v_1 is even and v_2 is odd in x_2 we have that $v_2(x_1, 0) = 0$ for all x_1, and we therefore only need to consider $v_1(x_1, 0)$. The theoretical prediction (3.2.9), (3.2.17), (3.2.16) is that, to leading order for large x_1,

$$v_1(x_1, 0) \approx \left(u_{\infty,1} \sqrt{\ell} \right) \frac{c}{2\sqrt{\pi}} \frac{1}{\sqrt{x_1}} \, , \tag{3.4.2}$$
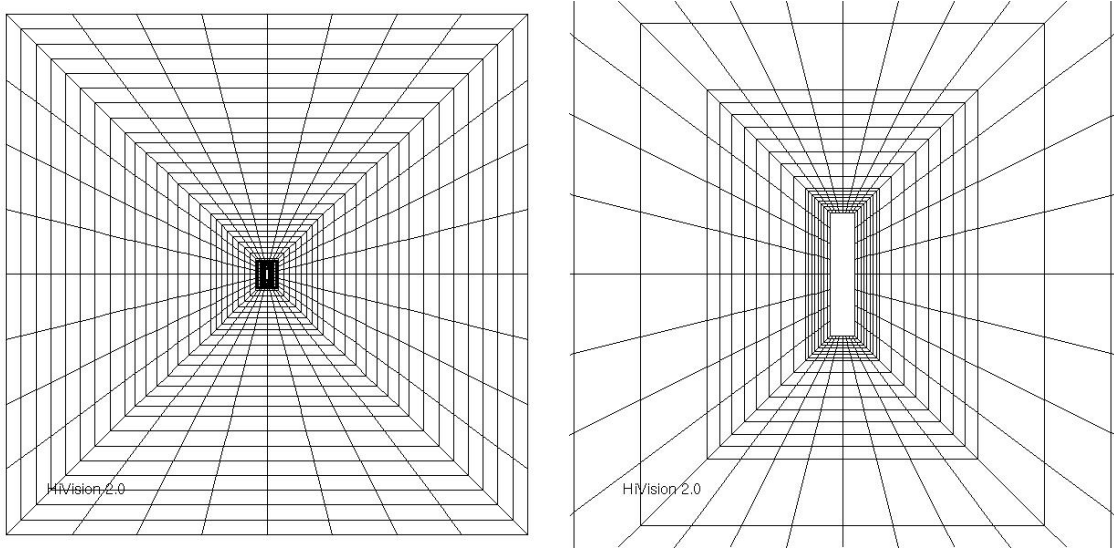
Figure 3.3: Left: Triangulation of the computational domain D after three refinement steps. The diameter of D is equal to $d = 50$. **Right:** Zoom on the mesh around the rigid body $\mathcal{S}$.

with

$$c = -\frac{1}{\rho \ell u_{\infty,1}^2} F \ . \tag{3.4.3}$$

In Figure 3.4 we have plotted the quantity $-2\sqrt{\pi}\sqrt{x_1}v_1(x_1, 0)$ as a function of x_1, where v_1 has been computed, once using homogeneous Dirichlet boundary conditions and once using our adaptive scheme. Numerically we find that $F = 0.05031$. We therefore expect using (3.4.2) that $-2\sqrt{\pi}\sqrt{x_1}v_1(x_1, 0) \approx - \left(u_{\infty,1}\sqrt{\ell} \right) c = 0.5031$ for large values of x_1. As Figure 3.4 shows, the solution with Dirichlet boundary conditions indeed appears to converge to this value, but most of the computational domain is lost for the interpolation between this correct asymptotic value and the value zero imposed by the boundary conditions. With the adaptive boundary conditions only minor (higher order) corrections are necessary when arriving to the boundary, the plot being close to the asymptotic value on most of the domain.

On cut II, perpendicular to the body, both components of v are non-zero, but the v_2-component is asymptotically dominant. The theory (3.2.14), (3.2.16), (3.2.17) predicts that, asymptotically, for large values of x_2,

$$v_2(0, x_2) \approx - (u_{\infty,1}\ell) \frac{c}{2\pi} \frac{1}{x_2} \ , \tag{3.4.4}$$

with c again given by (3.4.3). In Figure 3.5 we have plotted the quantity $2\pi x_2 v_2(0, x_2)$ as a function of x_2, and v_2 has been computed using Dirichlet boundary conditions and using the adaptive scheme. From (3.4.4) we expect that $2\pi x_2 v_2(0, x_2) \approx - (u_{\infty,1}\ell) c = 0.5031$ for large values of x_2. Indeed, for values of x_2 that are large compared to the size of $\mathcal{S}$, but small compared to the size of the computational domain (i.e., $x_2 \approx 100$) the graphs in Figure 3.5
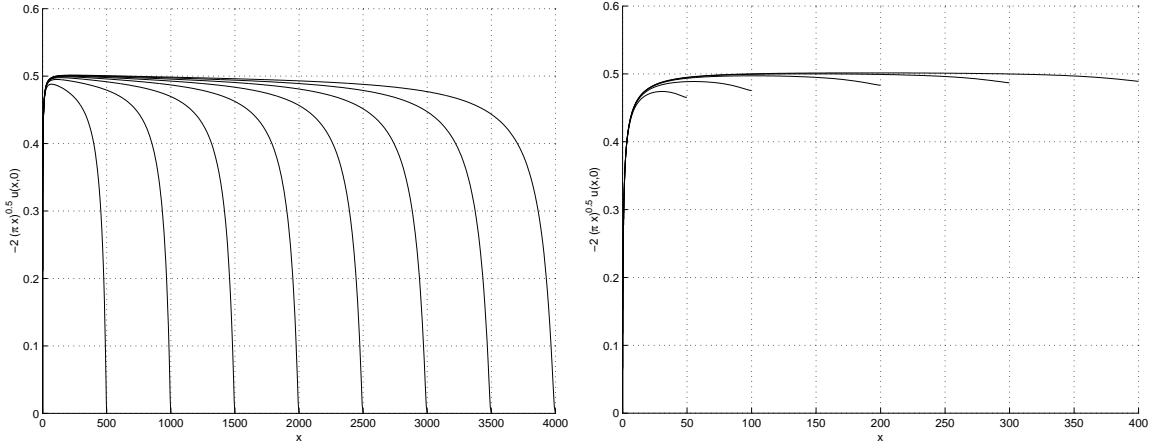
Figure 3.4: Scaled v_1-component along 'cut I', considering homogeneous Dirichlet boundary conditions (**left**) and the proposed adaptive boundary conditions (**right**). For the homogeneous Dirichlet (resp. adaptive) boundary conditions the size of the diameter of the computational domain D varies in the range $d \in [1000; 8000]$ (resp. $d \in [100; 800]$). The velocity profile on 'cut I' (which is defined in Figure 3.1) reveals the asymptotics in the wake.

appear to level off at a value compatible with the theoretical prediction, but then rapidly go to zero, in a domain-dependent way, as required by the Dirichlet boundary conditions. In the adaptive scheme the asymptotic value is enforced at the boundary, and we get, with increasing computational domains, a sequence of graphs that appear to converge to some limiting graph that is consistent with the asymptotic prediction (3.4.4).

On cut III, finally, the v_2-component is again zero and for v_1 we have the prediction that, asymptotically, for large negative values of x_1,

$$v_1(x_1, 0) \approx -(u_{\infty,1}\ell)\,\frac{c}{2\pi}\frac{1}{x_1}\;,\tag{3.4.5}$$

with c as above. In Figure 3.6 we have plotted the quantity $2\pi x_1 v_1(x_1, 0)$ as a function of x_1. For this cut the results are even more drastic. For the adaptive boundary conditions we get a sequence of graphs that converge quite clearly to some limiting graph which is moreover compatible with the asymptotic prediction (3.4.5). The sequence of graphs for Dirichlet boundary conditions does not converge at all for this case, but depends on the whole range of volumes very strongly on the boundary condition.

We conclude that, as expected, physically interesting quantities (in particular the drag) can a priori be computed using Dirichlet boundary conditions, but only by choosing the computational domain ridiculously large in order to leave 'sufficient room' to accommodate for the non-physical backflow. The computation times are accordingly exceedingly large, so that some of these computations are in practice unfeasible.

This issue which is essential for the numerical simulation is depicted, quantitatively, in Figure 3.7. On this plot the relative error of the drag as a function of the domain diameter is
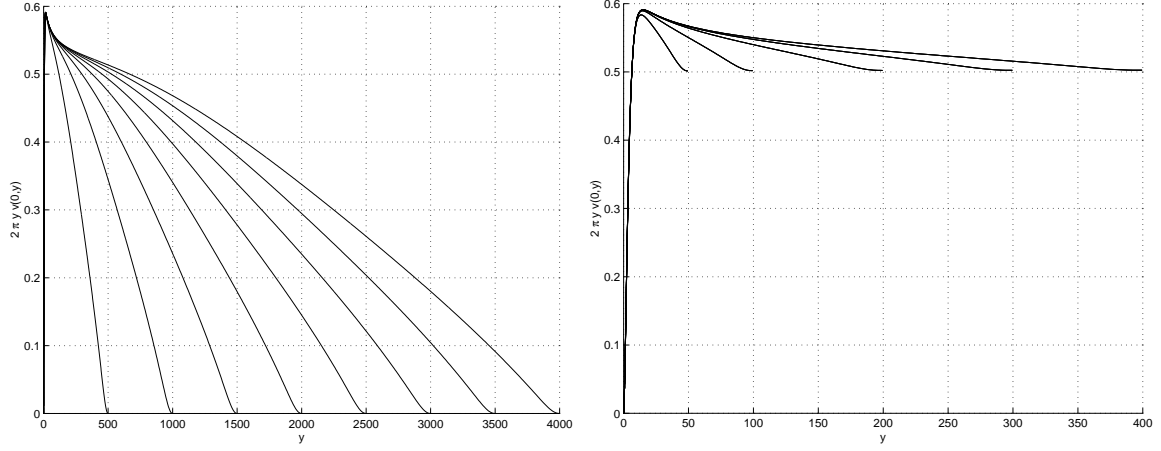
Figure 3.5: Scaled v_2-component along 'cut II' considering homogeneous Dirichlet boundary conditions (**left**) and the proposed adaptive boundary conditions (**right**). For homogeneous Dirichlet (resp. adaptive) boundary conditions the size of the diameter of the computational domain D varies in the range $d \in [1000; 8000]$ (resp. $d \in [100; 800]$). 'Cut II' is defined in Figure 3.1.
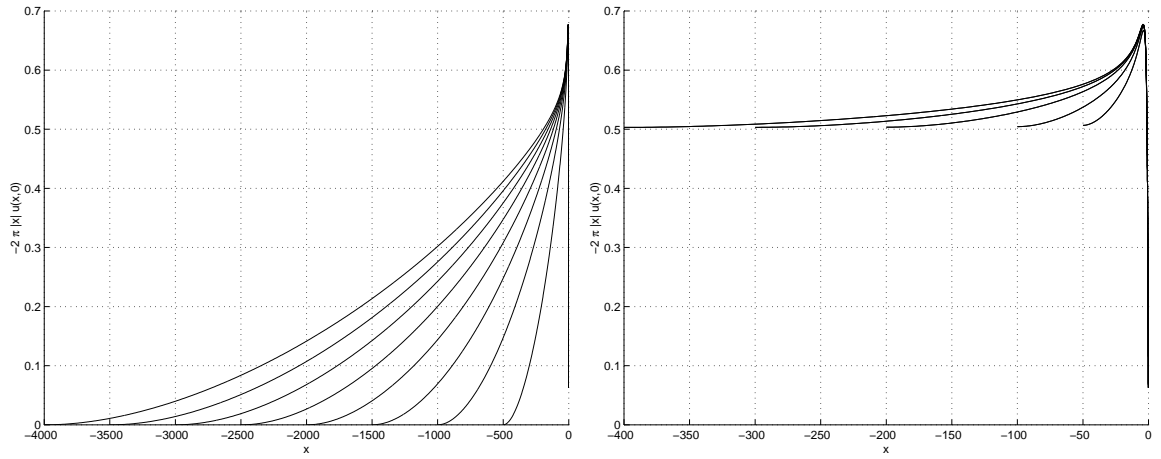

Figure 3.6: Scaled v_1-component along 'cut III', considering homogeneous Dirichlet boundary conditions (**left**) and the proposed adaptive boundary conditions (**right**). For the homogeneous Dirichlet (resp. adaptive) boundary conditions the size of the diameter of the computational domain D varies in the range $d \in [1000; 8000]$ (resp. $d \in [100; 800]$). 'Cut III' is defined in Figure 3.1.
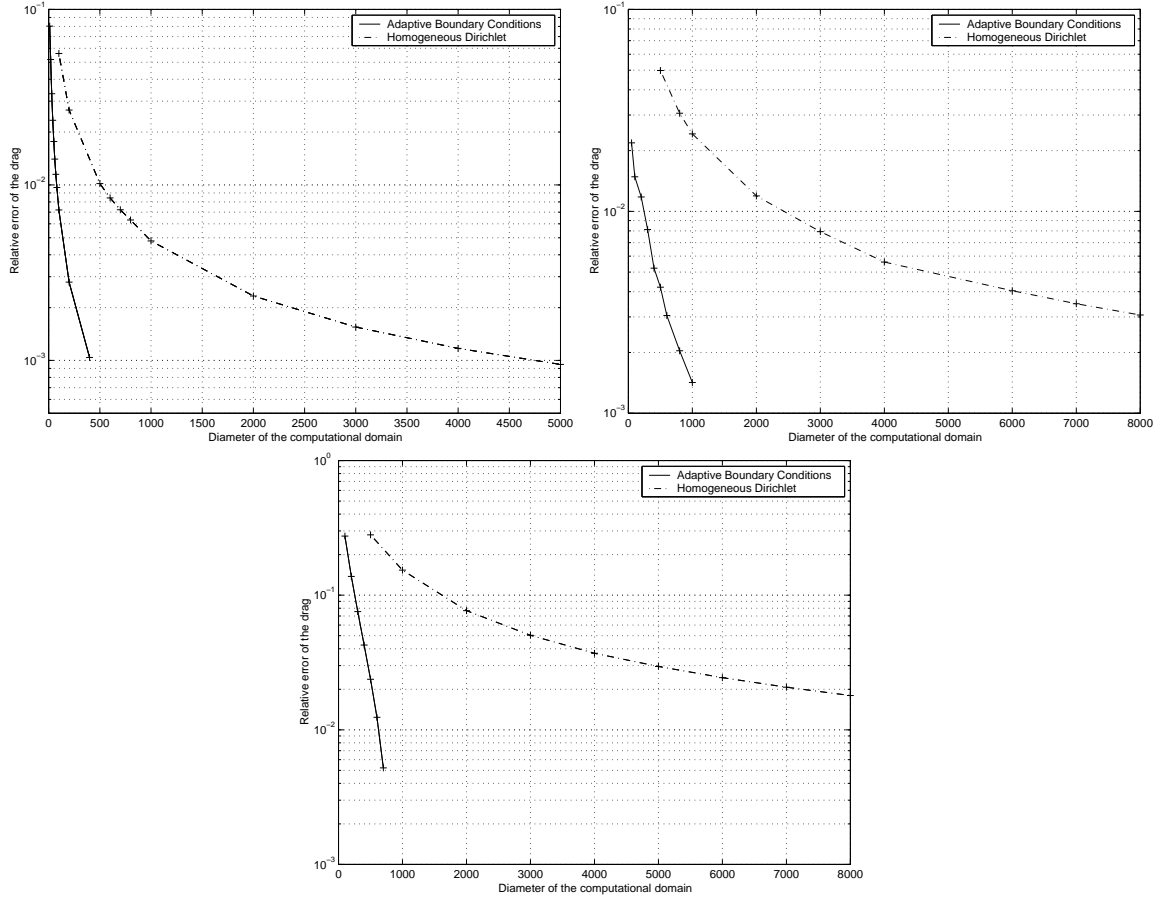
Figure 3.7: Plot of the relative error of the drag as a function of the domain diameter, comparing homogeneous Dirichlet boundary conditions and the proposed adaptive boundary conditions. The plotted configurations correspond to $\mu = 0.1$ ($Re = 1$, **top left**), $\mu = 1$ ($Re = 0.1$, **top right**) and $\mu = 10$ ($Re = 0.01$, **bottom**).

shown considering homogeneous Dirichlet boundary conditions and the proposed adaptive boundary conditions for $\mu = 0.1$ ($Re = 1$), $\mu = 1$ ($Re = 0.1$) and $\mu = 10$ ($Re = 0.01$). For $\mu = 0.1$ ($Re = 1$), a relative error of the drag equal to $0.5 \cdot 10^{-2}$ can be obtained using adaptive boundary conditions on a domain of diameter equal to $d_{ABC} = 100$ which has to be compared to a domain diameter equal to $d_{Dir} = 1000$ needed for the homogeneous Dirichlet case. For $\mu = 1$ ($Re = 0.1$), the same relative error can be attained for $d_{ABC} = 450$ which has to be compared to $d_{Dir} = 4500$. For $\mu = 10$ ($Re = 0.01$), the discrepancy is even bigger since the relative error obtained for $d_{ABC} = 700$ could not be obtained on domains with diameter less than 8000 for the homogeneous Dirichlet case. These results clearly illustrate the considerable increase of numerical efficiency associated with the proposed adaptive scheme.

Having established the validity of the adaptive scheme, we now present some additional results that illustrate in some more detail the basic ideas of our approach. All numerical results for this section have been established with our standard configuration and $\mu = 0.1$ ($Re = 1$).
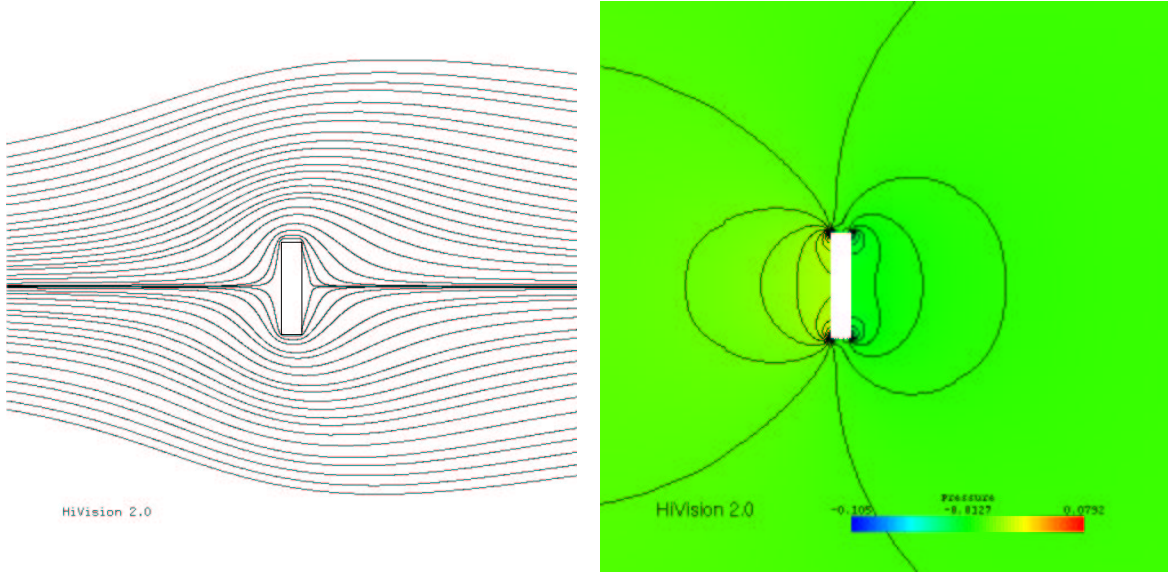
Figure 3.8: Streamlines (**left**) and pressure (**right**) around the body for the configuration described in the text.

First, in Figure 3.8 the streamlines of the vector field $u = v - V$, (the solution of (3.1.1)) are shown. In contrast to streamlines computed with homogeneous Dirichlet boundary conditions, which are forced to be perpendicular to the wall when entering and leaving the domain, no such non-physical deformations occur with the adaptive scheme. The same is true for the pressure isobars (see Figure 3.8, right).

We next discuss Figure 3.9 which shows the vorticity $\omega(x_1, x_2) = -\partial_2 v_1(x_1, x_2) + \partial_1 v_2(x_1, x_2)$. The lines of constant vorticity join the right boundary perfectly natural. No deformation can be observed near the border. One also clearly sees that the vorticity is basically zero outside a rather small region around the object and outside the wake. In Figure 3.10 we have plotted the vorticity on vertical lines just before, after and somewhat more downstream of the object. As can be clearly seen the vorticity decays extremely rapidly in the directions transverse to the flow.

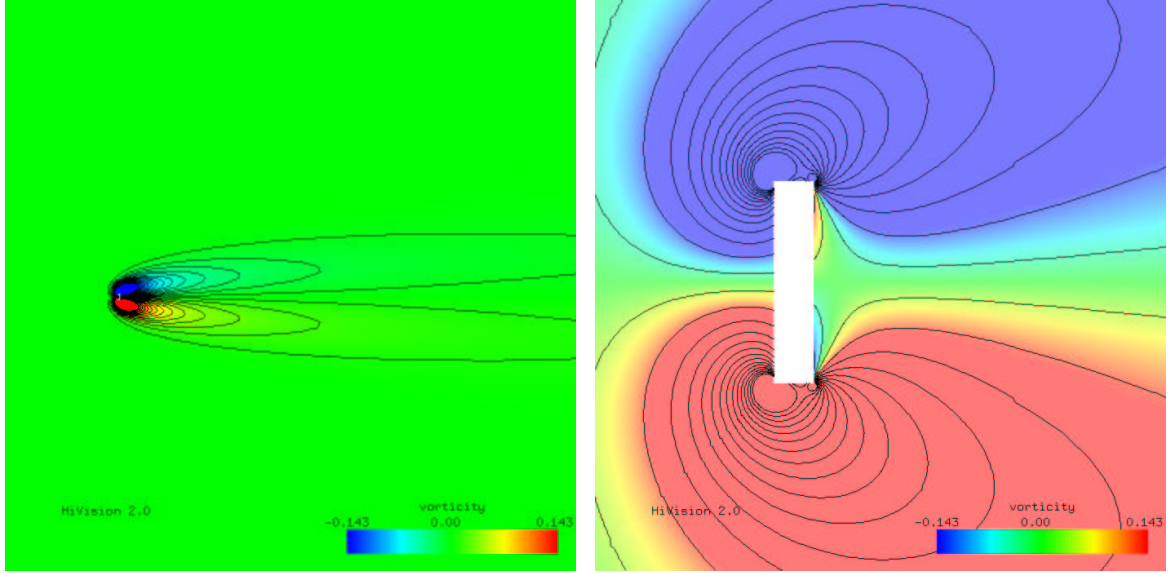This illustrates quite nicely the theorems and arguments of Section 3.2.

Figure 3.9: Vorticity (**left**), zoom on the vorticity (**right**) for the configuration described in the text.
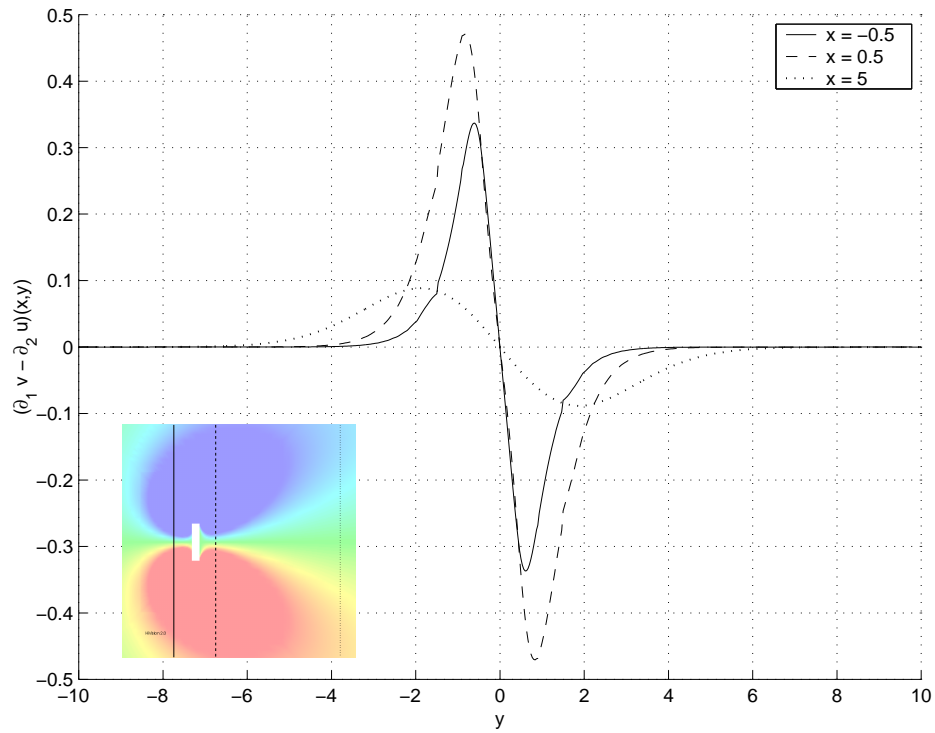

Figure 3.10: Vorticity on vertical lines for $x = -0.5$ (solid line), $x = 0.5$ (dashed line) and $x = 5$ (dotted line), as sketched in the small picture included in the plot.

3.5 Further results

In this chapter we have discussed the problem of solving numerically the stationary incompressible Navier-Stokes equations in a domain exterior to a body in two dimensions. A novel self-consistent scheme for choosing artificial boundary conditions has been introduced which incorporates in particular the computation of the total drag exerted on a body as part of the solution process. When compared with the results obtained using traditional constant boundary conditions computational times are typically reduced by several orders of magnitude.

Although we restricted ourselves to the case of symmetric bodies aligned with the fluid flow, the proposed method is not intrinsically limited to this case. A generalization to the two-dimensional non-symmetric case has been proposed in Bönisch et al. [BHW06] (see also Wittwer/Haldi [WH05]). There, a vector field is constructed in the form of an explicit expression depending on *two real parameters* which can be determined from the *drag and the lift* exerted on the body. Like in the symmetric case, this vector field is used to prescribe artificial boundary conditions on the boundary of the truncated computational domain. The simultaneous determination of the two parameters and the boundary condition is achieved by a self-consistent scheme similar to that discussed above. Another improvement in [BHW06] is the inclusion of higher-order asymptotic terms. Due to the increased accuracy of the resulting artificial boundary conditions the size of the truncated domains (and hence the computational effort) can be further reduced - typically by yet another order of magnitude - as compared with the 'first-order' boundary conditions derived above.

The construction of the 'second-order' adaptive boundary conditions as performed in [BHW06] is quite technical and leads to formulæ of considerable complexity. Therefore, in the following we would like to show only a few of the most important results and refer the interested reader to [BHW06] for all further details.

Figure 3.11 corresponds to Figure 3.4 above: Again, we look at the centerline velocity $v_1(x_1, 0)$ on 'cut I' (see Figure 3.1 for the definition of the cut-lines), and plot the quantity $-2\sqrt{\pi}\sqrt{x_1}v_1(x_1, 0)$ as a function of x_1, where v_1 has been computed once using first-order boundary conditions (the ones discussed in Section 3.2) and once using the improved second-order boundary conditions. With second-order boundary conditions the plot is closer to the asymptotic value on most of the domain. The impact of the second-order terms is however much more evident when considering the gain with regard to the relative error of the drag. In the plots of Figure 3.13 the relative error of the drag as a function of the domain diameter is plotted considering homogeneous Dirichlet boundary conditions, first-order boundary conditions and second-order boundary conditions. Clearly, the addition of the second-order terms allows to again substantially reduce the size of the computational domain when compared to the first-order approach. This is especially true if a high accuracy is needed for the drag. The additional computational time needed for the evaluation of the second-order boundary terms is negligible. Therefore, the reduction of the diameter of the computational domain induced by the second-order terms leads to direct and drastic benefits with regard to the overall computational time.
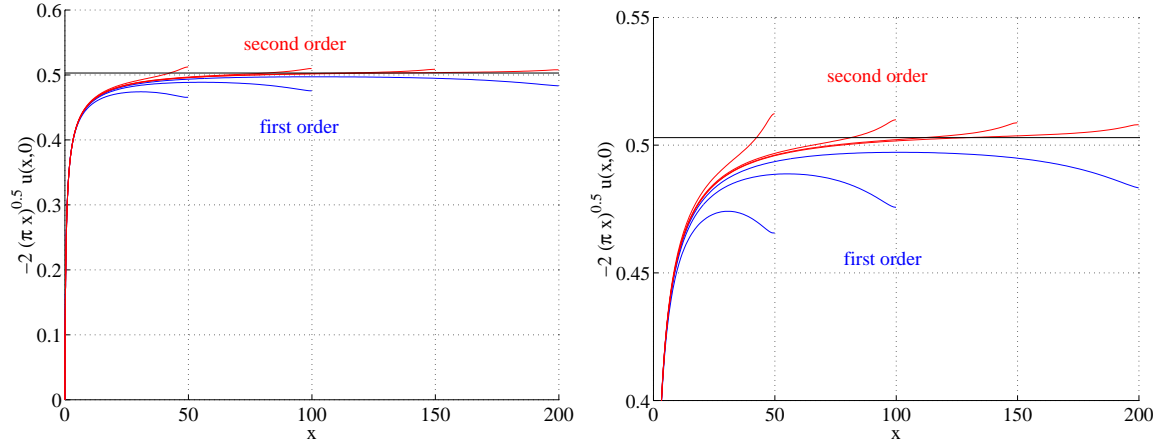
Figure 3.11: The scaled centerline velocity to first and second order (**left**) and zoom on the same quantities (**right**). These plots correspond to Figure 3.4, above.
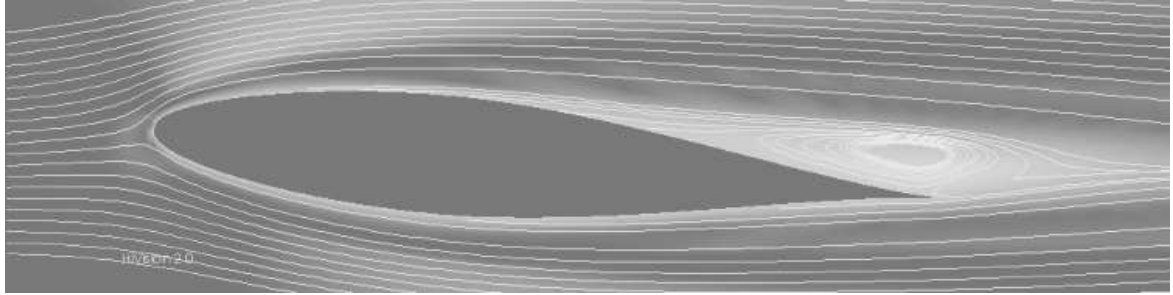

Figure 3.12: Flow around the NACA profile 64-015 at Reynolds number $Re = 1000$, computed using second-order adaptive boundary conditions.

Finally, Figure 3.12 shows the flow around the NACA profile 64-915, inclined by 5°, at Reynolds number $Re = 1000$ (see (3.2.1)), with A the chord length of the profile (distance from tip to tail), see Ladson et al. [LBH$^+$96]. Using our second-order artificial boundary conditions, it was possible to carry out this simulation on a very small computational domain. The (qualitative) comparison with the flow pattern obtained in a corresponding experiment is very satisfying and can be found in [BHW06].
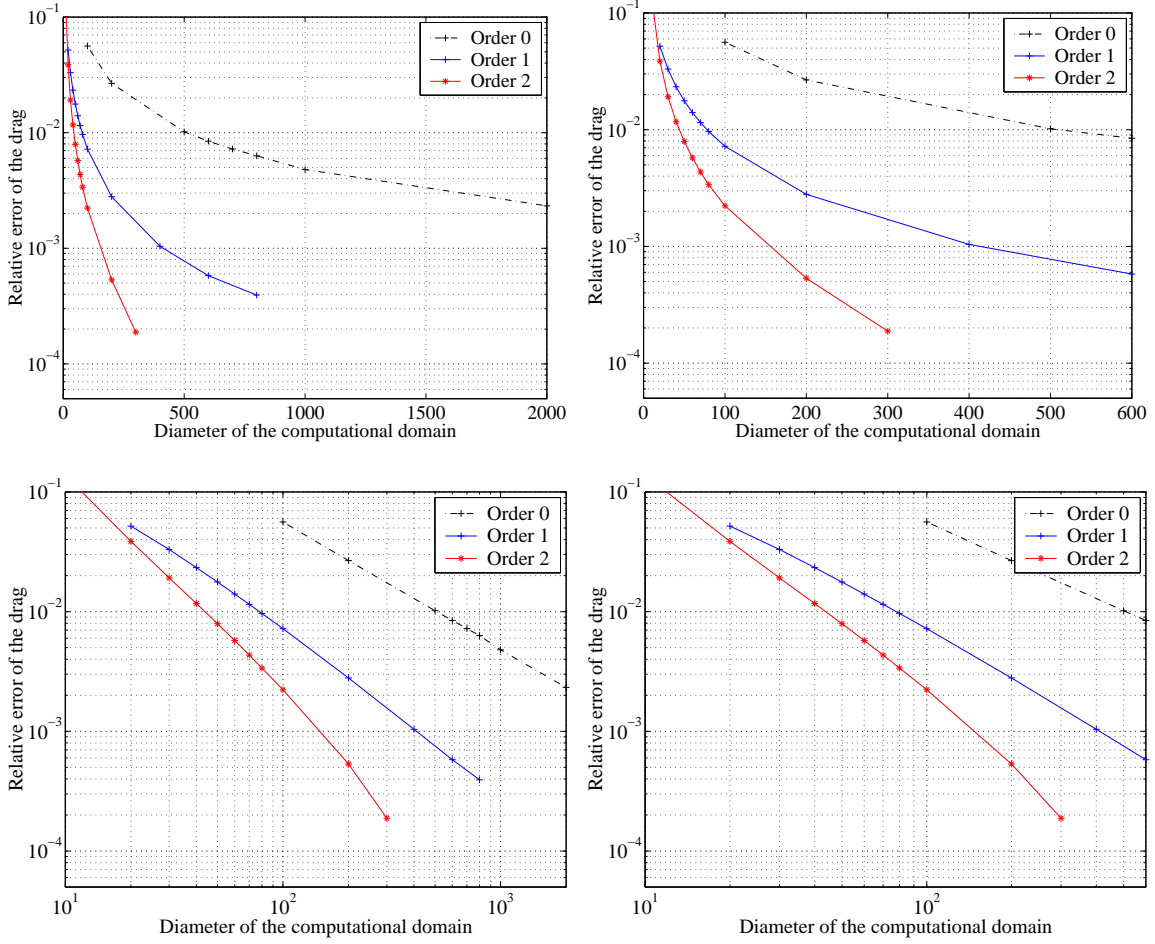
Figure 3.13: Plot of the relative error of the drag as a function of the domain diameter considering homogeneous Dirichlet boundary conditions and the adaptive boundary conditions to first and second order. From left to right and top to bottom the quantities are plotted in semi-log plots un-zoomed and zoomed and in log/log plots un-zoomed and zoomed.

4 Sedimentation of a single particle in a channel flow: Galdi's method

In the previous two chapters we considered, as a model problem, a single rigid body moving in a *viscous, Newtonian* fluid filling *the whole space.* The objective of this chapter is to describe some recent contributions to a problem which is considerably more complex, namely we treat the motion of a single symmetric particle in a *viscoelastic* fluid bounded by *two parallel walls.* More specifically, we consider a cylinder which is moving under the action of gravity in a vertical channel through a Poiseuille flow which may be directed either in the same or in opposite direction of the gravitational force. Furthermore, the viscoelastic liquid is taken to be a so-called 'second-order' liquid model, see e.g. Joseph [Jos90]. However, the method we are going to employ is also applicable to several other situations (e.g. horizontal channel flow, different liquid model, different particle geometry). Our main goal is to find 'steady' solutions to the fluid-particle system and to determine all possible equilibrium positions of the cylinder with respect to the walls.

This chapter is organized as follows: In order to better describe our methods and results, in Section 4.1 we give the main motivation behind the considered problem, as well as a short review of the relevant literature. In Section 4.2 we present a method to investigate the equilibrium positions of the sedimenting cylinder; this method is due to Galdi, see Galdi/Heuveline [GH06] and Bönisch/Galdi [BG06]. We derive a system of equations from which we can extract information about possible equilibria, *at first order in Re and We*, where Re is a suitable Reynolds number and We is the Weissenberg number. In the case of a purely Newtonian liquid, we can get more precise information by evaluating the equilibrium equations *at third order in Re*. The method relies on the evaluation of certain integrals which depend on the solutions of a number of auxiliary problems of Stokes-type. This can only be done numerically; the details of the numerical solution process are described in Section 4.3. Section 4.4 contains a number of numerical results.[1] The findings are discussed and compared to experimental observations.

4.1 Introduction

The study of a sedimenting cylinder in an infinite channel filled with liquid, possibly in the presence of a Poiseuille flow, concerns some of the fundamental aspects of particle sedimen-

---

tation in the presence of walls, see e.g. [GH06, BG06]. Understanding the motion of particles settling near walls in a liquid is of fundamental theoretical interest. Moreover, it is also a key issue in many industrial processes involving particle-laden materials, see e.g. Chhabra [Chh93]. Important examples include falling-ball viscometry, flow of slurries and coating processes for thin films (see e.g. Joseph [Jos00] and Ruschak [Rus85]). Let us consider first the case of a stagnant fluid (i.e. no Poiseuille flow). The following is known from experiments (cf. Joseph [Jos00]). When a homogeneous sphere sediments near a rigid wall, its terminal state depends on the physical properties of the fluid: If the liquid is Newtonian and viscous enough, the sphere will *move away* from the wall and reach a steady state characterized by the parameters U (translational velocity), ω (angular velocity) and h_{equi} (distance from the wall). However, for a viscoelastic liquid the same sphere will *move towards* the wall! Theoretical studies on the motion of spheres in presence of walls, under different flow conditions, have been the object of many papers; see, e.g., Becker et al. [BKS96], Cox/Brenner [CB68], Vasseur/Cox [VC76, VC77], Ho/Leal [HL74, HL76] and references cited therein.

These studies represent a significant attempt towards an understanding of the impact of the walls on a sedimenting sphere. However, most of the theoretical contributions are partially incomplete, for the following reasons: Firstly, all of them *prescribe* either the (translational and angular) velocity of the sphere (see e.g. Vasseur/Cox [VC76]) or the distance of the sphere from the wall (see e.g. Becker et al. [BKS96]). Consequently, they are only focused on certain aspects of the physical phenomena, like the evaluation of the lateral lift force on the sphere or its terminal velocity. Secondly, in the case of a viscoelastic fluid, they are obtained by assuming that there is *only one* wall (see Becker et al. [BKS96]). A third limitation is that they are all based on *formal* (matched) asymptotic expansions of the velocity and pressure fields (like 'inner-outer expansions') that lack a rigorous mathematical justification.

The motion of rigid spherical particles suspended in a Newtonian viscous liquid flowing under steady laminar conditions in a vertical tube or channel has been investigated in, e.g., Jeffrey/Pearson [JP65] and Asmolov [Asm99], see also Eichhorn/Small [ES64] and references cited therein.
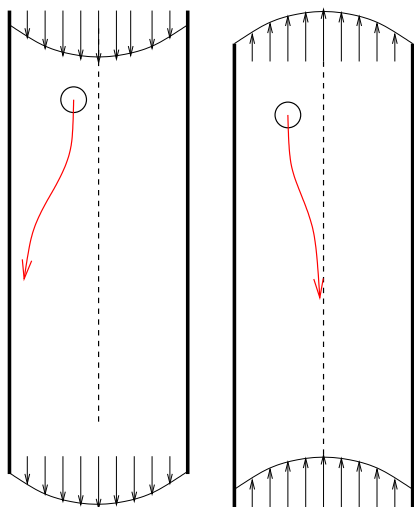
At small Reynolds number they found (see picture on the left) that particles that are slightly denser that the fluid migrate *towards the wall* for downward fluid flow and to the *axis of the tube* for upward fluid flow. Consequently, in the case of upward flow it should be possible to bring the particle to rest in the middle of the channel or tube by adjusting the flow rate. In fact, this procedure is described in Eichhorn/Small [ES64]: In this experimental paper the authors describe how they introduce a particle in a vertical tube filled with fluid and adjust the Poiseuille flow in such a way that the particle comes to rest.

In this chapter we shall address the aforementioned issues and present results which are valid for small enough (channel) Reynolds number Re and Weissenberg number We. In particular, we improve upon the weak points of some of the papers mentioned above. The strategy we are going to adopt to reach this goal is the following, see Galdi/Heuveline [GH06] and Bönisch/Galdi [BG06]: We first *fix* the distance h of the center of the sphere from one of the walls and ask for a solution $\{v, p, U, \omega\}$ of the corresponding steady system sphere-liquid. Due to the fact that we keep h fixed, the translational velocity U of the sphere need not be directed parallel to the wall of the channel and may have, in principle, a non-zero component U_2, perpendicular to the wall. By using the Lorentz reciprocal theorem (see e.g. Pozrikidis [Poz97]) we show that $U_2 = F(v, \mathrm{Re}, \mathrm{We}, \mathrm{Fr}, h, \alpha)$, where F is an appropriate function of the velocity field v, of the Reynolds, Weissenberg and Froude numbers Re, We, Fr, of h and of the buoyancy α. The equilibrium position $h = h_{equi}$ will be the one that makes $F = 0$. Using a theorem by Galdi, we expand the unknown solution $\{v, p, U, \omega\}$ around the solution $\{v_s, p_s, U_s, \omega_s\}$ corresponding to Re = We = 0 (Stokes approximation) and show that

$$U_2 = \mathrm{Re}\,(1 + E)U_2^{(1)} + \mathcal{O}(\mathrm{Re}^2 + \mathrm{We}^2),$$

and that

$$F = \mathrm{Re}\,\frac{\mathrm{Fr}^2}{\mathcal{T}_2(h)}[\mathcal{G}(h; \overline{\alpha}) + E\mathcal{G}_V(h; \overline{\alpha})] + \mathcal{O}(\mathrm{Re}^2 + \mathrm{We}^2).$$

Here, $\mathcal{T}_2(h) > 0$ is a function of h only, while $\mathcal{G}(h; \overline{\alpha})$ and $\mathcal{G}_V(h; \overline{\alpha})$ are functions of h and $\overline{\alpha} := \alpha/\mathrm{Fr}$, and $E = \frac{\mathrm{We}}{\mathrm{Re}}$ is the elasticity number. Therefore, *at first order in Re and We*, we have

$$U_2^{(1)} = \frac{\mathrm{Fr}^2}{(1 + E)\mathcal{T}_2(h)}[\mathcal{G}(h; \overline{\alpha}) + E\mathcal{G}_V(h; \overline{\alpha})].$$

The equilibrium position h_{equi} is obtained by imposing $U_2^{(1)} = 0$, and it is found to be a function of $\overline{\alpha}$ and E. The study of possible equilibrium positions and their stability is performed in Section 4.4. In the case of a purely Newtonian liquid (We = 0), we can obtain further results by expanding all quantities around the Stokes solution up to *third order in Re*.

4.2 Determination of equilibrium positions

The exposition in this section follows closely the lines of the papers Galdi/Heuveline [GH06] and Bönisch/Galdi [BG06].

4.2.1 Problem formulation and analytical preliminaries

We want to investigate equilibrium positions of a cylinder (disk in 2D) sedimenting through a vertical channel Poiseuille flow, see Figure 4.1. We are only interested in *steady motions* of the system liquid-disk. Here, the 'steadiness' has to be understood in the following sense: We introduce a coordinate frame attached to the disk center and moving with velocity U and require that the motion of the fluid as seen from this body frame is independent of
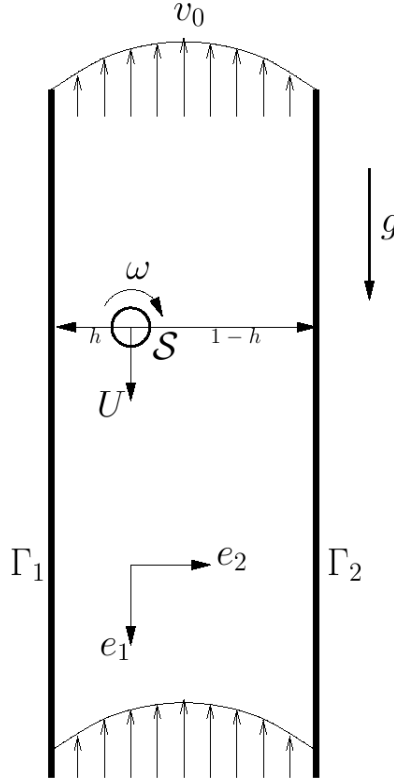
Figure 4.1: Description of the flow problem.

time. Moreover, the translational (angular, resp.) velocity U (ω, resp.) of the disk has to be constant in time, too. It is clear that such a steady motion can only occur if the (unknown) velocity U of the disk is directed along the channel walls which we will assume to be parallel to the x_1-axis of the body frame. We also assume, without loss of generality, that the origin of the body frame coincides with the disk center. We take d as a measure of the thickness of the channel. It is convenient to define as scaling velocity $V = \sqrt{gd}$, with g acceleration of gravity.

With these notations we find that the Poiseuille flow (v_0, p_0), as seen from the body frame assumes the following dimensionless form:

$$v_0(x_2; h) = -6 \operatorname{sgn}(\Phi) \operatorname{Fr} [h^2 + h(2x_2 - 1) + x_2(x_2 - 1)] e_1 \equiv \operatorname{Fr} f(x_2, h) e_1,$$

$$p_0 = -12 \frac{\Phi}{\mu d^2} x_1, \tag{4.2.1}$$

where $\operatorname{Fr} := \frac{|\Phi|}{Vd}$ is the Froude number, Φ is the given flow rate[2], μ is the shear viscosity and $-h$ (resp. $1 - h$) is the x_2-coordinate of the wall Γ_1 (resp. Γ_2) of the channel (see Figure 4.1). The channel flow problem we are interested in can then be formulated as follows.

---

[2] We shall use the following convention: If the fluid is flowing in the positive (negative, resp.) x_1-direction, we assume $\Phi > 0$ ($\Phi < 0$, resp.).

Find $\{v, P, U, \omega, h\}$ satisfying the dimensionless equations:

$$\begin{cases} \nabla \cdot \sigma(v, P) = \mathrm{Re}\,(v \cdot \nabla)v, \\ \nabla \cdot v = 0, \end{cases} \quad \text{in } \Omega,$$

$$v_{|\partial\mathcal{S}} = \omega e_3 \times x, \quad v_{|\Gamma_1} = v_{|\Gamma_2} = -U,$$

$$\lim_{|x_1|\to\infty} (v(x_1, x_2) - v_0(x_2; h) + U) = 0,$$

$$\int_{-h}^{1-h} v_1(x_1, x_2)\, dx_2 = \mathrm{sgn}(\Phi)\, \mathrm{Fr} - U \cdot e_1,$$

(4.2.2)

$$\int_{\partial\mathcal{S}} \sigma(v, P) \cdot n = G, \quad \int_{\partial\mathcal{S}} x \times [\sigma(v, P) \cdot n] = 0.$$

Here, Ω is the region occupied by the fluid and $\sigma = \sigma(v, P)$ is the Cauchy stress tensor. We assume a 'second-order' liquid model, see e.g. Joseph [Jos90]. In such a case, σ is given by

$$\sigma(v, P) = \sigma_N(v, P) - \mathrm{We}\, S(v),$$

(4.2.3)

where

$$\sigma_N(v, P) = -PI + 2D(v), \quad D = D(v) := (L + L^T)/2, \quad L = L(v) := \nabla v,$$
$$S(v) = 2(v \cdot \nabla)D + 2D \cdot L^T + 2L \cdot D + 4\varepsilon D \cdot D.$$

(4.2.4)

Moreover, $P = p - x_1$ is the modified pressure, $\mathrm{Re} := \frac{\rho V d}{\mu}$ is the (channel) Reynolds number, ρ is the fluid density, $\mathrm{We} := \frac{-\alpha_1 V}{d\mu}$ is the Weissenberg number, $\varepsilon := \alpha_2/\alpha_1$ where $\alpha_1 < 0$ and α_2 are the so-called 'quadratic constants'. In accordance with classical experimental results on viscoelastic liquids (see e.g. Liu/Joseph [LJ93]) we have fixed the constant ε to be -1.8. Furthermore, $\alpha := \pi(R/d)^2(\rho_s/\rho - 1)$ where R, ρ_s are the radius and the density of the disk, respectively, and $G = \alpha e_1$.

The first important step is to prove the existence and uniqueness of a solution to problem (4.2.2) for any *given* $h \in (a, 1 - a)$, where $a := R/d < 1/2$. In the following formulation of the main analytical result we denote by $(W^{m,q}(\Omega), \|\cdot\|_{m,q}), m \geq 0, q \geq 1$ the usual Sobolev space of functions in Ω having all derivatives up to the order m inclusive that are summable to the q-th power.

Theorem 4.1. Let $h \in (a, 1 - a)$ be given and let $\mathrm{Fr} \geq 0, \alpha \geq 0$. Then, there exists $\mathrm{Re}_0 > 0$ and $\mathrm{We}_0 > 0$ such that if $\mathrm{Re} < \mathrm{Re}_0$ and $\mathrm{We} < \mathrm{We}_0$ problem (4.2.2) admits one and only one solution $\{v, P, U, \omega\}$ such that

$$(v - v_0 + U) \in W^{2,2}(\Omega), \quad (P - p_0) \in W^{1,2}(\Omega).$$

Moreover, let $\{v_s, P_s, U_s, \omega_s\}$ be the solution of (4.2.2) corresponding to $\mathrm{Re} = \mathrm{We} = 0$. Then

$$v = v_s + (\mathrm{Re} + \mathrm{We})v^{(1)} + (\mathrm{Re}^2 + \mathrm{We}^2)v^{(2)}, \quad P = P_s + (\mathrm{Re} + \mathrm{We})P^{(1)} + (\mathrm{Re}^2 + \mathrm{We}^2)P^{(2)},$$

$$U = U_s + (\mathrm{Re} + \mathrm{We})U^{(1)} + (\mathrm{Re}^2 + \mathrm{We}^2)U^{(2)}, \quad \omega = \omega_s + (\mathrm{Re} + \mathrm{We})\omega^{(1)} + (\mathrm{Re}^2 + \mathrm{We}^2)\omega^{(2)},$$

$$\sum_{i=1}^{2} \left(|U^{(i)}| + |\omega^{(i)}| + \|\nabla v^{(i)}\|_{1,2} + \|P^{(i)}\|_{1,2} \right) \leq C,$$

(4.2.5)

with C depending only on Ω, Fr, Re_0 and We_0. Finally, if $\mathrm{We} = 0$ (purely Newtonian liquid), then v, p, U and ω are real-analytic in Re and their series are absolutely convergent in $W^{2,2}(\Omega)$, $W^{1,2}(\Omega)$, $\mathbb{R}^2$ and $\mathbb{R}$, respectively.

This theorem which is due to Galdi can be proved by following exactly the methods used in Galdi et al. [GVP$^+$02], see also Galdi/Heuveline [GH06].

Remark 4.2. The translational velocity U of the solutions given in Theorem 4.1 need *not* be directed along the walls Γ_1, Γ_2, that is, these solutions may have $U_2 \neq 0$. The objective of the next section is therefore to find conditions under which $U_2 = 0$. Such conditions will give precisely the possible values for h.

4.2.2 Derivation of the equilibrium equations

Our goal is to rewrite the last two equations in (4.2.2) in such a way that we get explicit expressions for the body variables U and ω as functions of the velocity field v. To this end, we introduce *auxiliary fields* $\{w^{(i)}, \pi^{(i)}\}$ defined as solutions of the following linear Stokes problems ($i = 1, 2, 3$):

$$
\begin{cases}
\begin{aligned}
\nabla \cdot \sigma_N(w^{(i)}, \pi^{(i)}) &= 0, \\
\nabla \cdot w^{(i)} &= 0,
\end{aligned} & \quad \text{in } \Omega,
\end{cases}
$$
$$
w^{(i)}_{|\partial \mathcal{S}} = \beta_i, \quad w^{(i)}_{|\Gamma_1} = w^{(i)}_{|\Gamma_2} = 0,
$$
$$
\lim_{|x_1| \to \infty} w^{(i)}(x_1, x_2) = 0,
$$

$$\tag{4.2.6}$$

where $\beta_i = e_i$ for $i = 1, 2$, and $\beta_3 = e_3 \times x$. Notice that all fields $w^{(i)}, \pi^{(i)}$ depend only on h.

Remark 4.3. The field $w^{(1)}$ ($w^{(2)}$, resp.) corresponds to the motion of a disk translating at unit velocity parallel (perpendicular, resp.) to the wall, while $w^{(3)}$ represents the rotation of the disk with unit angular velocity. The idea in the following is to relate the unknown solution v to the Stokes fields $w^{(i)}$, $i = 1, 2, 3$, by exploiting the mutual structure of velocity and stress of two different flow fields ('Lorentz reciprocal theorem'). The special choice for the boundary conditions of the auxiliary problems (4.2.6) will lead to three scalar equations for the three unknown body variables U_1, U_2 and ω, see equation (4.2.16).

In view of the symmetry $x_1 \leftrightarrow -x_1$ of problems (4.2.6), it can be easily shown that the following relations hold:

$$
\int_{\partial \mathcal{S}} \sigma_N(w^{(2)}, \pi^{(2)}) \cdot n = \mathcal{T}_2(h)e_2, \quad \int_{\partial \mathcal{S}} x \times [\sigma_N(w^{(2)}, \pi^{(2)}) \cdot n] = 0,
$$
$$
\int_{\partial \mathcal{S}} \sigma_N(w^{(3)}, \pi^{(3)}) \cdot n = \mathcal{T}_3(h)e_1, \quad \int_{\partial \mathcal{S}} \sigma_N(w^{(1)}, \pi^{(1)}) \cdot n = \mathcal{T}_1(h)e_1,
$$
$$
\int_{\partial \mathcal{S}} v_0 \cdot \sigma_N(w^{(1)}, \pi^{(1)}) \cdot n = \mathrm{Fr}\, \mathcal{F}_1(h), \quad \int_{\partial \mathcal{S}} v_0 \cdot \sigma_N(w^{(2)}, \pi^{(2)}) \cdot n = 0,
$$
$$
\int_{\partial \mathcal{S}} v_0 \cdot \sigma_N(w^{(3)}, \pi^{(3)}) \cdot n = \mathrm{Fr}\, \mathcal{F}_3(h),
$$

$$\tag{4.2.7}$$

where $\mathcal{T}_i(h), i = 1, 2, 3$, and $\mathcal{F}_i(h), i = 1, 2, 3$, depend only on h. Moreover,

$$\int_{\partial \mathcal{S}} x \times [\sigma_N(w^{(1)}, \pi^{(1)}) \cdot n] = \mathcal{R}_1(h)e_3, \quad \int_{\partial \mathcal{S}} x \times [\sigma_N(w^{(3)}, \pi^{(3)}) \cdot n] = \mathcal{R}_3(h)e_3, \quad (4.2.8)$$

where, again, $\mathcal{R}_i(h), i = 1, 3$, depend only on h.

Later on, we will need the following technical lemma:

Lemma 4.4. The following inequalities hold for all $h \in (a, 1 - a)$:

$$\mathcal{T}_1(h) > 0, \quad \mathcal{T}_2(h) > 0, \quad \mathcal{R}_3(h) > 0, \\ \mathcal{T}_1(h)\mathcal{R}_3(h) - \mathcal{R}_1(h)\mathcal{T}_3(h) > 0. \tag{4.2.9}$$

Proof. First, we show that

$$\mathcal{T}_3(h) = \mathcal{R}_1(h), \quad \forall h \in (a, 1 - a). \tag{4.2.10}$$

To this end, we multiply the first equation in (4.2.6) with $i = 3$ by $w^{(1)}$ and integrate by parts. Taking into account (4.2.7), we obtain

$$\mathcal{T}_3(h) = 2 \int_{\Omega} D(w^{(1)}) : D(w^{(3)}). \tag{4.2.11}$$

Likewise, if we multiply the first equation in (4.2.6) with $i = 1$ by $w^{(3)}$, integrate by parts and take into account (4.2.7), we obtain

$$\mathcal{R}_1(h) = 2 \int_{\Omega} D(w^{(3)}) : D(w^{(1)}), \tag{4.2.12}$$

and (4.2.10) follows.

Now we prove (4.2.9). To this end, we define $w := \sum_{i=1}^{3} \lambda_i w^{(i)}$, $\Pi := \sum_{i=1}^{3} \lambda_i \pi^{(i)}$ for arbitrary $\lambda_i \in \mathbb{R}$, $i = 1, 2, 3$. From (4.2.6) we find

$$\begin{cases} \nabla \cdot \sigma_N(w, \Pi) = 0, \\ \nabla \cdot w = 0, \end{cases} \quad \text{in } \Omega,$$
$$w_{|\partial \mathcal{S}} = \sum_{i=1}^{3} \lambda_i \beta_i, \quad w_{|\Gamma_1} = w_{|\Gamma_2} = 0, \tag{4.2.13}$$
$$\lim_{|x_1| \to \infty} w(x_1, x_2) = 0.$$

Multiplying the first equation in (4.2.13) by w, integrating by parts over Ω and taking into account (4.2.7) and (4.2.10) we get

$$\lambda_1^2 \mathcal{T}_1 + \lambda_2^2 \mathcal{T}_2 + \lambda_3^2 \mathcal{R}_3 + 2\lambda_1 \lambda_3 \mathcal{T}_3 = 2 \int_{\Omega} |D(w)|^2.$$

Since the right-hand side of this equation is always positive, unless $\lambda_1 = \lambda_2 = \lambda_3 = 0$, and the λ_i, $i = 1, 2, 3$ are arbitrary, (4.2.9) follows and the lemma is proved. $\square$

We now multiply the first equation in (4.2.2) by $w^{(i)}$, integrate by parts over Ω and use the asymptotic properties of $w^{(i)}$ to obtain ($i = 1, 2, 3$)

$$\int_{\partial S} \beta_i \cdot \sigma(v, P) \cdot n = \text{Re} \int_{\Omega} ((v \cdot \nabla)v) \cdot w^{(i)} - \text{We} \int_{\Omega} S(v) : D(w^{(i)}) + 2 \int_{\Omega} D(v) : D(w^{(i)}). \quad (4.2.14)$$

Likewise, if we multiply the first equation in (4.2.6) by $v - v_0 + U$ and integrate by parts over Ω, we find ($i = 1, 2, 3$)

$$\int_{\partial S} (U + \omega e_3 \times x - v_0) \cdot \sigma_N(w^{(i)}, \pi^{(i)}) \cdot n = 2 \int_{\Omega} D(v) : D(w^{(i)}). \quad (4.2.15)$$

From (4.2.7),(4.2.8),(4.2.14),(4.2.15), one deduces that the last two equations in (4.2.2) are equivalent to the following ones:

$$\omega \mathcal{R}_1(h) + U_1 \mathcal{T}_1(h) = \text{Fr}\, \mathcal{F}_1(h) + G_1 - \text{Re} \int_{\Omega} ((v \cdot \nabla)v) \cdot w^{(1)} + \text{We} \int_{\Omega} S(v) : D(w^{(1)}),$$

$$U_2 \mathcal{T}_2(h) = -\text{Re} \int_{\Omega} ((v \cdot \nabla)v) \cdot w^{(2)} + \text{We} \int_{\Omega} S(v) : D(w^{(2)}),$$

$$\omega \mathcal{R}_3(h) + U_1 \mathcal{T}_3(h) = \text{Fr}\, \mathcal{F}_3(h) - \text{Re} \int_{\Omega} ((v \cdot \nabla)v) \cdot w^{(3)} + \text{We} \int_{\Omega} S(v) : D(w^{(3)}).$$

$$(4.2.16)$$

Remark 4.5. Equation (4.2.16) represent a linear system for the body variables $\{U_1, U_2, \omega\}$ which is uniquely solvable for any right-hand side in virtue of (4.2.9). The right-hand side still depends on the unknown solution v. In the following we will plug the asymptotic expansion (4.2.5) into formula (4.2.16) and obtain information about the solutions of the particle-liquid system at first order in Re and We, as well as at first, second and third order in Re.

4.2.3 Evaluation of the equilibrium equations

The Stokes approximation

We start by evaluating equation (4.2.16) at 'zero-th order' in Re and We, in other words: we determine the solution $\{v_s, U_s, \omega_s\}$ of the particle-liquid system[3] for the case $\text{Re} = \text{We} = 0$. Recalling that $\mathcal{T}_2(h) > 0$, we get from the second equation in (4.2.16) that $U_{s2} = 0$. The first and third equation in (4.2.16) determine U_{s1} and ω_s:

$$\begin{aligned}
\omega_s \mathcal{R}_1(h) + U_{s1} \mathcal{T}_1(h) &= \text{Fr}\, \mathcal{F}_1(h) + \alpha, \\
\omega_s \mathcal{R}_3(h) + U_{s1} \mathcal{T}_3(h) &= \text{Fr}\, \mathcal{F}_3(h).
\end{aligned} \quad (4.2.17)$$

Set

$$\overline{v}_s \equiv v_s/\text{Fr}, \quad \overline{\omega}_s \equiv \omega_s/\text{Fr}, \quad \overline{U}_{s1} \equiv U_{s1}/\text{Fr}, \quad \overline{\alpha} \equiv \alpha/\text{Fr}. \quad (4.2.18)$$

---

[3] The subscript 's' stands for 'Stokes'. The pressure P_s is not needed in the following.

Then (4.2.17) becomes

$$\overline{\omega}_s \mathcal{R}_1(h) + \overline{U}_{s1}\mathcal{T}_1(h) = \mathcal{F}_1(h) + \overline{\alpha},$$
$$\overline{\omega}_s \mathcal{R}_3(h) + \overline{U}_{s1}\mathcal{T}_3(h) = \mathcal{F}_3(h). \tag{4.2.19}$$

In view of (4.2.9), system (4.2.19) has one and only one solution that depends only on h. The Stokes field $\overline{v}_s$ then can be written as $\overline{v}_s = \overline{U}_{s1}(w^{(1)} - e_1) + \overline{\omega}_s w^{(3)} + w^{(4)}$, where $w^{(i)}, i = 1, 3$ denote the auxiliary fields introduced in (4.2.6), and $\{w^{(4)}, \pi^{(4)}\}$ is defined as the solution of the following problem:

$$\begin{cases} \nabla \cdot \sigma_N(w^{(4)}, \pi^{(4)}) = 0, \\ \nabla \cdot w^{(4)} = 0, \end{cases} \quad \text{in } \Omega,$$
$$w^{(4)}_{|\partial \mathcal{S}} = 0, \quad w^{(4)}_{|\Gamma_1} = w^{(4)}_{|\Gamma_2} = 0, \tag{4.2.20}$$
$$\lim_{|x_1| \to \infty} (w^{(4)}(x_1, x_2) - f(x_2; h)e_1) = 0.$$

Evaluation at first order in Re and We

To evaluate equation (4.2.16) at first order in Re and We, we write (see (4.2.5)):

$$v = v_s + (\text{Re} + \text{We})v^{(1)} + (\text{Re}^2 + \text{We}^2)v^{(2)},$$
$$U = U_s + (\text{Re} + \text{We})U^{(1)} + (\text{Re}^2 + \text{We}^2)U^{(2)}, \tag{4.2.21}$$
$$\omega = \omega_s + (\text{Re} + \text{We})\omega^{(1)} + (\text{Re}^2 + \text{We}^2)\omega^{(2)},$$

and employ the second equation in (4.2.16) to obtain (recall that $U_{s2} = 0$)

$$(\text{Re} + \text{We})U_2^{(1)}\mathcal{T}_2(h) = \text{Fr}^2\text{Re}\,\mathcal{G}(h; \overline{\alpha}) + \text{Fr}^2\text{We}\,\mathcal{G}_V(h; \overline{\alpha}) + \Lambda, \tag{4.2.22}$$

where

$$\mathcal{G}(h; \overline{\alpha}) := -\int_\Omega ((\overline{v}_s \cdot \nabla)\overline{v}_s) \cdot w^{(2)}, \quad \mathcal{G}_V(h; \overline{\alpha}) := \int_\Omega S(\overline{v}_s) : D(w^{(2)}), \tag{4.2.23}$$

and

$$|\Lambda| \leq C(\text{Re} + \text{We})^2, \quad C = C(\Omega, \text{Fr}) > 0. \tag{4.2.24}$$

Thus, at first order in Re and We, it follows that $U_2^{(1)}$ is given by

$$U_2^{(1)} = \frac{\text{Fr}^2}{(1+E)\mathcal{T}_2(h)}[\mathcal{G}(h; \overline{\alpha}) + E\mathcal{G}_V(h; \overline{\alpha})], \tag{4.2.25}$$

with the elasticity number $E := \text{We}/\text{Re}$.

Since the equilibrium positions h_{equi} are those at which $U_2 = 0$, from (4.2.25) we deduce that, at first order in Re and We, h_{equi} is the solution to the equation

$$\mathcal{G}(h; \overline{\alpha}) + E\mathcal{G}_V(h; \overline{\alpha}) = 0. \tag{4.2.26}$$

Solutions of equation (4.2.26) will be computed numerically and discussed in Section 4.4. The first-order contributions to U_1 and ω can be computed in a similar manner from the first and third equation in (4.2.16):

$$\omega^{(1)}\mathcal{R}_1(h) + U_1^{(1)}\mathcal{T}_1(h) = \frac{\mathrm{Fr}^2}{(1+E)}\left[-\int_{\Omega}((\overline{v}_s\cdot\nabla)\overline{v}_s)\cdot w^{(1)} + E\int_{\Omega}S(\overline{v}_s):D(w^{(1)}) \right],$$

$$\omega^{(1)}\mathcal{R}_3(h) + U_1^{(1)}\mathcal{T}_3(h) = \frac{\mathrm{Fr}^2}{(1+E)}\left[-\int_{\Omega}((\overline{v}_s\cdot\nabla)\overline{v}_s)\cdot w^{(3)} + E\int_{\Omega}S(\overline{v}_s):D(w^{(3)}) \right].$$

$$(4.2.27)$$

Interestingly, we found that the integrals appearing on the right hand side of (4.2.27) are effectively zero, from a numerical point of view. In other words, there is no correction at first order of the quantities U_1 and ω with respect to their Stokes approximations U_{s1} and ω_s (see also Remark 4.7).

Evaluation at third order in Re

For a purely Newtonian liquid (We = 0) we know from Theorem 4.1 that v, p, U and ω are real-analytic functions in Re. In such a case we can extend the results above and evaluate equation (4.2.16) at any arbitrary order. In the following we perform this expansion up to third order.

We write

$$v = v_s + \mathrm{Re}\,v^{(1)} + \mathrm{Re}^2 v^{(2)} + \mathcal{O}(\mathrm{Re}^3),$$
$$P = P_s + \mathrm{Re}\,P^{(1)} + \mathrm{Re}^2 P^{(2)} + \mathcal{O}(\mathrm{Re}^3),$$
$$U = U_s + \mathrm{Re}\,U^{(1)} + \mathrm{Re}^2 U^{(2)} + \mathrm{Re}^3 U^{(3)} + \mathcal{O}(\mathrm{Re}^4),$$
$$\omega = \omega_s + \mathrm{Re}\,\omega^{(1)} + \mathrm{Re}^2\omega^{(2)} + \mathrm{Re}^3\omega^{(3)} + \mathcal{O}(\mathrm{Re}^4)\,.$$

$$(4.2.28)$$

Exploiting (4.2.16) and repeating the argument used above with $E = 0$ we find that the first-order contributions to U_1, U_2, ω are the solutions of the following linear system:

$$\omega^{(1)}\mathcal{R}_1(h) + U_1^{(1)}\mathcal{T}_1(h) = -\mathrm{Fr}^2\int_{\Omega}((\overline{v}_s\cdot\nabla)\overline{v}_s)\cdot w^{(1)},$$

$$U_2^{(1)} = -\frac{\mathrm{Fr}^2}{\mathcal{T}_2(h)}\int_{\Omega}((\overline{v}_s\cdot\nabla)\overline{v}_s)\cdot w^{(2)},$$

$$\omega^{(1)}\mathcal{R}_3(h) + U_1^{(1)}\mathcal{T}_3(h) = -\mathrm{Fr}^2\int_{\Omega}((\overline{v}_s\cdot\nabla)\overline{v}_s)\cdot w^{(3)}.$$

$$(4.2.29)$$

We next determine $v^{(1)}$ in (4.2.28). Recall that (v, P) and (v_s, P_s) are solutions to the following two problems:

$$\begin{cases} \nabla \cdot \sigma_N(v, P) = \text{Re}\,(v \cdot \nabla)v, \\ \nabla \cdot v = 0, \end{cases} \quad \text{in } \Omega,$$
$$v_{|\partial \mathcal{S}} = \omega e_3 \times x, \quad v_{|\Gamma_1} = v_{|\Gamma_2} = -U,$$
$$\lim_{|x_1| \to \infty} (v(x_1, x_2) - v_0(x_2; h) + U) = 0,$$

and

$$\begin{cases} \nabla \cdot \sigma_N(v_s, P_s) = 0, \\ \nabla \cdot v_s = 0, \end{cases} \quad \text{in } \Omega,$$
$$v_{s|\partial \mathcal{S}} = \omega_s e_3 \times x, \quad v_{s|\Gamma_1} = v_{s|\Gamma_2} = -U_s,$$
$$\lim_{|x_1| \to \infty} (v_s(x_1, x_2) - v_0(x_2; h) + U_s) = 0.$$

The difference $(v - v_s, P - P_s)$ is therefore a solution to the problem

$$\begin{cases} \nabla \cdot \sigma_N(v - v_s, P - P_s) = \text{Re}\,(v \cdot \nabla)v, \\ \nabla \cdot (v - v_s) = 0, \end{cases} \quad \text{in } \Omega,$$
$$(v - v_s)|_{\partial \mathcal{S}} = (\omega - \omega_s)e_3 \times x, \quad (v - v_s)|_{\Gamma_1} = (v - v_s)|_{\Gamma_2} = -(U - U_s), \qquad (4.2.30)$$
$$\lim_{|x_1| \to \infty} ((v - v_s)(x_1, x_2) + (U - U_s)) = 0.$$

We now expand the quantities v, P, U, and ω in (4.2.30) according to (4.2.28), neglect higher-order terms in Re and obtain that $\overline{v}^{(1)} := v^{(1)}/\text{Fr}^2$ is a solution to the following problem:

$$\begin{cases} \nabla \cdot \sigma_N(\overline{v}^{(1)}, \overline{P}^{(1)}) = (\overline{v}_s \cdot \nabla)\overline{v}_s, \\ \nabla \cdot \overline{v}^{(1)} = 0, \end{cases} \quad \text{in } \Omega,$$
$$\overline{v}^{(1)}_{|S} = \overline{\omega}^{(1)} e_3 \times x, \quad \overline{v}^{(1)}_{|\Gamma_i} = -\overline{U}^{(1)}, \quad \lim_{|x_1| \to \infty} (\overline{v}^{(1)} + \overline{U}^{(1)}) = 0, \qquad (4.2.31)$$

where $\overline{U}^{(1)} := U^{(1)}/\text{Fr}^2$ and $\overline{\omega}^{(1)} := \omega^{(1)}/\text{Fr}^2$.

The second-order contributions $U_1^{(2)}$, $U_2^{(2)}$, $\omega^{(2)}$ can now be obtained by using (4.2.16), (4.2.28), (4.2.29) and by neglecting higher-order terms in Re:

$$\omega^{(2)}\mathcal{R}_1(h) + U_1^{(2)}\mathcal{T}_1(h) = -\text{Fr}^3 \int_\Omega ((\overline{v}_s \cdot \nabla)\overline{v}^{(1)} + (\overline{v}^{(1)} \cdot \nabla)\overline{v}_s) \cdot w^{(1)},$$

$$U_2^{(2)} = -\frac{\text{Fr}^3}{\mathcal{T}_2(h)} \int_\Omega ((\overline{v}_s \cdot \nabla)\overline{v}^{(1)} + (\overline{v}^{(1)} \cdot \nabla)\overline{v}_s) \cdot w^{(2)}, \qquad (4.2.32)$$

$$\omega^{(2)}\mathcal{R}_3(h) + U_1^{(2)}\mathcal{T}_3(h) = -\text{Fr}^3 \int_\Omega ((\overline{v}_s \cdot \nabla)\overline{v}^{(1)} + (\overline{v}^{(1)} \cdot \nabla)\overline{v}_s) \cdot w^{(3)}.$$

To get information at third order in Re the same procedure has to be performed once more: derivation of an equation for $v^{(2)}$ and evaluation of the general equilibrium equations (4.2.16) at third order in Re. In the following we omit the details and directly present the result.

We set $\overline{\omega}^{(2)} := \omega^{(2)}/\text{Fr}^3$, $\overline{U}^{(2)} := U^{(2)}/\text{Fr}^3$ and $\overline{v}^{(2)} := v^{(2)}/\text{Fr}^3$. With these notations $\overline{v}^{(2)}$ is found to solve the following problem:

$$\begin{cases} \nabla \cdot \sigma_N(\overline{v}^{(2)}, \overline{P}^{(2)}) = (\overline{v}_s \cdot \nabla)\overline{v}^{(1)} + (\overline{v}^{(1)} \cdot \nabla)\overline{v}_s, \\ \nabla \cdot \overline{v}^{(2)} = 0, \end{cases} \quad \text{in } \Omega,$$
$$\overline{v}^{(2)}_{|S} = \overline{\omega}^{(2)} e_3 \times x, \quad \overline{v}^{(2)}_{|\Gamma_i} = -\overline{U}^{(2)}, \quad \lim_{|x_1| \to \infty} (\overline{v}^{(2)} + \overline{U}^{(2)}) = 0. \qquad (4.2.33)$$

The third-order contributions $U_1^{(3)}$, $U_2^{(3)}$, $\omega^{(3)}$ can now be obtained by using (4.2.16),(4.2.28), (4.2.29),(4.2.32) and by neglecting higher-order terms in Re:

$$\omega^{(3)}\mathcal{R}_1(h) + U_1^{(3)}\mathcal{T}_1(h) = -\mathrm{Fr}^4 \int_\Omega ((\overline{v}_s \cdot \nabla)\overline{v}^{(2)} + (\overline{v}^{(2)} \cdot \nabla)\overline{v}_s + (\overline{v}^{(1)} \cdot \nabla)\overline{v}^{(1)}) \cdot w^{(1)},$$

$$U_2^{(3)} = -\frac{\mathrm{Fr}^4}{\mathcal{T}_2(h)} \int_\Omega ((\overline{v}_s \cdot \nabla)\overline{v}^{(2)} + (\overline{v}^{(2)} \cdot \nabla)\overline{v}_s + (\overline{v}^{(1)} \cdot \nabla)\overline{v}^{(1)}) \cdot w^{(2)}, \qquad (4.2.34)$$

$$\omega^{(3)}\mathcal{R}_3(h) + U_1^{(3)}\mathcal{T}_3(h) = -\mathrm{Fr}^4 \int_\Omega ((\overline{v}_s \cdot \nabla)\overline{v}^{(2)} + (\overline{v}^{(2)} \cdot \nabla)\overline{v}_s + (\overline{v}^{(1)} \cdot \nabla)\overline{v}^{(1)}) \cdot w^{(3)}.$$

To have consistent notations, we finally set $\overline{\omega}^{(3)} := \omega^{(3)}/\mathrm{Fr}^4$, $\overline{U}^{(3)} := U^{(3)}/\mathrm{Fr}^4$ and $\overline{v}^{(3)} := v^{(3)}/\mathrm{Fr}^4$.

Remark 4.6. The algorithmic realization of the procedure described above is straightforward, albeit somewhat involved. We begin by solving the auxiliary Stokes problems (4.2.6) for $i = 1, 2, 3$ and (4.2.20). Then we compute the surface integrals $\mathcal{T}_i$, $i = 1, 2, 3$, and $\mathcal{F}_i$, $\mathcal{R}_i$, $i = 1, 3$ as defined in (4.2.7),(4.2.8). Solving the linear system (4.2.17) yields the Stokes approximations v_s, P_s, U_s, ω_s ('zero-order approximation'). We are then in position to evaluate the volume integrals occurring on the right-hand side of equations (4.2.25),(4.2.27) or (4.2.29), respectively, which depend on v_s. This gives us $U^{(1)}$ and $\omega^{(1)}$. Next, to get $v^{(1)}$ we solve problem (4.2.31) which depends on the previously computed zero-th and first-order terms v_s, $U^{(1)}$ and $\omega^{(1)}$. To determine the second-order contributions $U^{(2)}$ and $\omega^{(2)}$, we compute the volume integrals in (4.2.32) and solve the linear system. Finally, to get $v^{(2)}$ we solve problem (4.2.33) which depends on the previously computed zero-th, first and second-order terms v_s, $v^{(1)}$, $U^{(2)}$ and $\omega^{(2)}$. The third-order contributions $U^{(3)}$ and $\omega^{(3)}$ are then obtained by solving (4.2.34).

Remark 4.7. In anticipation of the presentation of numerical results in Section 4.4 we would like to mention an interesting phenomenon that was brought to light by the simulations. We found that, for any $h \in (a, 1 - a)$, the terms $U_1^{(1)}$, $\omega^{(1)}$, $U_1^{(3)}$, $\omega^{(3)}$, as well as the terms $U_2^{(0)} := U_{s2}$ and $U_2^{(2)}$ are practically zero, from a computational point of view. This suggests that U_1 and ω (U_2, resp.) allow for an expansion in *even* (*odd*, resp.) powers of Re,

$$
\begin{array}{llllll}
\omega & = & \omega_s & +\mathrm{Re}^2\omega^{(2)} & +\mathrm{Re}^4\omega^{(4)} & +\dots, \\
U_1 & = & U_{s1} & +\mathrm{Re}^2 U_1^{(2)} & +\mathrm{Re}^4 U_1^{(4)} & +\dots, \\
U_2 & = & \mathrm{Re}\, U_2^{(1)} & +\mathrm{Re}^3 U_2^{(3)} & +\mathrm{Re}^5 U_2^{(5)} & +\dots.
\end{array} \qquad (4.2.35)
$$

4.3 Solution process

The main numerical task needed to put the ideas described above into practice is the solution of a number of auxiliary Stokes problems. To get information at first order in Re and We, the three problems (4.2.6), for $i = 1, 2, 3$, have to be solved, as well as problem (4.2.20).

For a simulation up to third order in Re, we need to solve (4.2.6) for $i = 1, 2, 3$, and in addition (4.2.20),(4.2.31),(4.2.33). In order to obtain accurate information about the possible equilibrium positions of the particle these Stokes problems have to be solved for a large number (typically 50-100) of particle positions h. So a typical simulation up to third order in Re for *one* set of parameters $\{\mathrm{Fr}, \mathrm{Re}, \overline{\alpha}\}$ *requires the solution of 300-600 Stokes problems*! One should also keep in mind that the unbounded channel geometry of the continuous formulation has to be replaced by a truncated finite channel. In order to keep the impact of the artifical boundaries on the quantities of interest low, one has to take quite long channels for the simulations, cf. the discussion in Chapter 3. The computational effort to implement the method presented above is therefore very high. In order to reduce it we use, once more, the technique of *local grid refinement* in the context of a Galerkin finite element method. A typical computational grid is shown in Figure 4.2.

The finite element discretization of the (homogeneous, for simplicity) Stokes problem on a bounded domain D with Dirichlet boundary conditions,

$$-\Delta v + \nabla p = 0, \quad \nabla \cdot v = 0 \text{ in } D, \quad v_{|\partial D} = v^{\partial}, \tag{4.3.1}$$

starts from a variational formulation. Let $W = [H_0^1(D)]^2 \times L_0^2(D)$. For $U = \{v, p\} \in [v^{\partial} + H_0^1(D)^2] \times L_0^2(D)$ and $\Phi = \{\varphi, q\} \in W$, we define the bilinear form

$$A(U)(\Phi) := (\nabla v, \nabla \varphi)_D - (p, \nabla \cdot \varphi)_D - (\nabla \cdot v, q)_D. \tag{4.3.2}$$

A weak form of equation (4.3.1) then reads as follows:

Find $U = \{v, p\} \in [v^{\partial} + H_0^1(D)^2] \times L_0^2(D)$, such that

$$A(U)(\Phi) = 0, \quad \forall \Phi \in W. \tag{4.3.3}$$

Equation (4.3.3) is now discretized by means of the finite element method on locally refined meshes consisting of quadrilateral cells. As elements for velocity and pressure we take 'equal-order' Q_1 elements, i.e. we define

$$W_h := \left\{ (v, p) \in [C(\overline{D})]^3; \quad v|_K \in [Q_1]^2, p|_K \in Q_1 \right\},$$

where Q_1 describes the space of bilinear tensor-product polynomials. This spatial discretization needs stabilization in order to compensate for the lacking 'inf-sup stability', see e.g. Rannacher [Ran00]. As an alternative to the usual SDLS (Streamline Diffusion Least-Squares) or SUPG (Streamline Upwinded Petrov Galerkin) stabilization of Hughes et al. [HB82, HFB86], we suggest the LPS (Local Projection Stabilization) method proposed in Becker/Braack [BB01] and Braack/Burman [BrB06] which has several advantages over the other stabilization methods.

The discrete counterpart of problem (4.3.3) then reads: Find $U_h = \{v_h, p_h\} \in \{v_h^{\partial}, 0\} + W_h$, such that

$$A(U_h)(\Phi_h) + S_\delta(U_h)(\Phi_h) = 0, \quad \forall \Phi_h \in W_h. \tag{4.3.4}$$

Here, $S_\delta(U_h)(\Phi_h)$ denotes the additional stabilization form. This system is solved in a fully-coupled manner by the Generalized Minimal Residual Method (GMRES) with preconditioning by a geometric multigrid method with block-ILU smoothing. All simulations were done using the finite element simulation package **Gascoigne3D** (see Becker et al. [BB$^+$05]). The visualization of the results was done with **HiVision** (see Bönisch/Heuveline [BH06]).
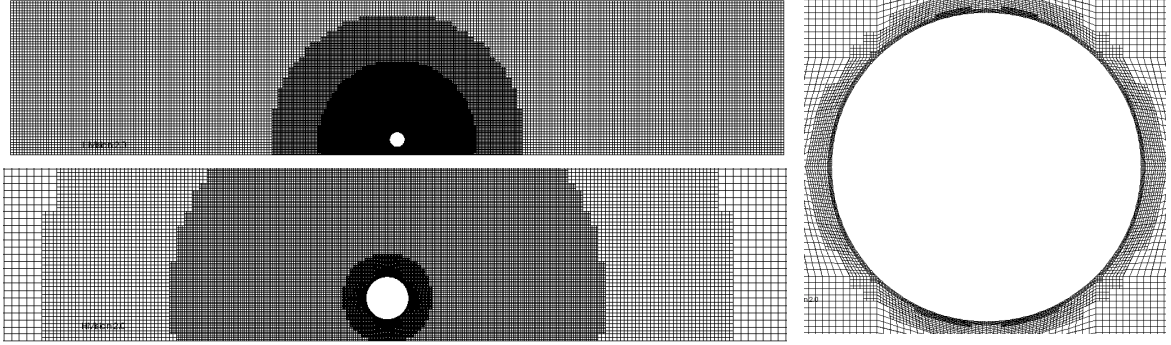
Figure 4.2: A typical, locally refined mesh employed in our computations. **Top-left**: the whole channel, **Bottom-left** and **Right**: zoom on the particle.

4.4 Numerical results

In this section we present comprehensive numerical results obtained by using the method described above. We consider a disk of radius $R = 0.05$ sedimenting in an infinite vertical channel of width $W_C = 1$. The length of the truncated channel used for the numerical computations is $L_C = 5$. (A comparison with a channel of length $L_C = 10$ showed no significant differences. Therefore we can conclude that $L_C = 5$ is enough.)

The material is organized as follows: In Section 4.4.1 we treat the case of a sedimenting cylinder when the fluid flow is in the same direction as the gravity (downward-directed Poiseuille flow). Section 4.4.2 then is devoted to the case of upward-directed Poiseuille flow. In any case, we shall start with a purely Newtonian liquid ($E = 0$) and determine - at first order - the equilibrium positions in dependence of the (scaled) buoyancy $\overline{\alpha} = \alpha/\text{Fr}$, beginning with $\overline{\alpha} = 0$ (neutrally buoyant particle). We then increase the elasticity number E and examine how the position and stability of equilibria is affected. In the last part of each of the Sections 4.4.1, 4.4.2 we present third-order results for a purely Newtonian liquid. The number and the stability of equilibrium positions strongly depends on the choice of the parameters $\overline{\alpha}$, Fr and Re.

Remark 4.8. In the numerical simulations we always determine the barred quantities $\overline{U}^{(i)}$, $\overline{\omega}^{(i)}$. The actual quantities of interest, U and ω, are related to those by

$$
\begin{aligned}
U &= \text{Fr}\,\overline{U}_s + \text{Fr}^2\,(\text{Re} + \text{We})\overline{U}^{(1)} + \dots, \\
\omega &= \text{Fr}\,\overline{\omega}_s + \text{Fr}^2\,(\text{Re} + \text{We})\overline{\omega}^{(1)} + \dots,
\end{aligned}
\tag{4.4.1}
$$

in the case of the first-order expansion in Re and We, and by

$$
\begin{aligned}
U &= \text{Fr}\,\overline{U}_s + \text{Fr}^2\,\text{Re}\,\overline{U}^{(1)} + \text{Fr}^3\,\text{Re}^2\overline{U}^{(2)} + \text{Fr}^4\,\text{Re}^3\overline{U}^{(3)} + \dots, \\
\omega &= \text{Fr}\,\overline{\omega_s} + \text{Fr}^2\,\text{Re}\,\overline{\omega}^{(1)} + \text{Fr}^3\,\text{Re}^2\overline{\omega}^{(2)} + \text{Fr}^4\,\text{Re}^3\overline{\omega}^{(3)} + \dots,
\end{aligned}
\tag{4.4.2}
$$

in the case of the third-order expansion in Re. So, in principle one has to track the dependence of U and ω on Fr as well as on Re. This ambivalence could easily lead to confusion.

Therefore we normalize the quantities in the following way:

$$U/\mathrm{Fr} = \overline{U}_s + \mathrm{Fr}\,\mathrm{Re}\,(1+E)\overline{U}^{(1)} + \cdots \equiv \tilde{U},$$
$$\omega/\mathrm{Fr} = \overline{\omega}_s + \mathrm{Fr}\,\mathrm{Re}\,(1+E)\overline{\omega}^{(1)} + \cdots \equiv \tilde{\omega},$$
(4.4.3)

and

$$U/\mathrm{Fr} = \overline{U}_s + \mathrm{Fr}\,\mathrm{Re}\,\overline{U}^{(1)} + (\mathrm{Fr}\,\mathrm{Re}\,)^2\overline{U}^{(2)} + (\mathrm{Fr}\,\mathrm{Re}\,)^3\overline{U}^{(3)} + \cdots \equiv \tilde{U},$$
$$\omega/\mathrm{Fr} = \overline{\omega_s} + \mathrm{Fr}\,\mathrm{Re}\,\overline{\omega}^{(1)} + (\mathrm{Fr}\,\mathrm{Re}\,)^2\overline{\omega}^{(2)} + (\mathrm{Fr}\,\mathrm{Re}\,)^3\overline{\omega}^{(3)} + \cdots \equiv \tilde{\omega}.$$
(4.4.4)

Then everything depends on the single parameter $\mathrm{Fr}\,\mathrm{Re}\,$. It is clear that neither the position nor the stability of equilibria is affected by this scaling.

Remark 4.9. For a better understanding of the particle dynamics we will extensively plot 'pseudo-trajectories'. So, if $\tilde{U} = (\tilde{U}_1, \tilde{U}_2)$ denotes the normalized translational velocity of the particle introduced above, we plot curves $\{(x_1(t), x_2(t)),\ t \geq 0\}$ which are defined as solutions of the initial-value problems

$$\dot{x}_1 = \tilde{U}_1, \quad x_1(0) = 0,$$
$$\dot{x}_2 = \tilde{U}_2, \quad x_2(0) = h_0,$$
(4.4.5)

for different initial heights h_0. Of course, the resulting curves are not identical with the 'real', i.e. instationary particle trajectories, since for each h the velocity $\tilde{U} = \tilde{U}(h)$ is the result of solving the *stationary* fluid-particle equations.

4.4.1 Downward-directed Poiseuille flow

Results at first order in Re and We

We recall from Section 4.2.3 that the equilibrium heights h_{equi} are given, at first order in Re and We, by the solutions to equation (4.2.26), that is,

$$\mathcal{G}(h; \overline{\alpha}) + E\mathcal{G}_V(h; \overline{\alpha}) = 0.$$
(4.4.6)

First we will describe the results for the purely Newtonian case, $E = 0$. (These results are summarized in Table 4.1.) Equilibria are then characterized as zeros of the function $\mathcal{G}(\cdot; \overline{\alpha})$. In the following, we subsequently increase $\overline{\alpha}$, starting with $\overline{\alpha} = 0$ (neutrally buoyant case). With a view to Figure 4.3 (top left), we find three[4] possible solutions,

$$h_{equi}^{(1)} \approx 0.26, \quad h_{equi}^{(2)} = 0.5, \quad h_{equi}^{(3)} \approx 1 - 0.26 = 0.74.$$

Notice that $h_{equi}^{(1)}$ and $h_{equi}^{(3)}$ are *stable* equilibria, while $h_{equi}^{(2)}$ is *unstable*. This can be estab- lished as follows: Consider a small variation δh at the equilibrium position $h_{equi}^{(1)}$. If $\delta h < 0$, we get that $\mathcal{G}(h + \delta h; \overline{\alpha})$ is positive. $U_2^{(1)}(h + \delta h)$ is hence positive, too, in view of equation

---

[4] All plots in this section refer to the range $h \in (0, 0.5]$, i.e. only the lower half of the channel is shown. This is sufficient, because the problem is symmetric with respect to the center line $\{h = 0.5\}$. However, when it comes to *counting* the number of equilibria we will always refer to the whole channel!

(4.2.25). This means that the fluid will exert a force in the upward direction that will bring the particle back to $h_{equi}^{(1)}$. Analogously, if $\delta h > 0$ then $\mathcal{G}(h + \delta h; \overline{\alpha})$ is negative and the fluid will exert a force in the downward direction that will bring the particle back to $h_{equi}^{(1)}$, too. Repeating exactly the same argument, we find that $h_{equi}^{(3)}$ is stable and $h_{equi}^{(2)}$ is unstable. (The trajectories shown in Figure 4.3 illustrate this fact.) For later considerations, we may summarize this result by saying that a given equilibrium position h_{equi} is *stable* if the slope of $\mathcal{G}(h; \overline{\alpha})$ is *negative* at $h = h_{equi}$, and that it is *unstable* if the slope is *positive*.

Our findings for the case $\overline{\alpha} = 0$ are in very good agreement with the classical experimental observations by Segrè and Silberberg [SS61, SS62]. These authors studied the migration of neutrally buoyant spheres in pipe flows at Reynolds numbers between 2 and 700, and found that the spheres migrate away from the wall and centerline and cluster at about 0.6 of a pipe radius ('Segrè-Silberberg effect'.)

We now discuss the case $\overline{\alpha} > 0$. Figures 4.4, 4.5 and 4.6 correspond to $\overline{\alpha} = 0.5$, $\overline{\alpha} = 1$ and $\overline{\alpha} = 1.5$, respectively. What we found is the following: The two stable equilibrium positions $h_{equi}^{(1)}$ and $h_{equi}^{(3)}$ both move towards the walls as $\overline{\alpha}$ increases. Furthermore, there is a critical (scaled) buoyancy $\overline{\alpha}_c$ such that if $\overline{\alpha} < \overline{\alpha}_c$, the equilibria $h_{equi}^{(1)}$ and $h_{equi}^{(3)}$ are the *only* stable equilibria. If, however, $\overline{\alpha} > \overline{\alpha}_c$, the center position $h_{equi}^{(2)} = 0.5$ becomes a *third stable* equilibrium position. A physical interpretation of this phenomenon is the following. If the particle is 'heavy enough', it falls so rapidly that it completely 'leads' the flow, in other words: it does not really 'feel' the Poiseuille inflow. The fluid, as seen from the particle, therefore behaves essentially stagnant. For a sedimenting disk in a stagnant fluid, however, we know from previous computations that the center position is in fact a stable equilibrium, cf. Galdi/Heuveline [GH06].

Concerning the **viscoelastic case** ($E > 0$) we found the following, see Figure 4.3–4.6. For relatively small values of $\overline{\alpha}$, as we increase the elasticity number, the stable off-center equilibrium positions move toward the center of the channel. Eventually, for E large enough, the center becomes the only stable position.

However, for large values of $\overline{\alpha}$ the situation approaches the limit case of a stagnant fluid (no 'effective' Poiseuille flow). For such a case we know from Galdi/Heuveline [GH06] that elasticity acts to push the particle towards the walls. In Figure 4.7 we show the variation of $\mathcal{G}_V(h)$ when $\overline{\alpha} = 100$. In fact, we see that elasticity acts to destroy the stability of the center equilibrium and to push the particle toward the walls.
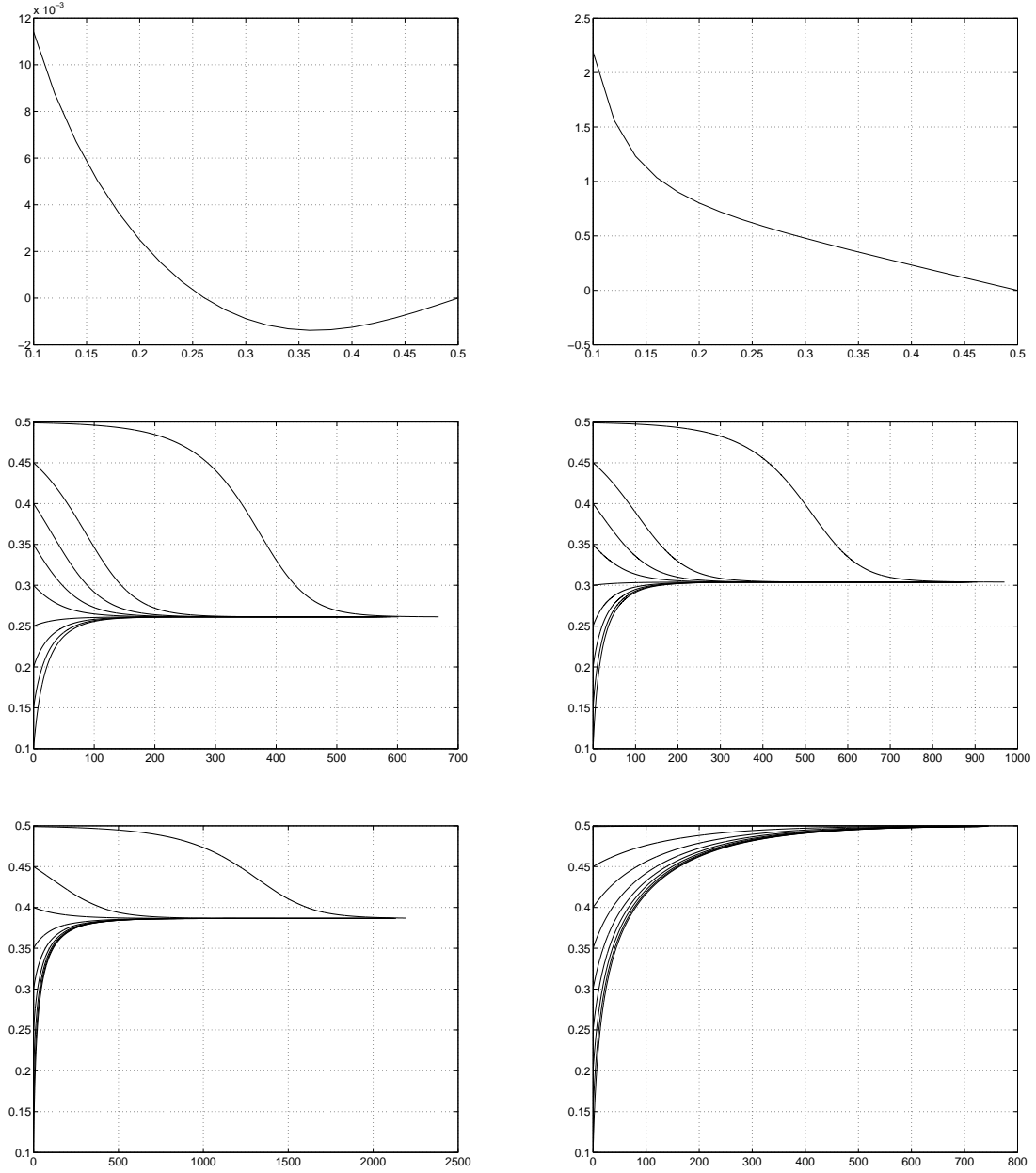
Figure 4.3: Results at first order in Re and We for the case of a downward Poiseuille flow, where $\overline{\alpha} = 0$ and $\mathrm{Fr}\,\mathrm{Re} = 10$. $\mathcal{G}(h)$ and $\mathcal{G}_V(h)$ vs. h (**first row**) and trajectories for $E = 0$, $E = 0.002$ (**second row**) and $E = 0.005$, $E = 0.01$ (**third row**).
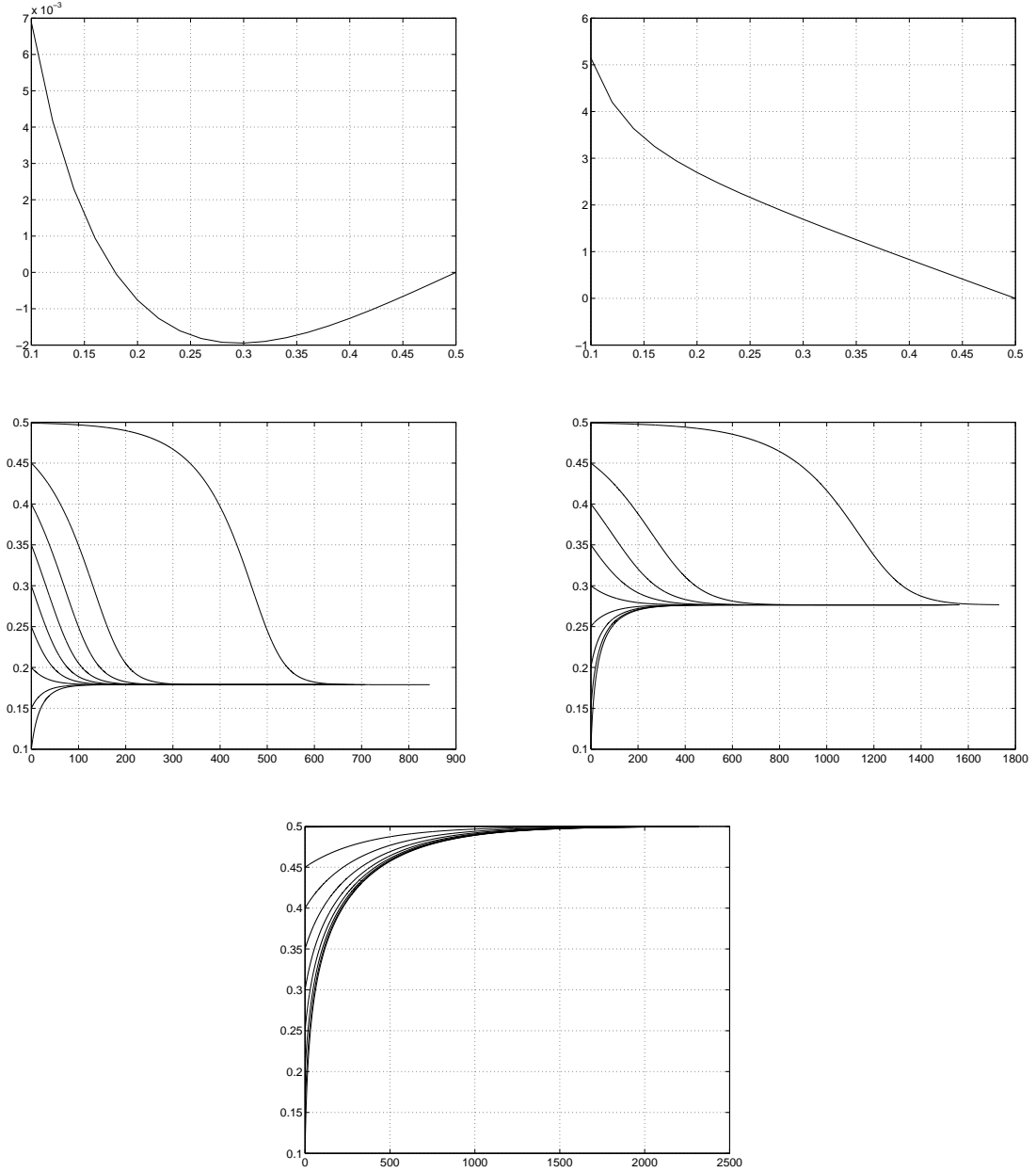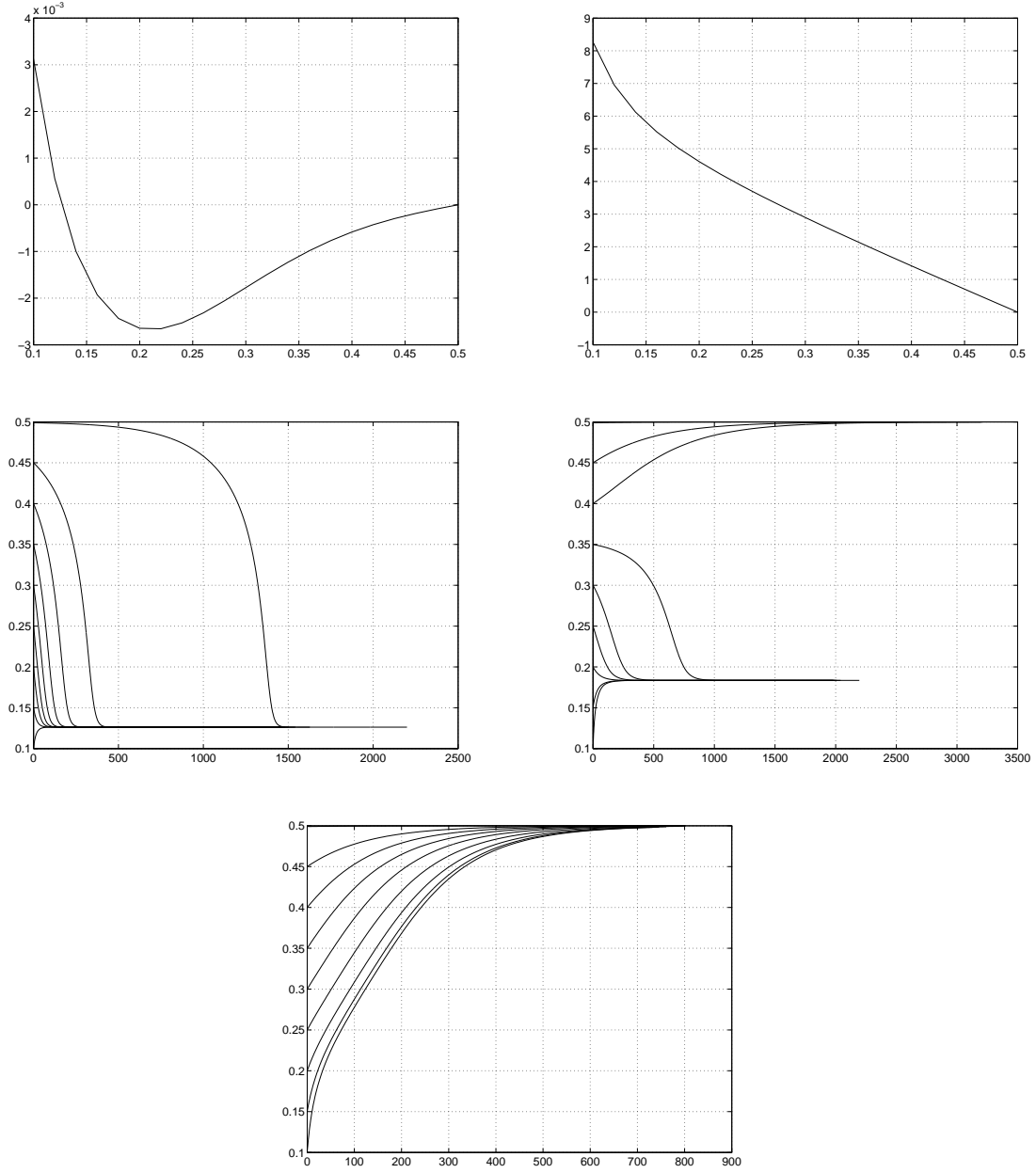
Figure 4.4: Results at first order in Re and We for the case of a downward Poiseuille flow, where $\overline{\alpha} = 0.5$ and $\mathrm{Fr}\,\mathrm{Re} = 10$. $\mathcal{G}(h)$ and $\mathcal{G}_V(h)$ vs. h (**first row**) and trajectories for $E = 0$, $E = 0.001$ (**second row**) and $E = 0.002$ (**third row**).
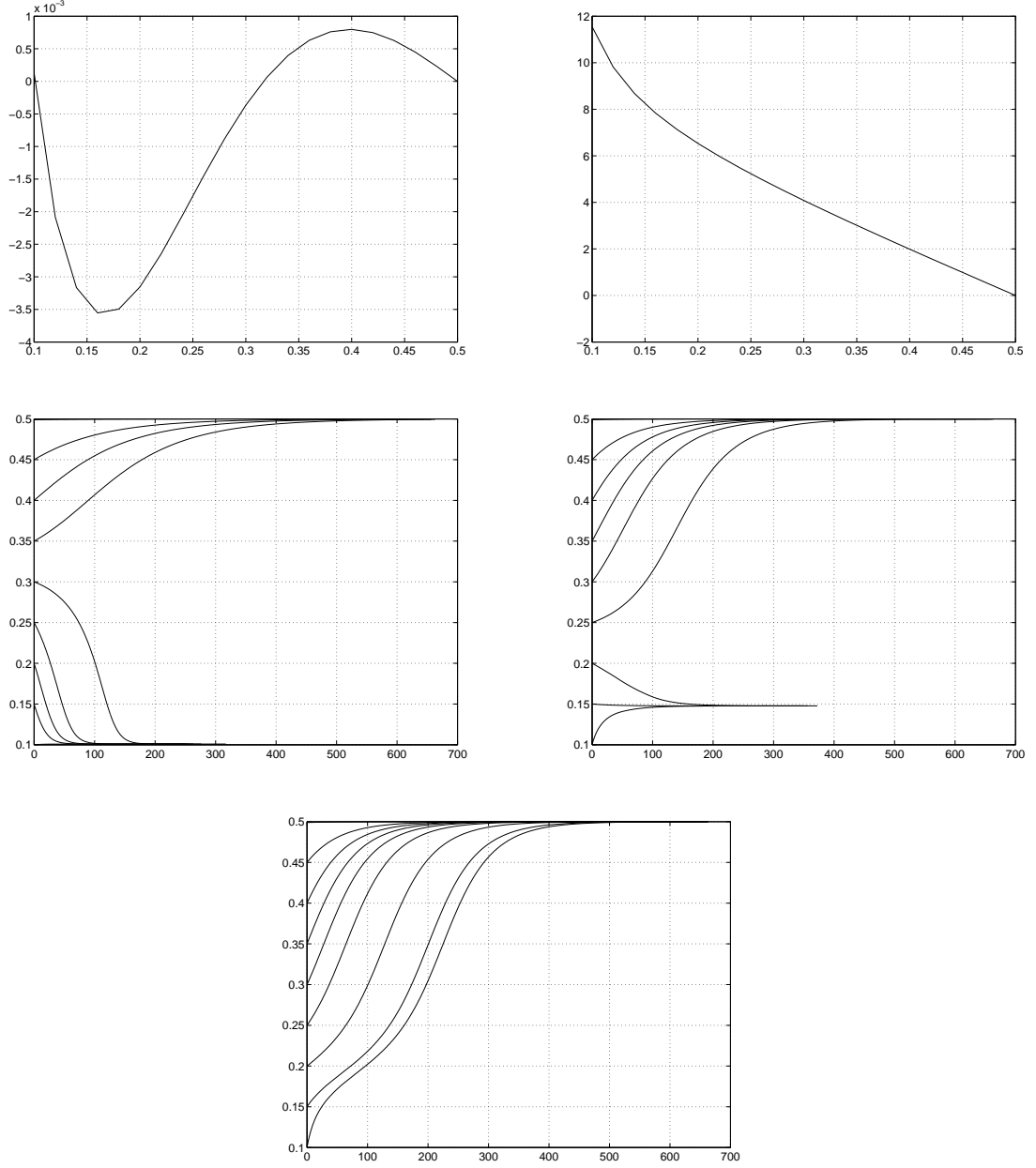
Figure 4.5: Results at first order in Re and We for the case of a downward Poiseuille flow, where $\overline{\alpha} = 1$ and $\mathrm{Fr}\,\mathrm{Re} = 10$. $\mathcal{G}(h)$ and $\mathcal{G}_V(h)$ vs. h (**first row**) and trajectories for $E = 0$, $E = 0.0005$ (**second row**) and $E = 0.001$ (**third row**).

Figure 4.6: Results at first order in Re and We for the case of a downward Poiseuille flow, where $\overline{\alpha} = 1.5$ and $\mathrm{Fr\,Re} = 10$. $\mathcal{G}(h)$ and $\mathcal{G}_V(h)$ vs. h (**first row**) and trajectories for $E = 0$, $E = 0.0004$ (**second row**) and $E = 0.0006$ (**third row**).

Table 4.1: Number, position and stability of equilibrium positions for different values of $\overline{\alpha}$. The Poiseuille flow is directed downwards. The fluid is purely Newtonian ($E = 0$) and $\mathrm{Fr}\,\mathrm{Re} = 10$. Equilibria are computed at first order in Re.

| $\overline{\alpha}$	
0	neutrally buoyant case; two stable equilibrium positions, symmetric with respect to the center line ('Segrè-Silberberg effect'). The equilibrium in the middle of the channel is unstable (Figure 4.3).
0.5	The equilibrium positions are shifted towards the walls (Figure 4.4).
1	The equilibrium positions move further towards the walls. The center equilibrium is still unstable (Figure 4.5).
1.5	The off-center equilibrium positions move further towards the walls. The center has become another stable equilibrium (Figure 4.6).
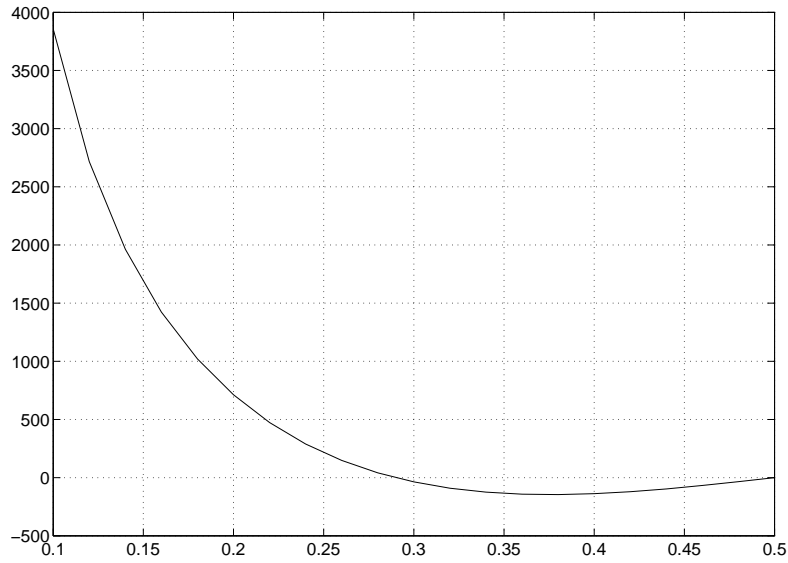
Figure 4.7: Results at first order in Re and We for the case of a downward Poiseuille flow, $\overline{\alpha} = 100$. The viscoelastic contribution $\mathcal{G}_V(h)$ to the lift is plotted vs. h. Compare this curve to the corresponding one for smaller values of $\overline{\alpha}$, Figures 4.3–4.6).

Results at third order in Re

The equilibrium heights h_{equi} are given, at third order in Re, by the solutions to

$$\operatorname{Re} U_2^{(1)}(h) + \operatorname{Re}^2 U_2^{(2)}(h) + \operatorname{Re}^3 U_2^{(3)}(h) = 0.$$

We recall (see the second equation in (4.2.29), (4.2.32) and (4.2.34), respectively) that the (scaled) first, second and third-order contributions to U_2 are given by

$$\overline{U}_2^{(1)} = -\frac{1}{\mathcal{T}_2(h)} \int_\Omega ((\overline{v}_s \cdot \nabla)\overline{v}_s) \cdot w^{(2)} \equiv \frac{1}{\mathcal{T}_2(h)} \mathcal{G}^{(1)}(h; \overline{\alpha}),$$

$$\overline{U}_2^{(2)} = -\frac{1}{\mathcal{T}_2(h)} \int_\Omega ((\overline{v}_s \cdot \nabla)\overline{v}^{(1)} + (\overline{v}^{(1)} \cdot \nabla)\overline{v}_s) \cdot w^{(2)} \equiv \frac{1}{\mathcal{T}_2(h)} \mathcal{G}^{(2)}(h; \overline{\alpha}),$$

$$\overline{U}_2^{(3)} = -\frac{1}{\mathcal{T}_2(h)} \int_\Omega ((\overline{v}_s \cdot \nabla)\overline{v}^{(2)} + (\overline{v}^{(2)} \cdot \nabla)\overline{v}_s + (\overline{v}^{(1)} \cdot \nabla)\overline{v}^{(1)}) \cdot w^{(2)} \equiv \frac{1}{\mathcal{T}_2(h)} \mathcal{G}^{(3)}(h; \overline{\alpha}).$$

$$(4.4.7)$$

The integral defining $\mathcal{G}^{(2)}(h)$ was numerically found to be zero for any h (see Remark 4.7). Hence the equilibrium positions h_{equi} are characterized as solutions to the equation

$$\tilde{U}_2(h) = \operatorname{Fr}\operatorname{Re}\overline{U}_2^{(1)}(h) + (\operatorname{Fr}\operatorname{Re})^3\overline{U}_2^{(3)}(h) = 0. \tag{4.4.8}$$

In Figures 4.8–4.11 we present numerical results for $\overline{\alpha} \in \{0, 0.5, 1, 1.5\}$. For each value of $\overline{\alpha}$ we plot the following characteristic quantities:

- the first and third-order contributions $\mathcal{G}^{(1)}$ and $\mathcal{G}^{(3)}$ to the lift (see (4.4.7)),
- $\tilde{U}_2$ as in (4.4.8), for different values of $\operatorname{Fr}\operatorname{Re}$,
- the particle 'trajectories' $\{(x_1(t), x_2(t)), \ t \geq 0\}$ computed according to (4.4.5), for different values of $\operatorname{Fr}\operatorname{Re}$.

Let us begin with $\overline{\alpha} = 0$. With a view to Figure 4.8 (first row), we see that the 'first-order equilibria'

$$h_{equi}^{(1)} \approx 0.26, \quad h_{equi}^{(2)} = 0.5, \quad h_{equi}^{(3)} \approx 0.74,$$

see above, are also zeros of the function $\mathcal{G}^{(3)}(h)$. However, the slope of $\mathcal{G}^{(1)}(h)$ and $\mathcal{G}^{(3)}(h)$ has *opposite sign* at $h_{equi}^{(i)}$, $i = 1, 2, 3$. That means that there is a *competition between the first and third-order contributions* concerning the stability of equilibria. For small values of $\operatorname{Fr}\operatorname{Re}$, the first-order term dominates and the two off-center equilibria $h_{equi}^{(1)}$ and $h_{equi}^{(3)}$ are stable. For $\operatorname{Fr}\operatorname{Re}$ large enough, however, third-order effects become more important and the off-center equilibria lose their stability while the center equilibrium becomes stable. For certain intermediate values of $\operatorname{Fr}\operatorname{Re}$, two additional unstable equilibria $h_{equi}^{(4)}$ and $h_{equi}^{(5)}$ occur. The (rather complex) dependency of the number and stability of equilibrium positions on the parameter $\operatorname{Fr}\operatorname{Re}$ is also summarized in Table 4.2.

Let us turn now to the case of a non-neutrally buoyant particle ($\overline{\alpha} > 0$). Figures 4.9, 4.10, 4.11 show the results corresponding to $\overline{\alpha} = 0.5$, $\overline{\alpha} = 1$ and $\overline{\alpha} = 1.5$, respectively.

Table 4.2: Number and stability of equilibrium positions for $\overline{\alpha} = 0$ (**left**), $\overline{\alpha} = 1$ (**middle**) and $\overline{\alpha} = 1.5$ (**right**). The Poiseuille flow is directed downwards. The fluid is purely Newtonian ($E = 0$) and equilibria are computed at third order in Re.

	$\overline{\alpha} = 0$			$\overline{\alpha} = 1$		$\overline{\alpha} = 1.5$	
Fr Re	10	30	70	10	50	5	50
#equilibria	3	5	3	3	1	5	3
#stable eq.	2	2	1	2	0	3	2
center stable	no	no	yes	no	no	yes	no

Like in the case $\overline{\alpha} = 0$ we found different trajectory patterns and a different number of equilibrium positions, depending on $\overline{\alpha}$ and Fr Re. (The number and stability of equilibria are also summarized in Table 4.2.) The overall trend that we can extract from the data is the following: Increasing Fr Re for fixed $\overline{\alpha}$ effectuates a shift of the off-center equilibria *towards the walls*. The same happens if we fix Fr Re and increase $\overline{\alpha}$.
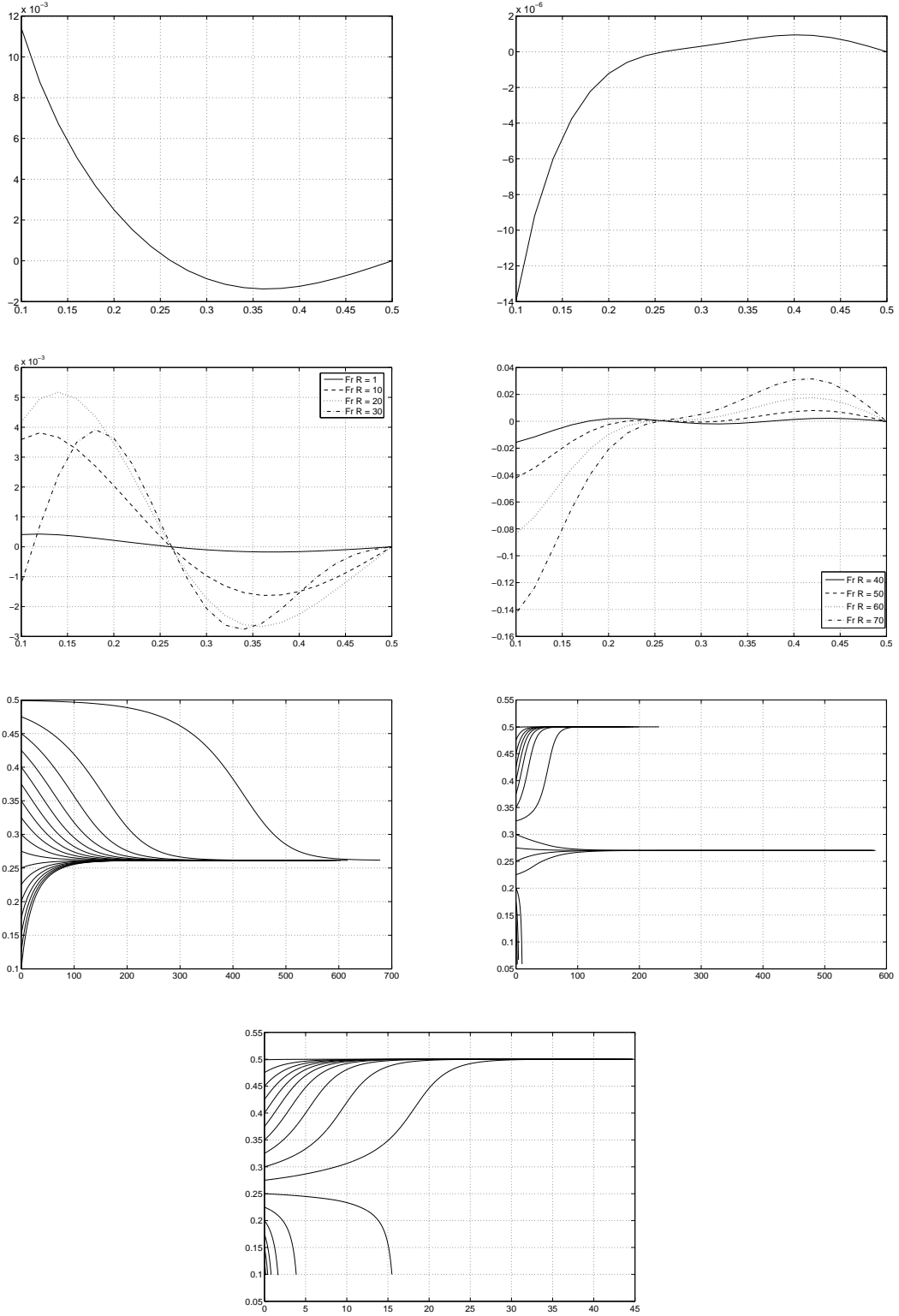
Figure 4.8: Results at third order in Re for the case of a downward Poiseuille flow, $\overline{\alpha} = 0$. $\mathcal{G}^{(1)}(h)$ and $\mathcal{G}^{(3)}(h)$ vs. h (**first row**), $\tilde{U}_2$ vs. h for different values of Fr Re (**second row**), and trajectories for Fr Re $\in \{10, 50, 70\}$ (**third & fourth row**).
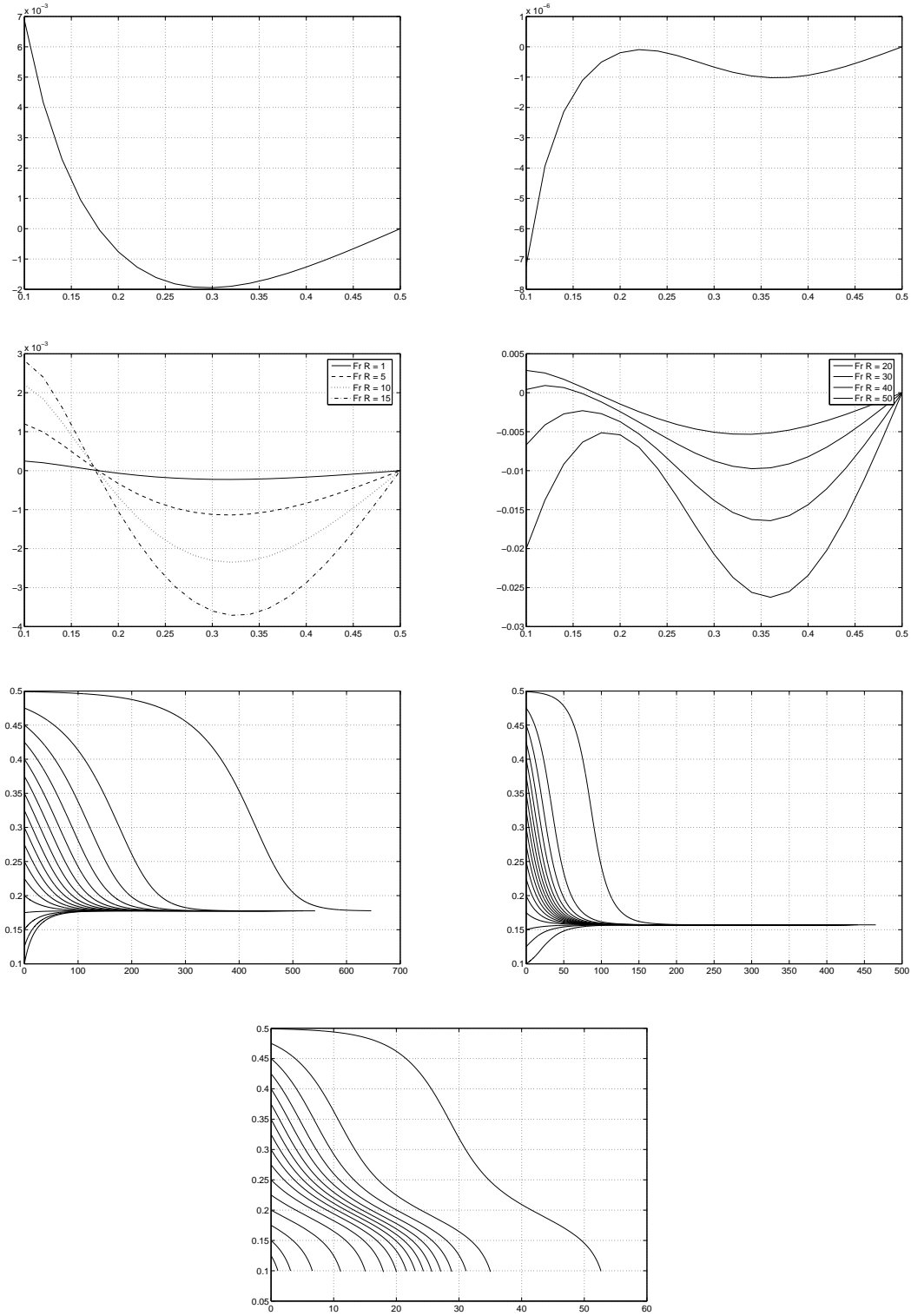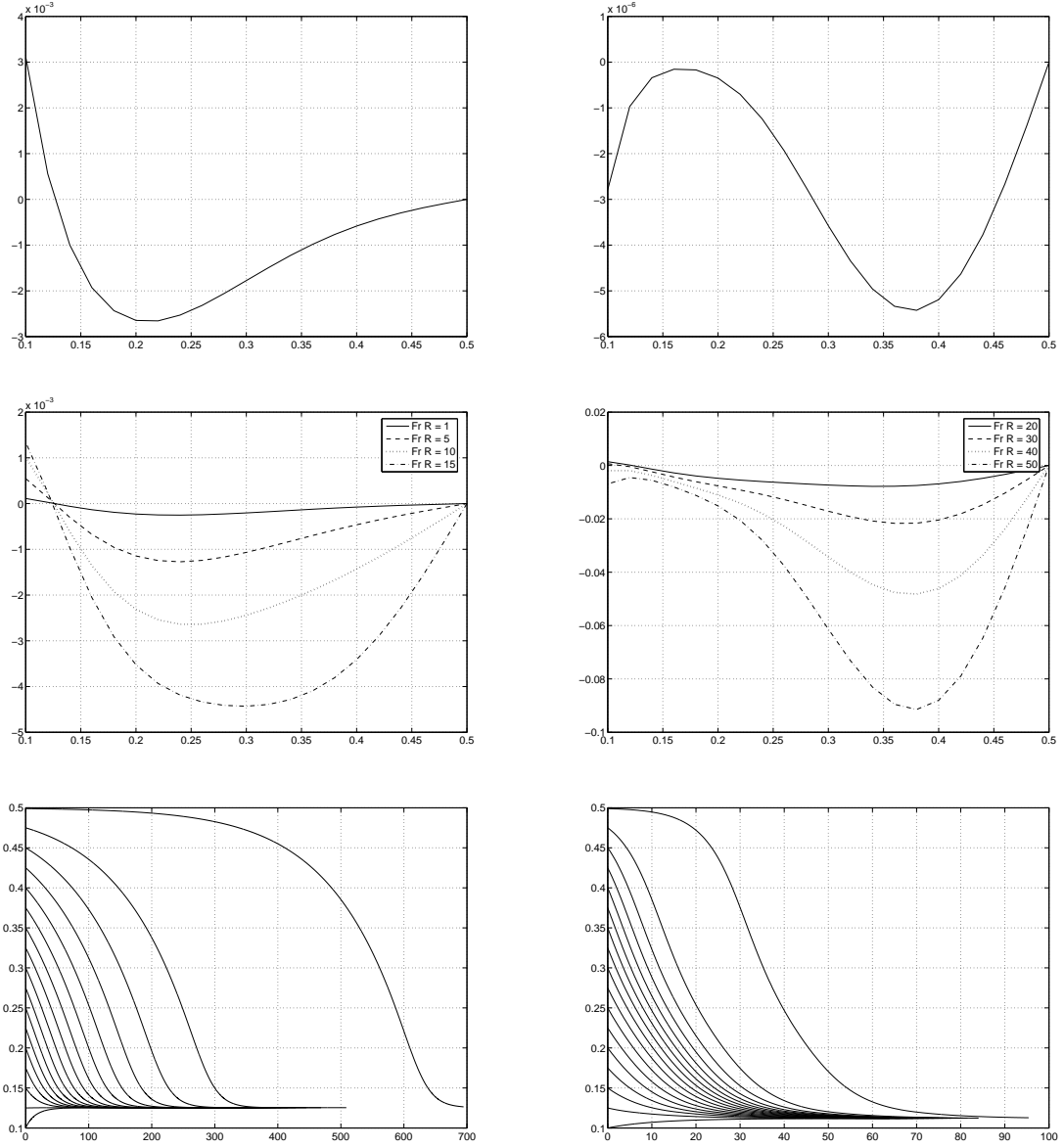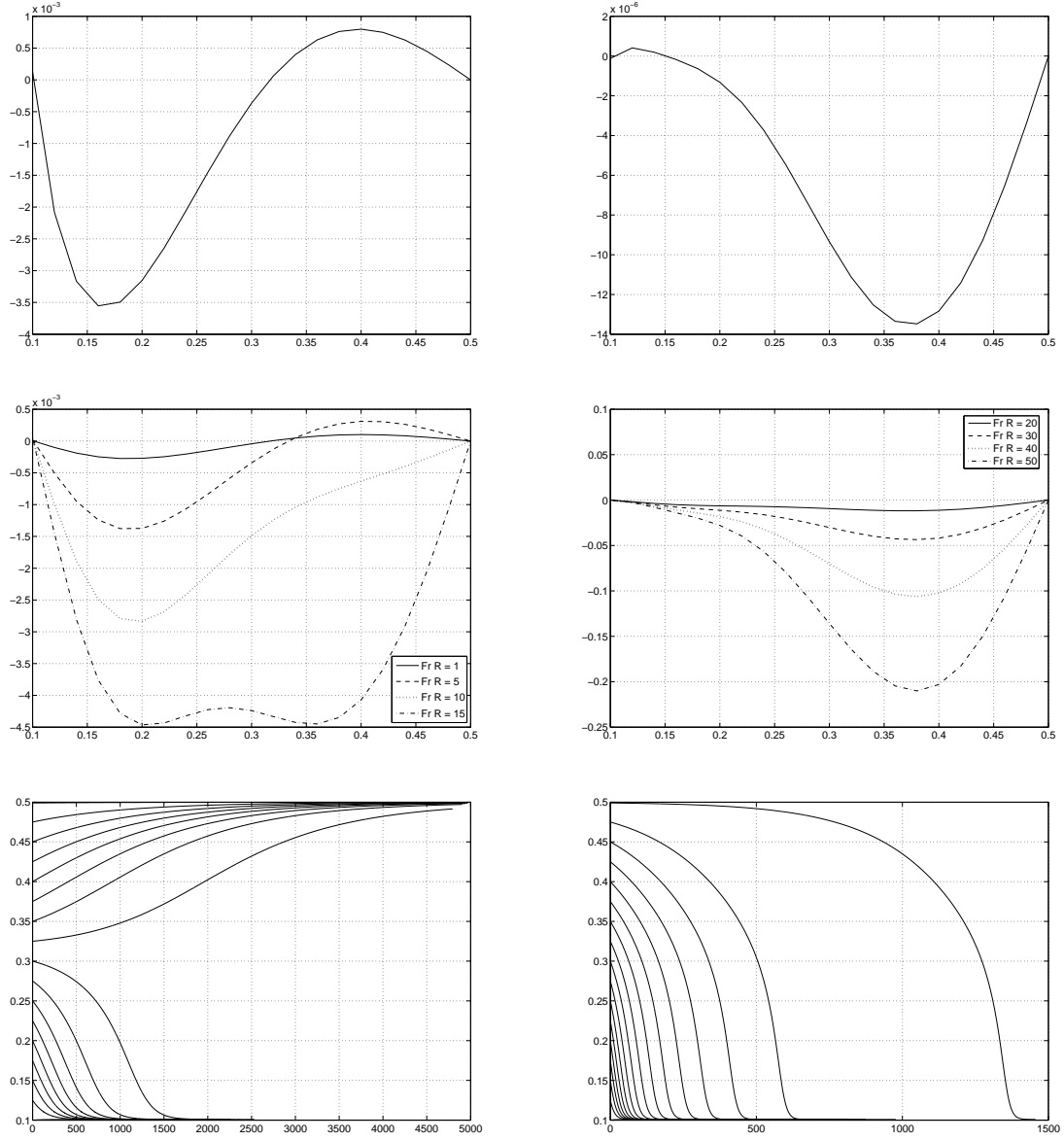
Figure 4.9: Results at third order in Re for the case of a downward Poiseuille flow, $\overline{\alpha} = 0.5$. $\mathcal{G}^{(1)}(h)$ and $\mathcal{G}^{(3)}(h)$ vs. h (**first row**), $\tilde{U}_2$ vs. h for different values of Fr Re (**second row**), and trajectories for Fr Re $\in \{10, 30, 50\}$ (**third & fourth row**).

Figure 4.10: Results at third order in Re for the case of a downward Poiseuille flow, $\overline{\alpha} = 1$. $\mathcal{G}^{(1)}(h)$ and $\mathcal{G}^{(3)}(h)$ vs. h (**first row**), $\tilde{U}_2$ vs. h for different values of $\mathrm{Fr}\,\mathrm{Re}$ (**second row**), and trajectories for $\mathrm{Fr}\,\mathrm{Re} \in \{10, 30\}$ (**third row**).

Figure 4.11: Results at third order in Re for the case of a downward Poiseuille flow, $\overline{\alpha} = 1.5$. $\mathcal{G}^{(1)}(h)$ and $\mathcal{G}^{(3)}(h)$ vs. h (**first row**), $\tilde{U}_2$ vs. h for different values of Fr Re (**second row**), and trajectories for Fr Re $\in \{1, 10\}$ (**third row**).

4.4.2 Upward-directed Poiseuille flow

We now turn to the situation when the channel Poiseuille flow is in opposite direction than the gravitational force. It is clear that in such a case, the particle will sediment only if it is heavy enough; if it is too light, it will be blown upwards by the fluid flow. Moreover it is known (see Section 4.1) that if the liquid is Newtonian and viscous enough, a (spherical) particle settling through an upward Poiseuille flow always goes to the center of the channel. Consequently, in such a case one can bring the particle to rest in the middle of the channel by adjusting the flow rate Φ (or, equivalently, the Froude number Fr or the maximum velocity of the parabolic inflow profile). It is clear that for a given buoyancy α there is one and only one such 'fluidization flow rate', see also Joseph [Jos00], Chapter VI. Using as decisive parameter the scaled buoyancy $\overline{\alpha} = \alpha/\text{Fr}$, the 'stabilization problem' reads as follows: Find $\overline{\alpha}^*$ such that the resulting translational velocity $U_1 = U_1(h; \overline{\alpha})$ vanishes at $h = 0.5$,

$$U_1(0.5; \overline{\alpha}^*) = 0.$$

In the following we will compute $\overline{\alpha}^*$. Since we only want to show the basic principle we will restrict ourselves to satisfying the condition $U_1 = 0$ at *first order in Re*, cf. Remark 4.10.

Stabilization of the particle at first order

We recall from Theorem 4.1 the asymptotic expansion for U_1,

$$U_1 = U_{s1} + \text{Re}\, U_1^{(1)} + \mathcal{O}(\text{Re}^2).$$

Numerically, we found (see Remark 4.7) that $U_1^{(1)} = 0$. This means that in order to satisfy the condition $U_1 = 0$ at first order in Re it is enough to enforce it at zeroth order. So we consider the Stokes field $v_s = v_s(h)$ and require that $U_{s1}(0.5; \overline{\alpha}) = 0$. Then (4.2.19) shrinks to

$$\begin{aligned}
\overline{\omega}_s(0.5)\mathcal{R}_1(0.5) &= \mathcal{F}_1(0.5) + \overline{\alpha}, \\
\overline{\omega}_s(0.5)\mathcal{R}_3(0.5) &= \mathcal{F}_3(0.5).
\end{aligned} \tag{4.4.9}$$

From (4.4.9) we can compute the value of $\overline{\alpha}$ for equilibrium,

$$\overline{\alpha}^* = \frac{\mathcal{F}_3(0.5)\mathcal{R}_1(0.5)}{\mathcal{R}_3(0.5)} - \mathcal{F}_1(0.5). \tag{4.4.10}$$

In other words, for a given buoyancy α the Froude number yielding equilibrium is, at first order in Re, given by

$$\text{Fr}^*(\alpha) = \frac{\alpha}{\overline{\alpha}^*}. \tag{4.4.11}$$

In the following we shall present numerical results for the cases $\overline{\alpha} < \overline{\alpha}^*$, $\overline{\alpha} = \overline{\alpha}^*$ and $\overline{\alpha} > \overline{\alpha}^*$, at first order in Re and We, as well as at third order in Re.

Remark 4.10. Before presenting our numerical results, we would like to make two comments concerning the above computation of the equilibrium value $\overline{\alpha}^*$: Firstly, it is based on a *first-order* approximation of U_1 only. As a consequence, when we proceed to higher order we cannot expect the particle to stay at rest unless we also adjust $\overline{\alpha}^*$. Secondly, in the above computation we assume that the equilibrium distance from the wall is $h_{equi} = 0.5$, i.e. the channel center is a (stable) equilibrium. We will see that for $E = 0$ (purely Newtonian liquid) this is indeed the case provided the particle is heavy enough (at least at first order in Re). For a viscoelastic liquid ($E > 0$) however, this is not true in general. As we will see, elasticity acts to push the particle to the walls. Consequently, in such a case the choice of $\overline{\alpha} = \overline{\alpha}^*$ *does not guarantee* that the particle comes to rest, *even at first order* in Re and We!

Results at first order in Re and We

We recall, once more, from Section 4.2.3 that the equilibrium heights h_{equi} are given, at first order in Re and We, by the solutions to equation (4.2.26), that is,

$$\mathcal{G}(h; \overline{\alpha}) + E\mathcal{G}_V(h; \overline{\alpha}) = 0. \qquad (4.4.12)$$

The equilibrium value $\overline{\alpha}^*$ in (4.4.10) was found to be

$$\overline{\alpha}^* = 13.3591. \qquad (4.4.13)$$

First we will describe the results for the purely Newtonian case, $E = 0$. (These results are summarized in Table 4.3.) Equilibria are then characterized as zeros of the function $\mathcal{G}(\cdot; \overline{\alpha})$. In the following, we subsequently increase $\overline{\alpha}$. The results for $\overline{\alpha} = 0$ do not need to be discussed again since they are identical with the respective results for downward Poiseuille flow (see Section 4.4.1, Figure 4.3), the only difference being that the particle is now going up. The same two stable 'Segrè-Silberberg equilibria' $h_{equi}^{(1)} \approx 0.26$ and $h_{equi}^{(3)} \approx 0.74$ are found. The center equilibrium $h_{equi}^{(2)} = 0.5$ is unstable.

We now discuss the case $\overline{\alpha} > 0$. Figures 4.12, 4.13, 4.14, 4.15, 4.16 and 4.17 correspond to $\overline{\alpha} = 0.5$, $\overline{\alpha} = 1$, $\overline{\alpha} = 5$, $\overline{\alpha} = 10$, $\overline{\alpha} = \overline{\alpha}^*$ and $\overline{\alpha} = 15$, respectively. What we found is the following: The two stable equilibrium positions $h_{equi}^{(1)}$ and $h_{equi}^{(3)}$ both move towards the center as $\overline{\alpha}$ increases. Eventually, when $\overline{\alpha}$ reaches a critical value $\overline{\alpha}_c$, they will both collapse in the middle of the channel that will then become the only (stable) equilibrium. Note that $\overline{\alpha}_c$ is well below the equilibrium value $\overline{\alpha}^*$. Hence, in the parameter range $\overline{\alpha}_c < \overline{\alpha} < \overline{\alpha}^*$ the particle approaches the channel center and, eventually, goes up.

We come now to the case $\overline{\alpha} = \overline{\alpha}^*$, see Figure 4.16. All particle trajectories go to the channel center. There the particle comes to rest, as expected.

The case $\overline{\alpha} > \overline{\alpha}^*$ corresponds to a particle which is 'too heavy' to be balanced by the inflow. It falls down while approaching the center which is the only (stable) equilibrium.

Concerning the **viscoelastic case** ($E > 0$) we found the following, cf. Figures 4.12-4.17. For all values of $\overline{\alpha}$ in the considered parameter range, elasticity acts to *push the particle to*

Table 4.3: Number, position and stability of equilibrium positions for different values of $\overline{\alpha}$. The Poiseuille flow is directed upwards. The fluid is purely Newtonian ($E = 0$) and $\mathrm{Fr}\,\mathrm{Re} = 10$. Equilibria are computed at first order in Re.

$\overline{\alpha}$	
0	neutrally buoyant case; two stable equilibrium positions, symmetric with respect to the centerline ('Segrè-Silberberg effect'). The equilibrium in the middle of the channel is unstable.
0.5	The equilibrium positions are shifted towards the center line (Figure 4.12).
1	The center line is now the only (stable) equilibrium position (Figure 4.13).
10	When starting near the walls, the particle first go down a little bit while moving to the center line. Eventually, of course, it must go up, since still $\overline{\alpha} < \overline{\alpha}^*$ (Figure 4.15).
$\overline{\alpha}^*$	The equilibrium case: All trajectories go to the centerline. There the particle comes to rest (Figure 4.16).
15	The particle is too heavy. It falls down while approaching the center line (Figure 4.17).

the walls of the channel. Special attention deserves the case $\overline{\alpha} = \overline{\alpha}^*$, see Figure 4.16: For elasticity numbers E less than a certain critical elasticity number E_c, the trajectories still go to the center. For such a case, the analysis carried out above to determine $\overline{\alpha}^*$ is valid. Consequently, the particle comes to rest in the middle of the channel. However, if $E > E_c$, the center equilibrium becomes unstable. In this case, the particle approaches one of the two off-center equilibrium positions and goes down since the parabolic inflow is strong enough for fluidization only in the middle of the channel. The critical elasticity number was computed to $E_c = 0.0122$.
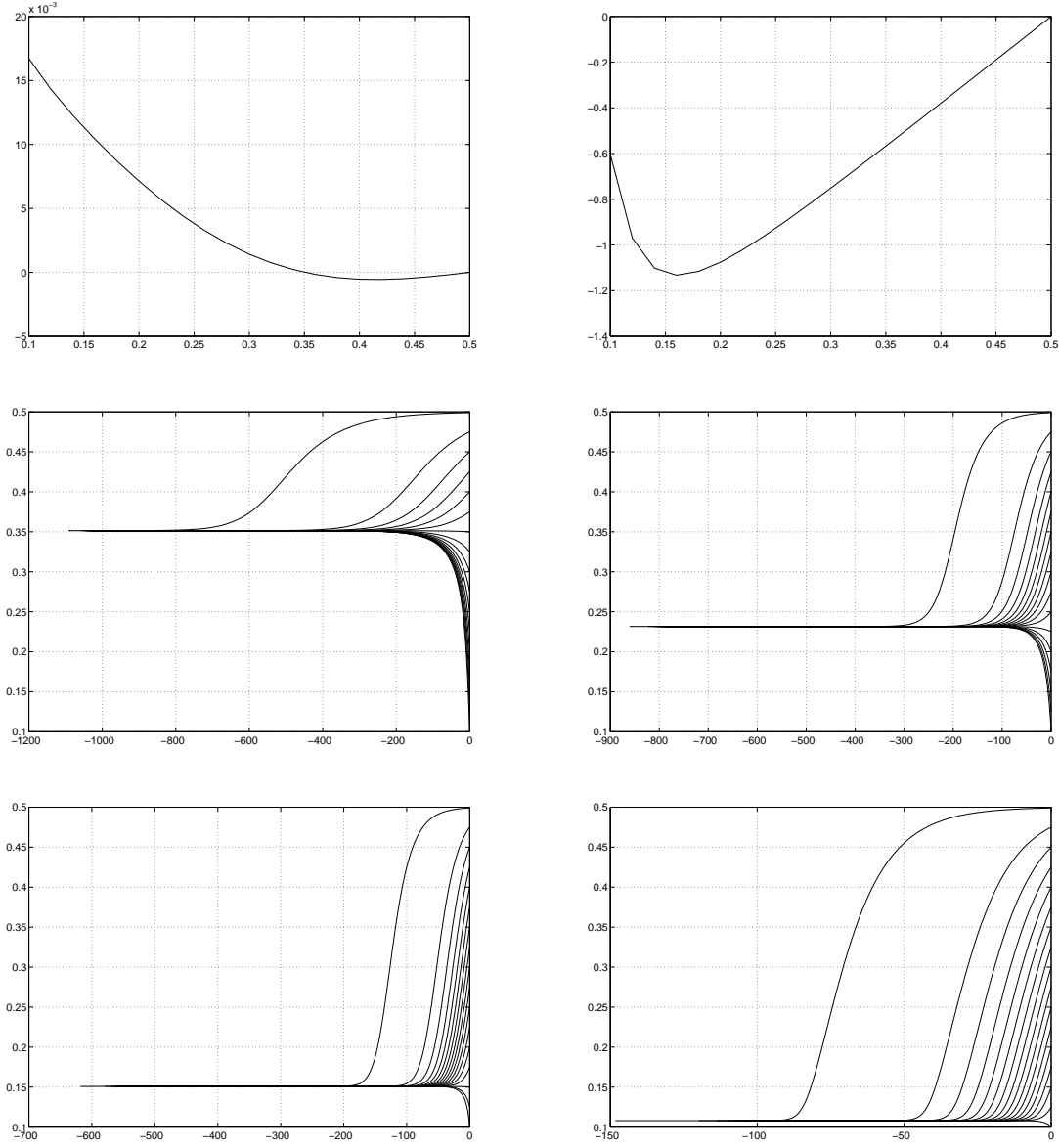
Figure 4.12: Results at first order in Re and We for the case of an upward Poiseuille flow, where $\overline{\alpha} = 0.5$ and $\mathrm{Fr}\,\mathrm{Re} = 10$. $\mathcal{G}(h)$ and $\mathcal{G}_V(h)$ vs. h (**first row**) and trajectories for $E = 0$, $E = 0.005$ (**second row**) and $E = 0.01, 0.02$ (**third row**).
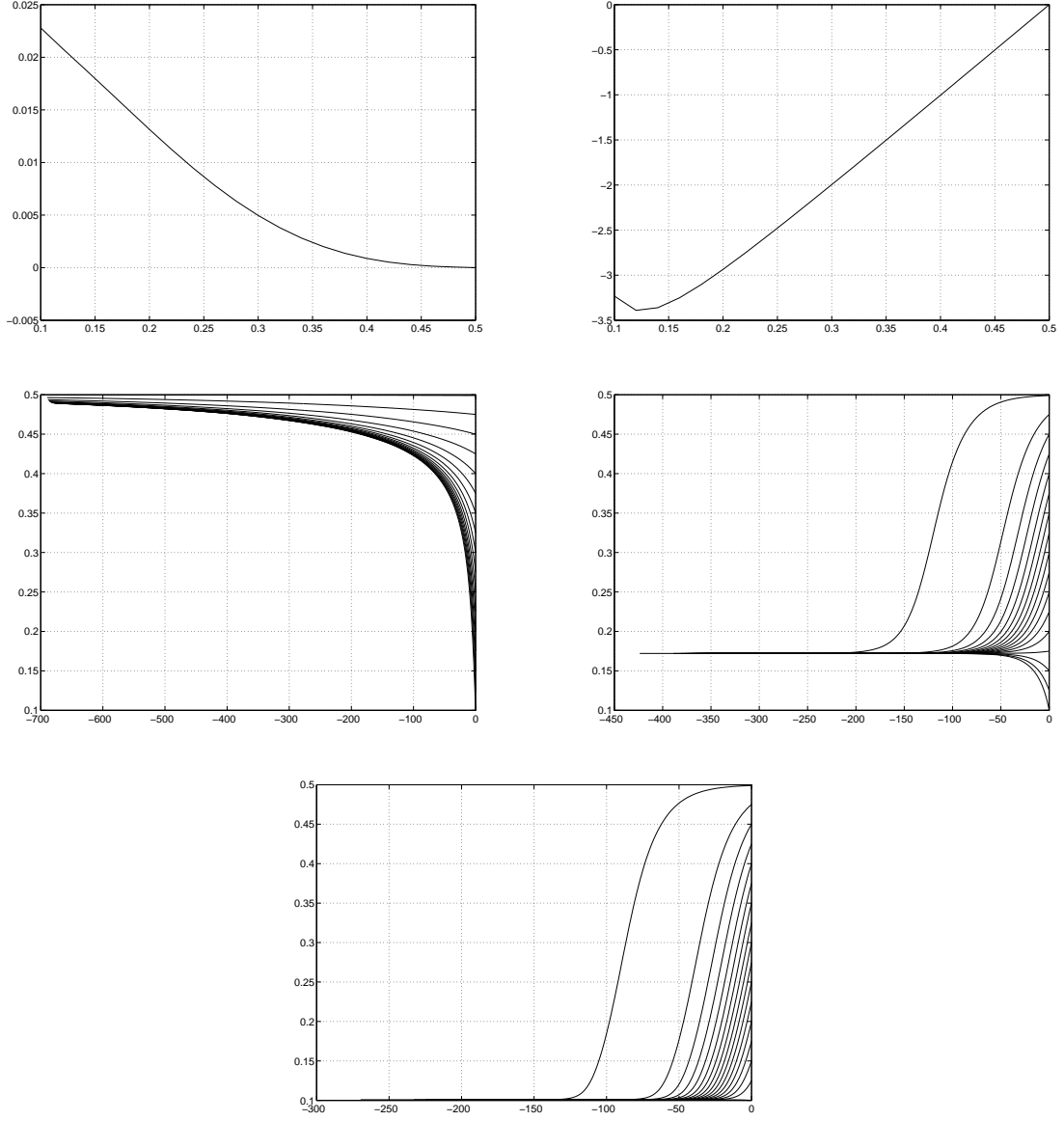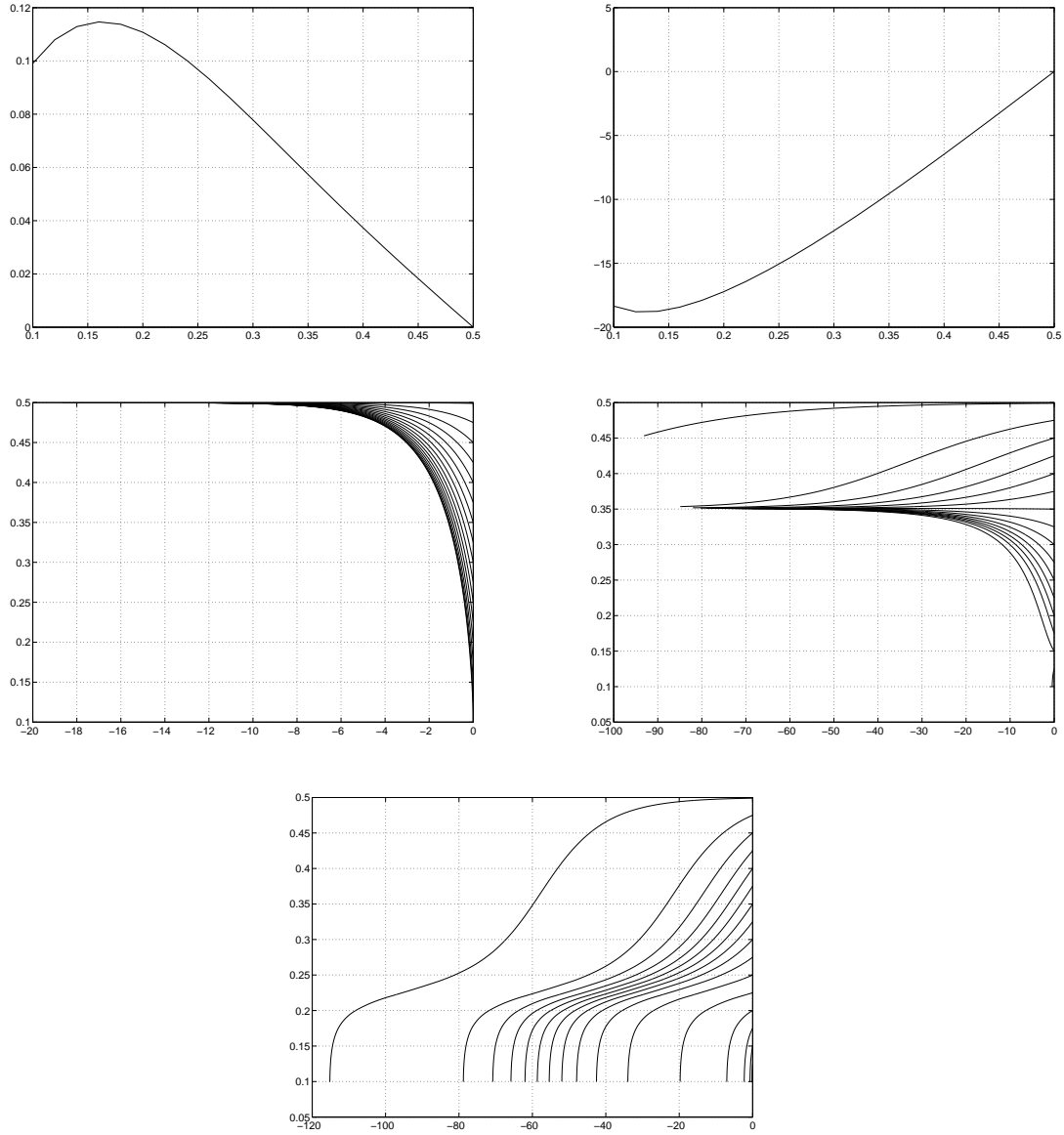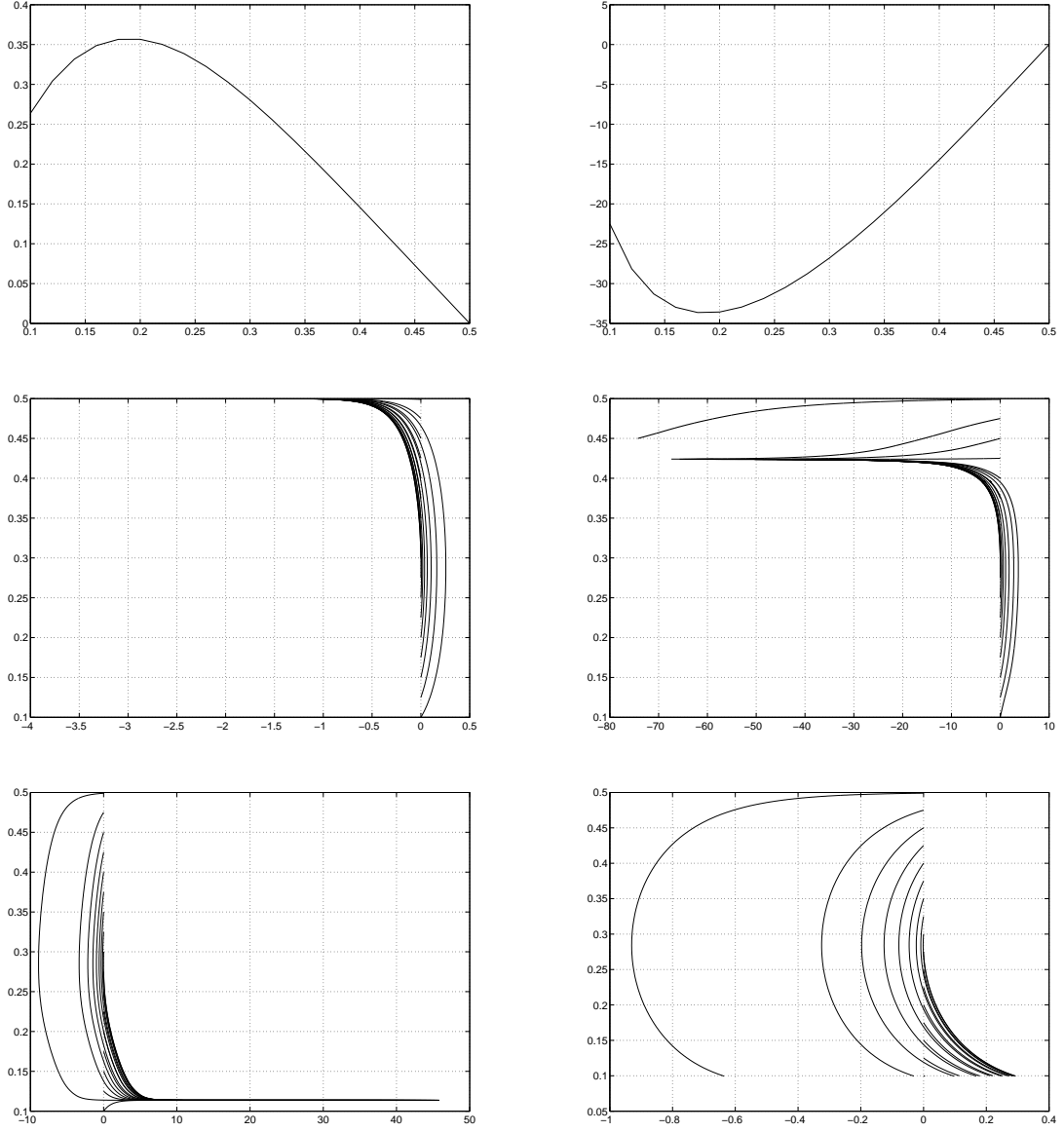
Figure 4.13: Results at first order in Re and We for the case of an upward Poiseuille flow, where $\overline{\alpha} = 1$ and $\mathrm{Fr}\,\mathrm{Re} = 10$. $\mathcal{G}(h)$ and $\mathcal{G}_V(h)$ vs. h (**first row**) and trajectories for $E = 0$, $E = 0.005$ (**second row**) and $E = 0.007$ (**third row**).
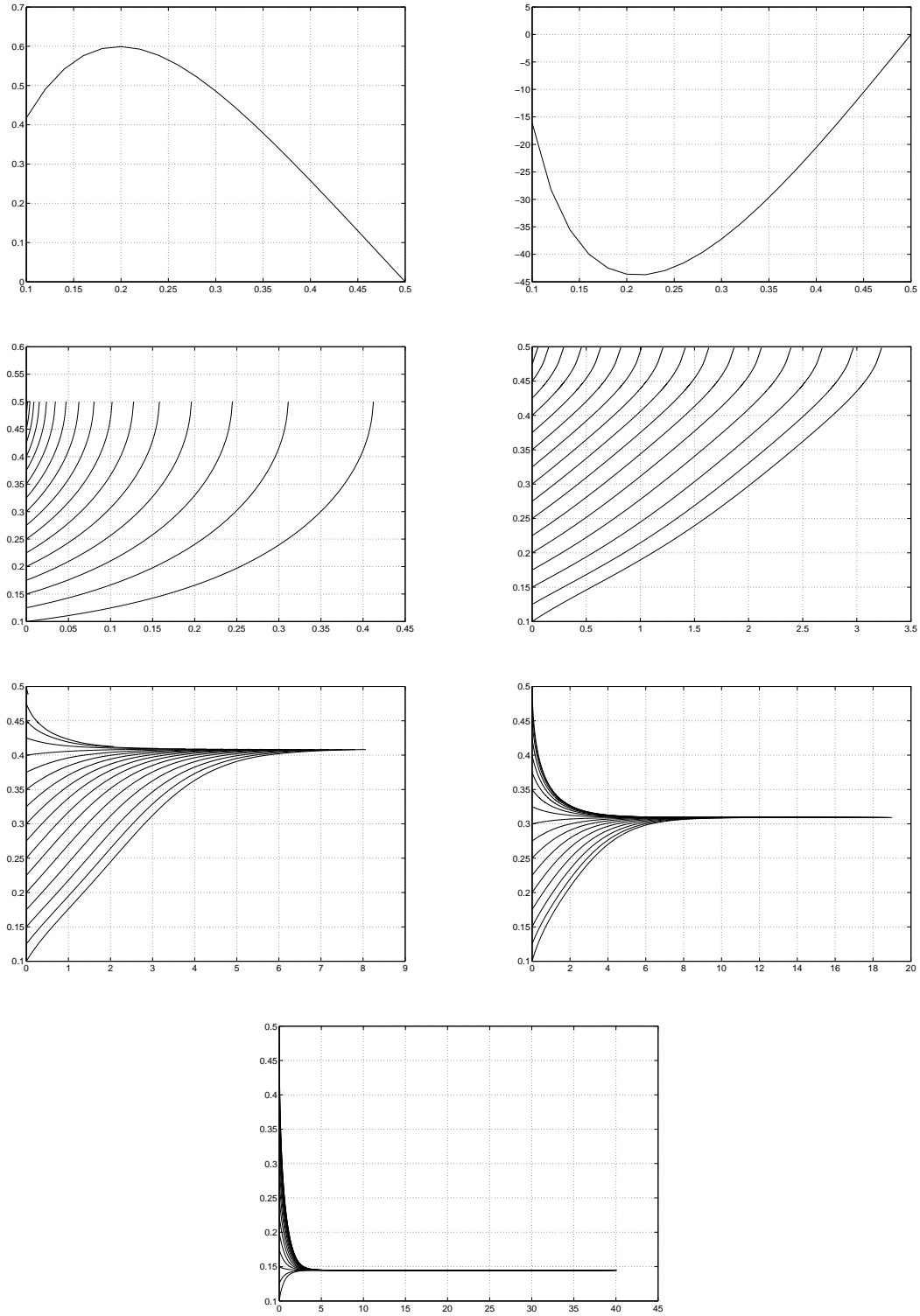
Figure 4.14: Results at first order in Re and We for the case of an upward Poiseuille flow, where $\overline{\alpha} = 5$ and $\mathrm{Fr}\,\mathrm{Re} = 10$. $\mathcal{G}(h)$ and $\mathcal{G}_V(h)$ vs. h (**first row**) and trajectories for $E = 0$, $E = 0.006$ (**second row**) and $E = 0.0065$ (**third row**).

Figure 4.15: Results at first order in Re and We for the case of an upward Poiseuille flow, where $\overline{\alpha} = 10$ and $\mathrm{Fr}\,\mathrm{Re} = 10$. $\mathcal{G}(h)$ and $\mathcal{G}_V(h)$ vs. h (**first row**) and trajectories for $E = 0$, $E = 0.01$ (**second row**) and $E = 0.011, 0.02$ (**third row**).

Figure 4.16: Results at first order in Re and We for the case of an upward Poiseuille flow, where $\overline{\alpha} = \overline{\alpha}^*$ and $\mathrm{Fr}\,\mathrm{Re} = 10$. $\mathcal{G}(h)$ and $\mathcal{G}_V(h)$ vs. h (**first row**) and trajectories for $E = 0$, $E = 0.012$ (**second row**), $E = 0.0125$, $E = 0.013$ (**third row**) and $E = 0.015$ (**fourth row**).
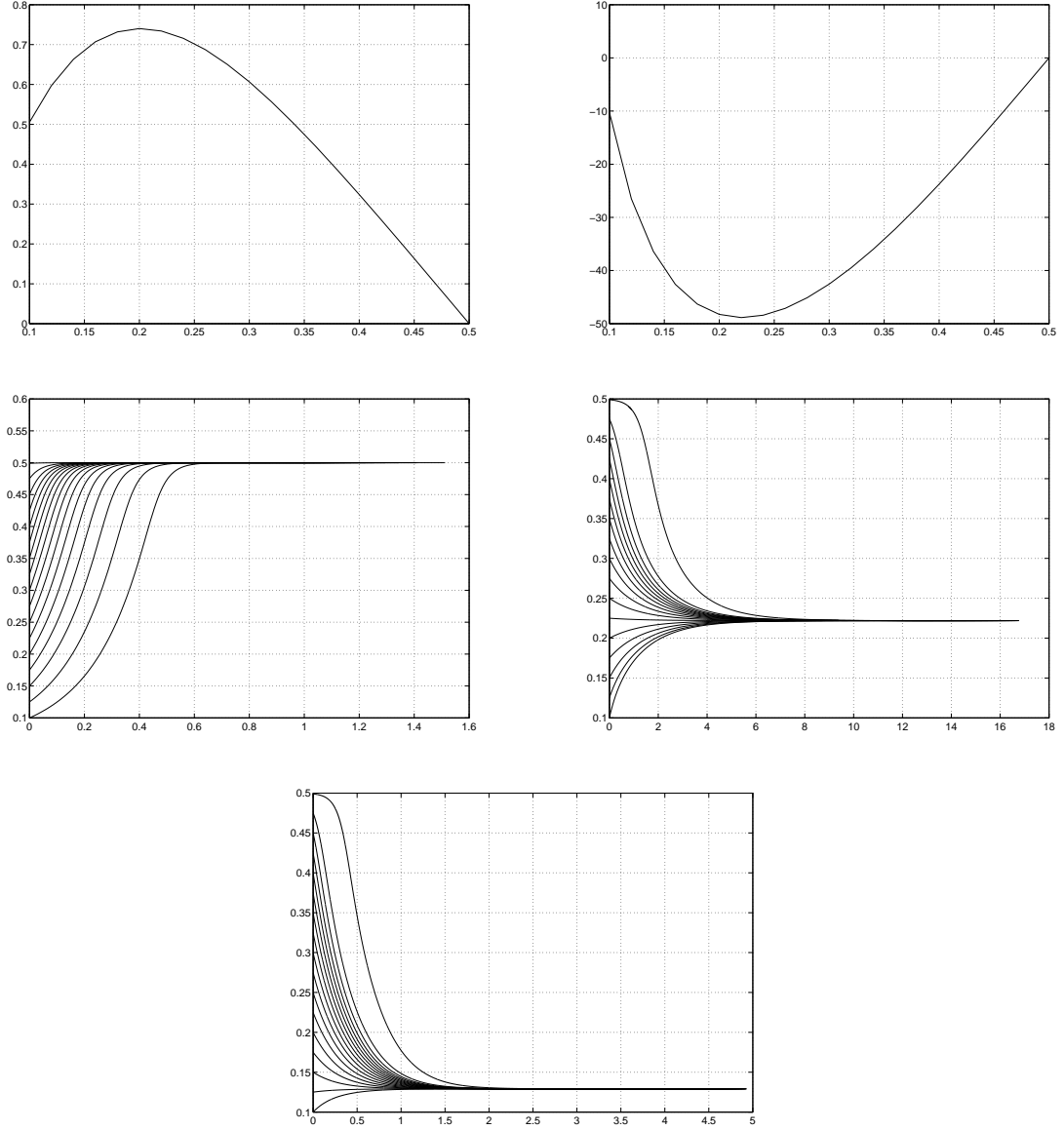
Figure 4.17: Results at first order in Re and We for the case of an upward Poiseuille flow, where $\overline{\alpha} = 15$ and $\mathrm{Fr}\,\mathrm{Re} = 10$. $\mathcal{G}(h)$ and $\mathcal{G}_V(h)$ vs. h (**first row**) and trajectories for $E = 0$, $E = 0.015$ (**second row**) and $E = 0.02$ (**third row**).

Results at third order in Re

The equilibrium heights h_{equi} are given, at third order in Re, by the solutions to

$$\text{Re}\, U_2^{(1)}(h) + \text{Re}^2 U_2^{(2)}(h) + \text{Re}^3 U_2^{(3)}(h) = 0.$$

Since $U_2^{(2)}(h) \equiv 0$ (see Remark 4.7) the equilibrium positions h_{equi} are again characterized as solutions to the equation

$$\tilde{U}_2(h) = \text{Fr}\,\text{Re}\overline{U}_2^{(1)} + (\text{Fr}\,\text{Re})^3 \overline{U}_2^{(3)} = 0. \tag{4.4.14}$$

In Figures 4.19–4.24 we present numerical results for $\overline{\alpha} \in \{0.5, 1, 5, 10, \overline{\alpha}^*, 15\}$. As in Section 4.4.1 (downward flow), we plot the following characteristic quantities for each value of $\overline{\alpha}$:

- the first and third-order contributions $\mathcal{G}^{(1)}$ and $\mathcal{G}^{(3)}$ to the lift (see (4.4.7)),

- $\tilde{U}_2$ as in (4.4.8), for different values of $\text{Fr}\,\text{Re}$,

- the particle 'trajectories' $\{(x_1(t), x_2(t)),\ t \geq 0\}$ computed according to (4.4.5), for different values of $\text{Fr}\,\text{Re}$.

The results for $\overline{\alpha} = 0$ do not need to be discussed again since they are identical with the respective results for downward Poiseuille flow (see Section 4.4.1, Figure 4.8), the only difference being that the particle is now going up instead of going down. In particular, the number and stability of equilibrium positions are the same. They are summarized in Table 4.4.

Concerning $\overline{\alpha} > 0$ the following information can be extracted from the simulations (see Figures 4.19–4.24 and Table 4.4): For small values of $\text{Fr}\,\text{Re}$, first-order effects are dominant and hence the particle will go to the center, provided $\overline{\alpha} > \overline{\alpha}_c$ (see above). For $\overline{\alpha}$ *and* $\text{Fr}\,\text{Re}$ both large enough, the particle will always go *to the walls*. For intermediate values of $\overline{\alpha}$ and/or $\text{Fr}\,\text{Re}$, however, the particle trajectories show a rather complex transient structure; small variations in the parameters can lead to dramatic changes of the global particle behavior. As an example, we consider the case $\overline{\alpha} = \overline{\alpha}^*$, where $\overline{\alpha}^*$ is the value of $\overline{\alpha}$ introduced in (4.4.10),(4.4.13) in order to stabilize the particle *at first-order* in Re. Figure 4.18 shows the trajectories corresponding to $\text{Fr}\,\text{Re} = 5$, $\text{Fr}\,\text{Re} = 7$ and $\text{Fr}\,\text{Re} = 10$, respectively. (The plots are identical with the corresponding ones contained in Figure 4.23, but we repeat them here for the readers' convenience). As expected, the 'first-order equilibrium value' $\overline{\alpha} = \overline{\alpha}^*$ is not appropriate in order to stabilize the particle at third order (see also Remark 4.10). For $\text{Fr}\,\text{Re} = 5$ the trajectories still go to the centerline, but the particle does not come to rest there but goes up instead. In contrast, for $\text{Fr}\,\text{Re} = 10$ the particle first goes up for most initial positions and approaches an off-center equilibrium position near the channel wall. There it falls down. Finally, for $\text{Fr}\,\text{Re} = 7$, a 'mixture' of the two aforementioned results is observed: The half-channel $\{h \leq 0.5\}$ is divided in two sections by an unstable equilibrium at $h_0 \approx 0.28$. A particle starting in the lower section ($h < h_0$) eventually will fall down while approaching a stable equilibrium at $h \approx 0.18$. In contrast, a particle released in the upper section ($h > h_0$) approaches the channel centerline while rising. We can conclude that at higher order much more intricate trajectory patterns emerge than at first order.

Table 4.4: Number and stability of equilibrium positions. The upper table refers to $\overline{\alpha} = 0$ (**left**), $\overline{\alpha} = 0.5$ (**middle**) and $\overline{\alpha} = 1$ (**right**). The lower table refers to $\overline{\alpha} = 5$ (**left**), $\overline{\alpha} = 10$ (**middle**) and $\overline{\alpha} = \overline{\alpha}^*$ (**right**). The Poiseuille flow is directed upwards. The fluid is purely Newtonian ($E = 0$) and equilibria are computed at third order in Re.

	$\overline{\alpha} = 0$			$\overline{\alpha} = 0.5$		$\overline{\alpha} = 1$	
Fr Re	10	30	70	10	30	10	30
#equilibria	3	5	3	3	3	1	3
#stable eq.	2	2	1	2	1	1	1
center stable	no	no	yes	no	yes	yes	yes

	$\overline{\alpha} = 5$			$\overline{\alpha} = 10$			$\overline{\alpha} = \overline{\alpha}^*$		
Fr Re	10	20	30	5	10	20	4	8	12
#equilibria	1	3	1	1	5	1	1	5	1
#stable eq.	1	1	0	1	3	0	1	3	0
center stable	yes	yes	no	yes	yes	no	yes	yes	no
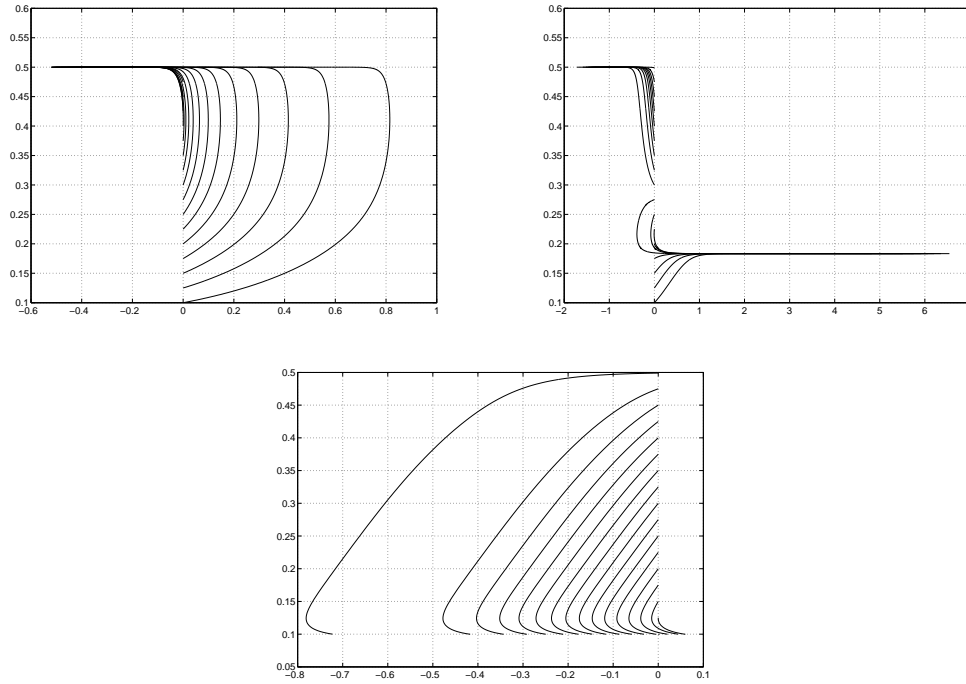
Figure 4.18: Results at third order in Re for the case of an upward Poiseuille flow, $\overline{\alpha} = \overline{\alpha}^*$. The particle trajectories are plotted for $\mathrm{Fr}\,\mathrm{Re} = 5$ (**top left**), $\mathrm{Fr}\,\mathrm{Re} = 7$ (**top right**), and $\mathrm{Fr}\,\mathrm{Re} = 10$ (**bottom**).
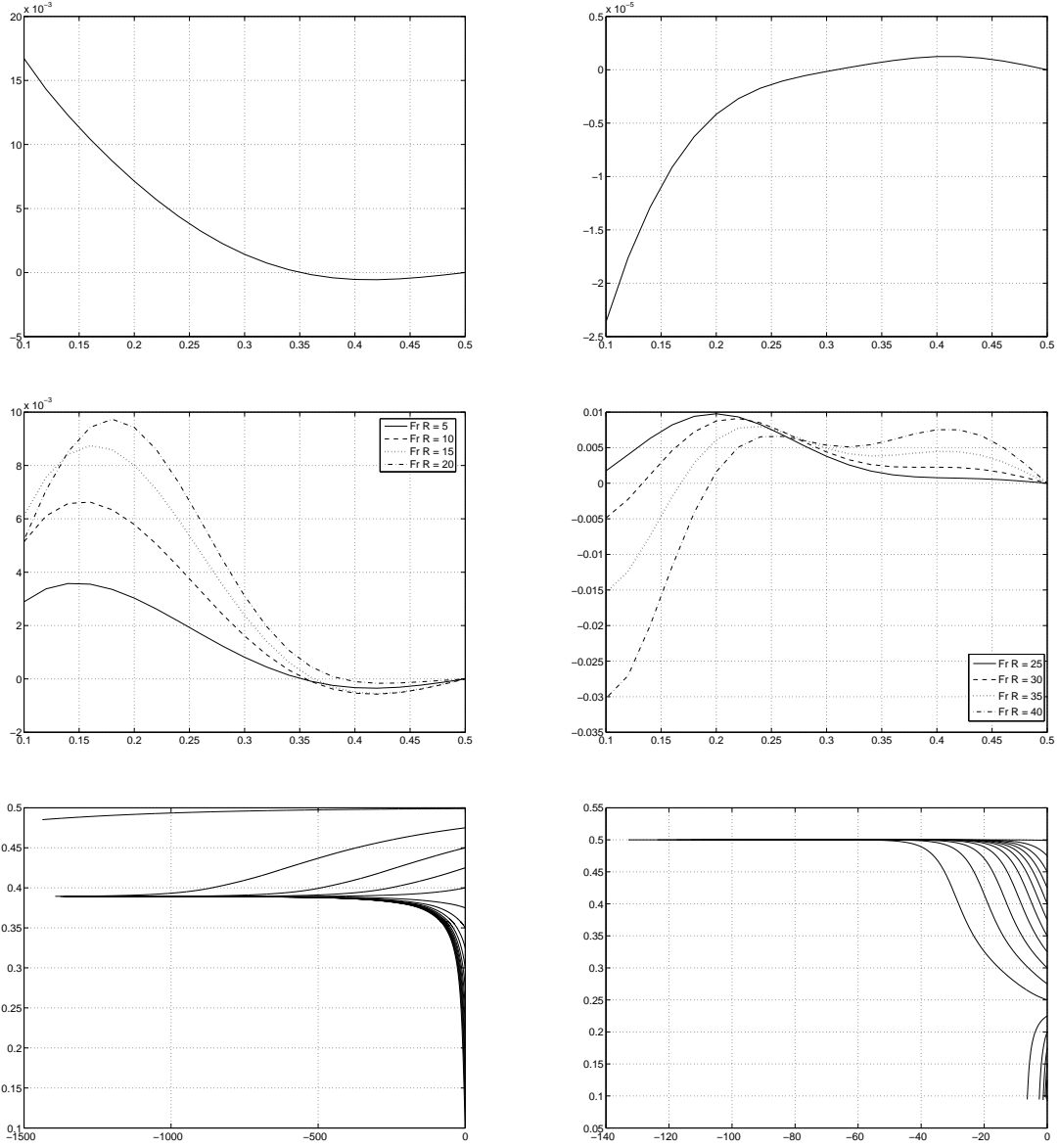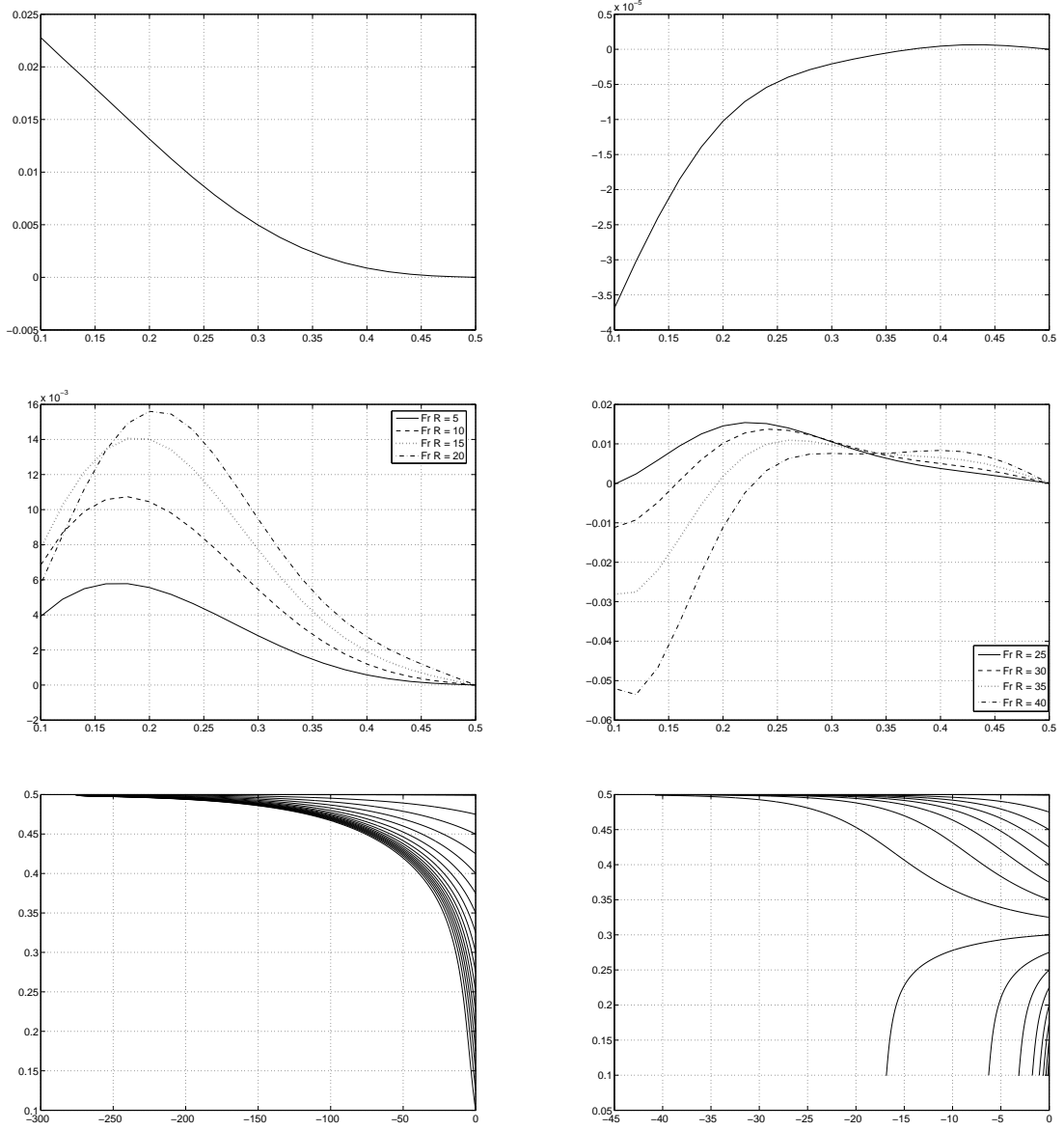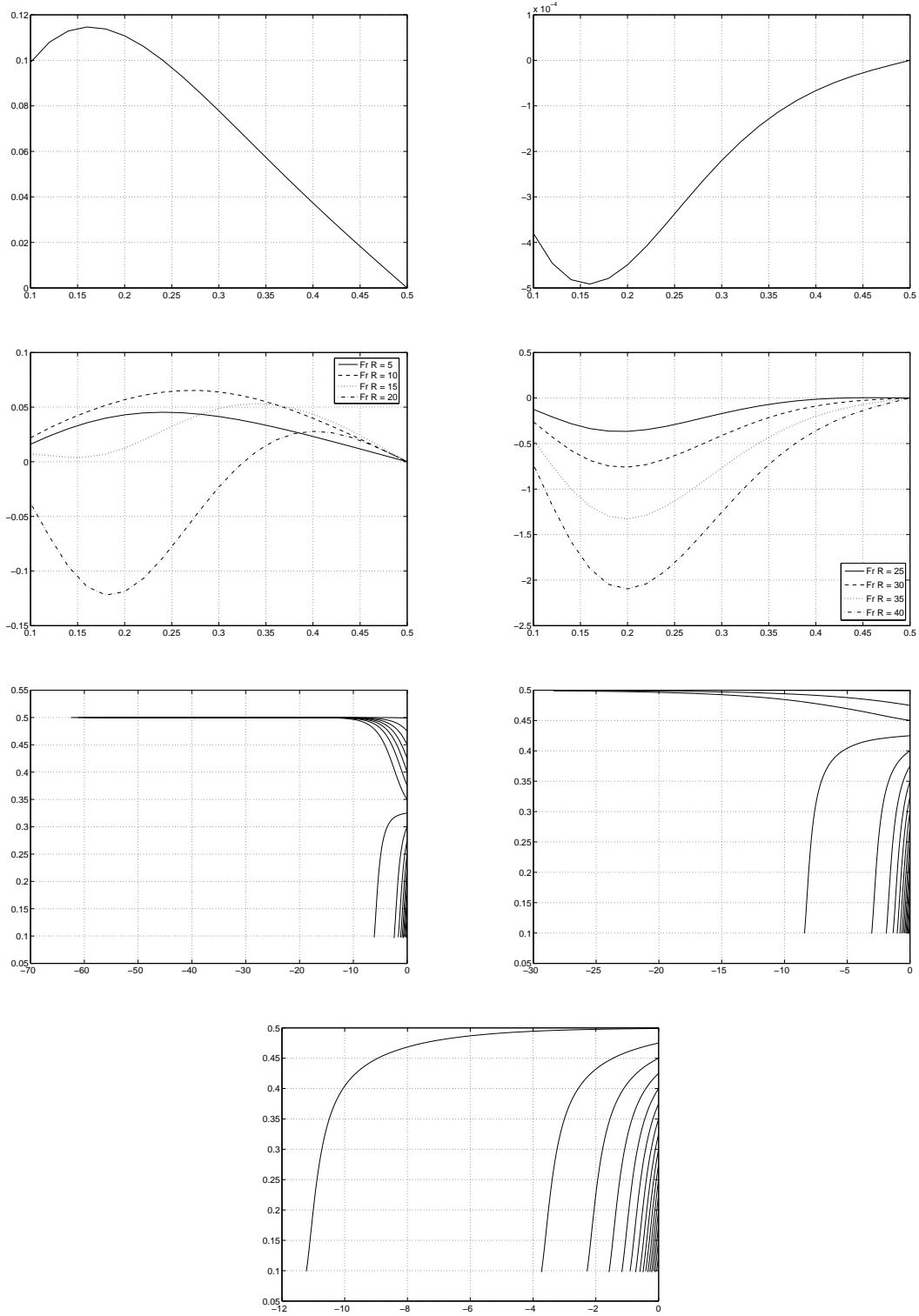
Figure 4.19: Results at third order in Re for the case of an upward Poiseuille flow, $\overline{\alpha} = 0.5$. $\mathcal{G}^{(1)}(h)$ and $\mathcal{G}^{(3)}(h)$ vs. h (**first row**), $\tilde{U}_2$ vs. h for different values of $\mathrm{Fr}\,\mathrm{Re}$ (**second row**), and trajectories for $\mathrm{Fr}\,\mathrm{Re} \in \{20, 50\}$ (**third row**).
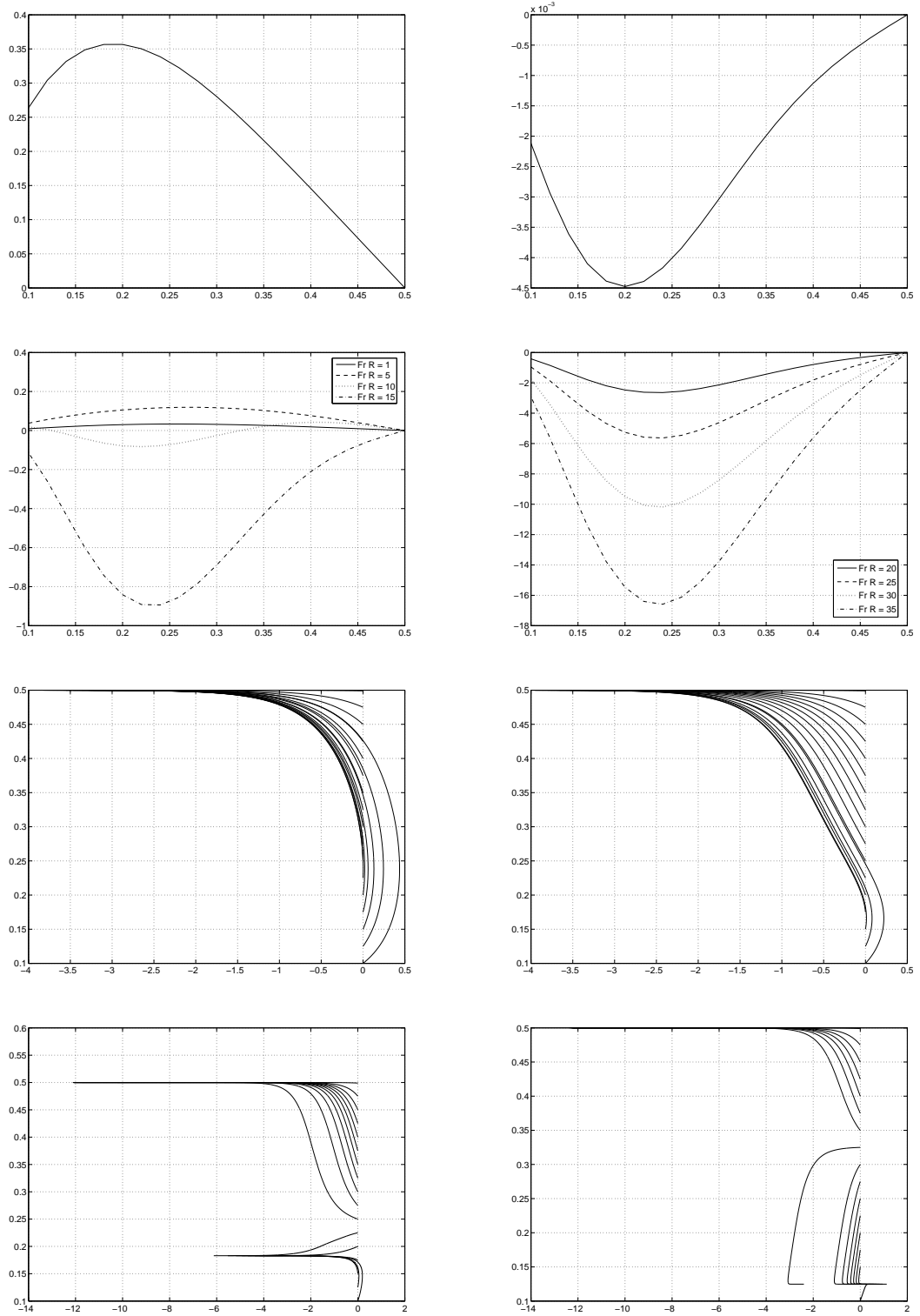
Figure 4.20: Results at third order in Re for the case of an upward Poiseuille flow, $\overline{\alpha} = 1$. $\mathcal{G}^{(1)}(h)$ and $\mathcal{G}^{(3)}(h)$ vs. h (**first row**), $\tilde{U}_2$ vs. h for different values of $\mathrm{Fr}\,\mathrm{Re}$ (**second row**), and trajectories for $\mathrm{Fr}\,\mathrm{Re} \in \{20, 50\}$ (**third row**).
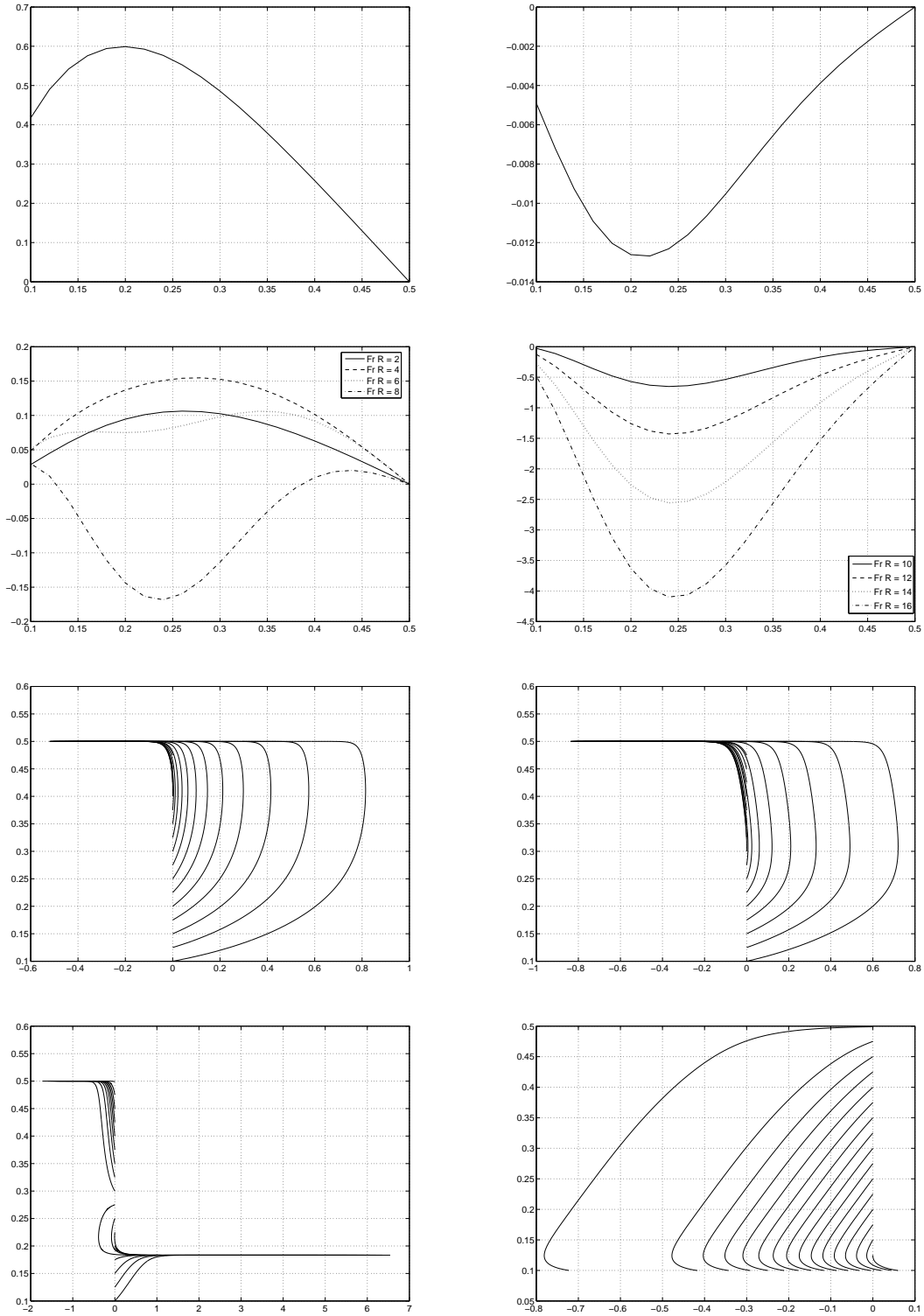
Figure 4.21: Results at third order in Re for the case of an upward Poiseuille flow, $\overline{\alpha} = 5$. $\mathcal{G}^{(1)}(h)$ and $\mathcal{G}^{(3)}(h)$ vs. h (**first row**), $\tilde{U}_2$ vs. h for different values of Fr Re (**second row**), and trajectories for Fr Re $\in \{20, 25, 30\}$ (**third & fourth row**).

Figure 4.22: Results at third order in Re for the case of an upward Poiseuille flow, $\overline{\alpha} = 10$. $\mathcal{G}^{(1)}(h)$ and $\mathcal{G}^{(3)}(h)$ vs. h (**first row**), $\tilde{U}_2$ vs. h for different values of $\mathrm{Fr}\,\mathrm{Re}$ (**second row**), and trajectories for $\mathrm{Fr}\,\mathrm{Re} \in \{5, 8, 9, 10\}$ (**third & fourth row**).

Figure 4.23: Results at third order in Re for the case of an upward Poiseuille flow, $\overline{\alpha} = \overline{\alpha}^*$. $\mathcal{G}^{(1)}(h)$ and $\mathcal{G}^{(3)}(h)$ vs. h (**first row**), $\tilde{U}_2$ vs. h for different values of Fr Re (**second row**), and trajectories for Fr Re $\in \{5, 6, 7, 10\}$ (**third & fourth row**).
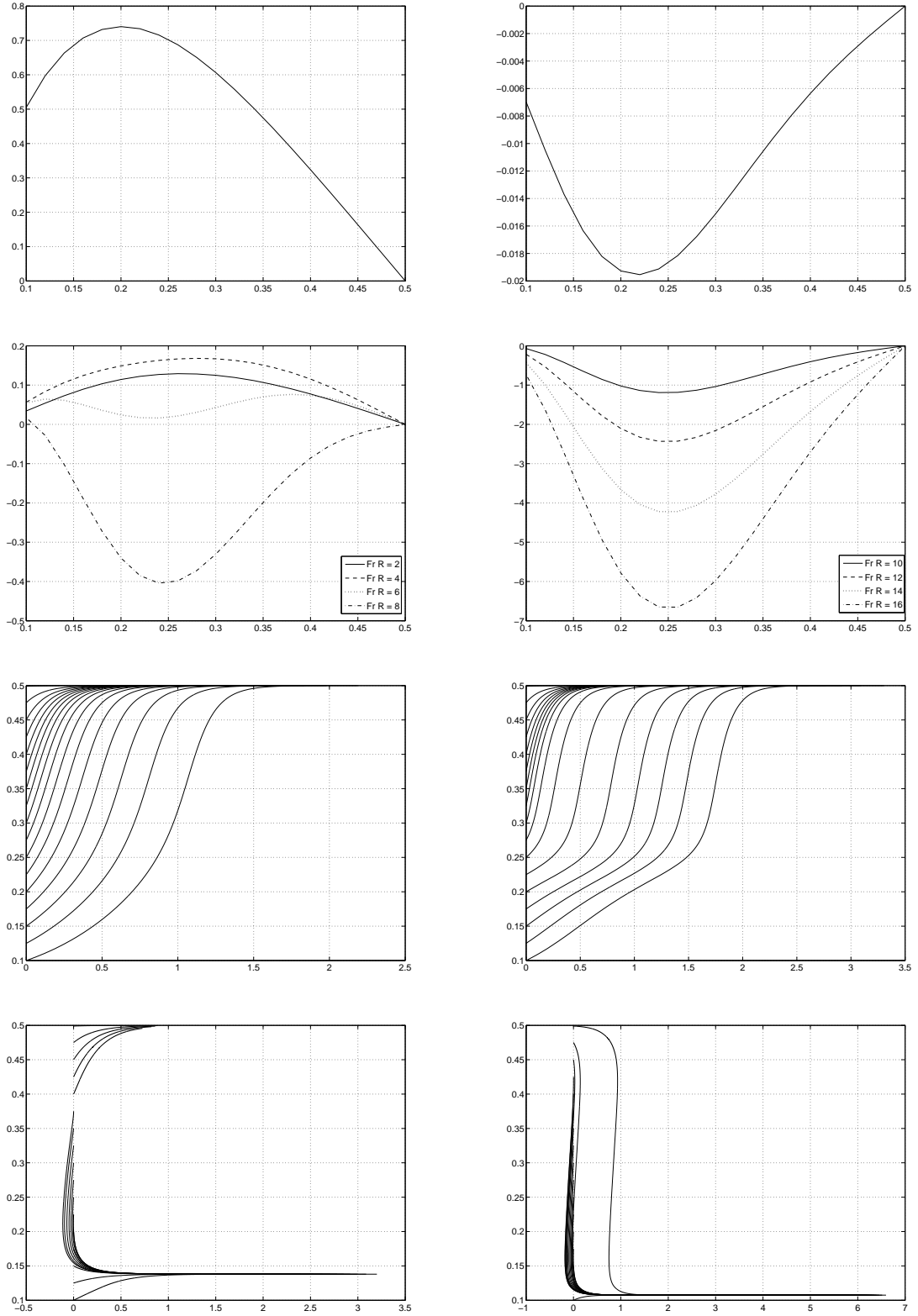
Figure 4.24: Results at third order in Re for the case of an upward Poiseuille flow, $\overline{\alpha} = 15$. $\mathcal{G}^{(1)}(h)$ and $\mathcal{G}^{(3)}(h)$ vs. h (**first row**), $\tilde{U}_2$ vs. h for different values of Fr Re (**second row**), and trajectories for Fr Re $\in \{5, 6, 7, 8\}$ (**third & fourth row**).

5 Motion of multiple particles

We now turn to the general case and discuss possibilities to simulate the motion of an arbitrary number of rigid particles in a fluid filling a domain with arbitrary geometry. Unlike in the special cases considered in the previous chapters, there is no possibility any more to get rid of the time-dependence of the fluid domain by means of a simple frame transformation. Moreover, since the particles are advected by the fluid and exert forces on the fluid, the need for an accurate resolution of the body-liquid interfaces gives further complexity to the problem with increasing number of particles. This makes Direct Numerical Simulation (DNS) of the general particulate flow problem a very challenging task.

This chapter is organized as follows: In Section 5.1 we give an overview of the different numerical methods proposed for this problem during the past years. In Section 5.2 we present an adaptive fictitious-domain method to simulate rigid particulate flow problems. Our algorithm is based on the stress-DLM approach originally proposed by Patankar et al. [PSJ⁺00]. However, the consequent use of *adaptivity* (adapted meshes, selective quadrature) makes our method much more accurate and efficient, see also Bönisch et al. [BDR06, Boe06]. In Section 5.3 we present numerical experiments. We validate our method by solving a well-known benchmark problem. The savings achieved by adaptivity are huge. The simulation of different configurations involving multiple particles show the potential of our approach. The issue of non-smooth particle geometries is addressed.

5.1 Overview of existing numerical approaches

There are essentially two conceptually distinct approaches which have been developed for DNS of particulate flow problems, see e.g. Wan/Turek [WT06] and Patankar et al. [PSJ⁺00].

The first approach is based on the arbitrary-Lagrangian-Eulerian (ALE) idea and was introduced by Hu and coworkers [Hu96, HJC92, HPZ01]. They use a combined weak fluid-particle formulation, where the mutual hydrodynamic forces acting on the particles and on the fluid cancel out. For the computations an unstructured, body-fitted moving mesh is employed and the arbitrary-Lagrangian-Eulerian technique is adopted to deal with the motion of the particles. The mesh points located on the particle boundary move with the particle, while the mesh points associated to the fluid domain are computed using Laplace's equation in order to guarantee a smoothly varying node distribution. At each time step, the mesh is updated according to the motion of the particles. Care has to be taken of possible degeneration of mesh cells. If the mesh distortion becomes too large, a new finite element grid is generated and the flow field is projected from the old grid to the new one. In this scheme, the positions of the particles and grid nodes are updated explicitly, while the velocities of the

fluid and the solid particles are determined implicitly. Another numerical scheme based on the moving-mesh technique was developed by Johnson and Tezduyar [JT96]. These authors used a space-time finite element formulation and a fully explicit scheme in which the forces acting on the particles were calculated explicitly in order to solve Newton's equations of motion for the rigid particles.

The second approach is 'Eulerian' and is based on the principle of embedded or 'fictitious' domains. The idea is to embed an irregular computational domain into a larger domain of simpler shape and to discretize this simple, 'fictitious' domain. The presence of the 'real' boundaries is then simulated by adding appropriate forcing terms to the equation to be solved. In the context of particulate flows this means that the fluid flow is computed *as if the space occupied by the particles were filled with fluid*, too. The no-slip boundary condition on the particle boundaries is then enforced by an extra constraint. This allows for the use of a fixed grid, eliminating the need for re-meshing which is a definite advantage especially in parallel implementations. There are several ways to apply this general principle to solve fluid-particle interaction problems. Glowinski et al. [GPH+01] proposed a distributed Lagrange-multiplier/fictitious-domain (DLM) method for the direct numerical simulation of the motion of many rigid particles in Newtonian fluids. Their formulation permits the use of a fixed structured grid which allows for the use of fast and efficient solvers. In the DLM method, the flow in the particle domain is restricted to rigid-body motions by employing a rigidity constraint giving rise to a Lagrange multiplier field in the particle domain. The fluid-particle motion is treated implicitly using a combined weak formulation in which the mutual forces cancel. A variant of the DLM approach for particulate flow simulations was later presented by Patankar et al. [PSJ+00] and is known as the 'stress-DLM formulation'. The idea is to impose the rigid motion by constraining the deformation-rate tensor within the particle domain to zero. This eliminates the translational and angular velocities of the particles as variables from the coupled system of equations. The stress-DLM formulation recognizes that the rigidity constraint results in a stress field inside a rigid solid just as there is a pressure in an incompressible fluid. The DLM variants of Glowinski et al. [GPH+01] and Patankar et al. [PSJ+00] were both implemented by using a Marchuk-Yanenko operator-splitting scheme for time discretization and a finite element spatial discretization. Although the DLM methodology has been successfully used for computations with up to 1204 spheres in three dimensions, see Pan et al. [PJB+02], further speed-up of the solution procedure was desirable. Therefore, Patankar [Pat01, SP05] presented an adapted version of his earlier DLM-based formulation for the fast computation of rigid particulate flows. The key issue addressed in this DLM variant is the fast implementation of the rigidity constraint. The formulation eliminates the need for an iterative procedure to solve the rigid body projection step thereby allowing for faster computations.

Recently, a more 'explicit' variant of the fictitious-domain method, the so-called 'fictitious-boundary' method, has been introduced by Turek et al. [TWR03, WT06], see also Duchanoy and Jongen [DJ03]. In contrast to the classical, 'implicit' fictitious-domain approach, the fictitious-boundary method solves the fluid equations and the solid equations separately. The forces exerted on the particles are calculated in an efficient way by means of an explicit volume formula. Turek et al. [TWR03] proposed a multigrid-FEM-based explicit fictitious boundary method which is based on an unstructured FEM background grid. The flow is computed using a multigrid finite element method and the solid particles are allowed to move

freely through the computational mesh which can be chosen independently of the particles. The motion of the solid particles is represented by prescribing the respective velocities at the nodes covered by the particles. The new positions and the new velocities of the particles are updated using Newton's law so that there is no need to re-mesh the domain.

Recent computational approaches to solid-liquid flows, possibly inspired by molecular dynamics, are based on the lattice-Boltzmann method (LBM), see Ladd [Lad94a, Lad94b, LV01]. In LBM, simplified kinetic models are constructed which incorporate the essential physics of the microscopic and mesoscopic equations. These models can handle huge numbers of particles. One should keep in mind, however, that they replace the well-justified hydrodynamic equations of motion by pointwise collision rules. Therefore, many interesting results obtained using these methods are not yet sufficiently reliable to be used in engineering practice.

5.2 An adaptive fictitious-domain method

In this section we present a numerical scheme for rigid particulate flows which can be seen, to some extent, as a combination of Eulerian and Lagrangian methods: On one hand, we borrow from Eulerian methods the idea of solving the fluid equations on a fixed, simple-shaped 'fictitious' domain. On the other hand, we let the mesh refinement follow the particle boundaries. This seems to be a new aspect in particulate flow simulations. The resulting method is highly accurate and, at the same time, very economic (see also Bönisch et al. [BDR06, Boe06]).

Our method is based on the so-called 'stress-DLM formulation' introduced by Patankar et al. [PSJ$^+$00] which we are going to describe first.

5.2.1 The stress-DLM formulation

Let Ω be the (bounded) computational domain which includes both the fluid and the particle domain and let $S = S(t)$ be the particle domain. In order to facilitate notations, we assume that there is only one moving particle in a Newtonian fluid. The formulation can be easily generalized beyond these assumptions.

The governing equations for fluid motion are given by:

$$
\begin{aligned}
\rho_f \left(\partial_t v + (v \cdot \nabla) v \right) + \nabla p - \mu \Delta v = \rho_f g, & \quad \text{in } \Omega \setminus \overline{S(t)}, \\
\nabla \cdot v = 0 & \quad \text{in } \Omega \setminus \overline{S(t)}, \\
v = v^\partial(t) \quad \text{on } \partial\Omega(t), \quad v = v^i & \quad \text{on } \partial S(t), \\
v_{|t=0} = v^0 & \quad \text{in } \Omega \setminus \overline{S(0)},
\end{aligned}
\tag{5.2.1}
$$

where ρ_f is the fluid density, $U = \{v, p\}$ is the fluid velocity and pressure pair, v^i is the velocity of the fluid-particle interface $\partial S(t)$, and v^0 is the initial velocity. In the stress-DLM formulation the particles are treated as a fluid with an additional constraint to impose the rigidity. Accordingly, the governing equations for particle motion are:

$$\rho_s \left(\partial_t v + (v \cdot \nabla) v \right) + \nabla p - \mu \Delta v = \rho_s g \quad \text{in } S(t),$$
$$\nabla \cdot v = 0 \quad \text{in } S(t),$$
$$\nabla \cdot D(v) = 0 \quad \text{in } S(t), \quad n \cdot D(v) = 0 \quad \text{on } \partial S(t), \qquad (5.2.2)$$
$$v = v^i \quad \text{on } \partial S(t),$$
$$v_{|t=0} = v^0 \quad \text{in } S(0),$$

where ρ_s is the particle density. The third equation in (5.2.2) represents the rigidity constraint that sets the deformation tensor, $D(v) := (\nabla v + \nabla v^T)/2$, in the particle domain equal to zero. Then, a combined weak formulation of the fluid-particle equations (5.2.1-5.2.2) can be derived by introducing a *distributed Lagrange multiplier* (DLM) Λ. Variational analysis shows (see e.g. Sharma/Patankar [SP05]) that $D(\Lambda)$ can be interpreted as an extra-stress field required inside the particle domain to maintain the rigid-body motion. With the spaces

$$V_0 := H_0^1(\Omega)^2, \quad L_0 := \{ q \in L^2(\Omega), \, (q,1)_\Omega = 0 \},$$

the combined weak formulation of (5.2.1) and (5.2.2) reads as follows:

Problem 5.1. For $t > 0$, find $v \in v^\partial + V_0$, $p \in L_0$, $\Lambda \in H^1(S(t))^2$ satisfying

$$\begin{aligned}
\left(\rho_f(\partial_t v + (v \cdot \nabla)v - g), \varphi \right)_\Omega - (p, \nabla \cdot \varphi)_\Omega &+ (\chi, \nabla \cdot v)_\Omega + \mu(\nabla v, \nabla \varphi)_\Omega \\
&+ \left((\rho_s - \rho_f)(\partial_t v + (v \cdot \nabla)v - g), \varphi \right)_{S(t)} \qquad (5.2.3) \\
&+ \left(D(\Lambda), D(\varphi) \right)_{S(t)} + \left(D(\psi), D(v) \right)_{S(t)} = 0,
\end{aligned}$$

for all $\varphi \in V_0, \chi \in L_0(\Omega), \psi \in H^1(S(t))^2$.

Remark 5.2. The fluid-particle interface condition is internal to the combined system (5.2.3). Hence there are no explicit interface force or velocity terms in the combined form. We also note that the particle translational and angular velocities are not present unlike in the original DLM formulation of Glowinski et al. [GPH$^+$01].

5.2.2 Numerical scheme

Patankar et al. [Pat01, SP05] proposed a fast projection scheme to solve (5.2.3) without the need for an additional saddle-point iteration to determine the Lagrange multiplier Λ. For the reader's convenience we shall briefly recall this scheme. Further details concerning the solution of the individual substeps and the incorporation of adaptivity are presented in Section 5.2.3.

The starting point is the strong formulation of (5.2.3). The momentum and continuity equations applicable in the entire domain can be written as:

$$\rho(\partial_t v + (v \cdot \nabla)v) + \nabla p - \mu \Delta v = \rho g + f \quad \text{in} \quad \Omega,$$
$$\nabla \cdot v = 0 \quad \text{in} \quad \Omega, \qquad (5.2.4)$$

where

$$\rho = \rho(x) = \begin{cases} \rho_f & \text{in} \quad \Omega \backslash \overline{S(t)}, \\ \rho_s & \text{in} \quad S(t), \end{cases} \qquad (5.2.5)$$

and f is the additional term due to the rigidity constraint in the particle domain. More specifically, $f = \nabla \cdot D(\Lambda)$.

The fast projection scheme for solving (5.2.4) now consists of two fractional steps:

(I) Determine intermediate velocity and pressure fields $\hat{v}$ and $\hat{p}$ by solving the following equations in the entire domain Ω:

$$\rho \left(\tfrac{\hat{v}-v^n}{\Delta t} + (\hat{v} \cdot \nabla)\hat{v} \right) + \nabla \hat{p} - \mu \Delta \hat{v} = \rho g \quad \text{in} \quad \Omega,$$
$$\nabla \cdot \hat{v} = 0 \quad \text{in} \quad \Omega. \tag{5.2.6}$$

Set $v^{n+1} = \hat{v}$ and $p^{n+1} = \hat{p}$ in the fluid domain.

(II) Determine v^{n+1} in the particle domain by projecting $\hat{v}$ onto a rigid body motion, i.e. solve

$$\rho_s \left(\frac{v^{n+1} - \hat{v}}{\Delta t} \right) = f \quad \text{in} \quad S. \tag{5.2.7}$$

To solve equation (5.2.7), one needs knowledge of f. Following Sharma/Patankar [SP05], an equation for f can be obtained by imposing as an additional condition that *the total linear and angular momenta in the particle domain should be conserved*. To this end, we first split $\hat{v}$ as $\hat{v} = v_r + v'$, where

$$v_r = V_C + \omega \times (x - x_C),$$
$$m_S V_C = \int_S \rho_s \hat{v} \, dx \quad \text{and} \quad I_S \omega = \int_S (x - x_C) \times \rho_s \hat{v} \, dx. \tag{5.2.8}$$

Here, m_S (I_S, resp.) denotes the mass (moment of inertia, resp.) of the particle. Since the total linear and angular momenta should be conserved in the projection step, set $v^{n+1} = v_r$ in the particle domain. This corresponds to

$$f = -(\rho_s v')/\Delta t. \tag{5.2.9}$$

Remark 5.3. The algorithmic realization of the projection step (5.2.7) is very cheap. However, the accuracy of the integrations in (5.2.8) can be argued since the particle boundaries and the underlying grid do not match in general. We address this point in Section 5.2.3.

Remark 5.4. In the actual implementation of the second fractional step (5.2.7), instead of using (5.2.9) we compute f according to

$$f = -(\phi \rho_s v')/\Delta t. \tag{5.2.10}$$

Here, ϕ is the 'particle volume fraction' associated with a given grid point. By doing so we ensure that the velocity correction is properly smeared on the length scale of the grid size, cf. Patankar [Pat01]. Detailed information about the computation of ϕ is given in Section 5.2.3.

5.2.3 Algorithmic details

In this section we wish to give more detailed information about the algorithmic realization of the splitting scheme described in Section 5.2.2. In particular, we are going to comment on how we incorporate the concept of *adaptivity* into the scheme.

Mesh adaptation

In its original form the stress-DLM method has been described on uniform meshes in order to facilitate the use of special fast solution algorithms and to keep the cost of the solution process low. However, this may either lead to an insufficient resolution of the flow near the particle boundary and therefore to an inaccurate representation of the fluid-particle interaction or to enormous costs when handling many particles on a very fine mesh. As an alternative we propose to use locally adapted meshes which still have a good degree of regularity. The refinement zones of the mesh are attached to the particles following purely geometrical criteria and are moved according to the movement of the particles. In the case of particulate flows at moderate Reynolds numbers, we expect the error to be much larger near the particle boundaries than in the far-field region. Based on this heuristic criterion, we refine the grid around the particle boundaries in several stages, see Figure 5.1. It is clear that huge savings in terms of the number of needed grid cells are possible in comparison to uniform grid refinement. Whether further savings are possible by employing a systematic mesh refinement strategy based on a posteriori error estimation (cf. Section 2.2.4) still has to be examined.
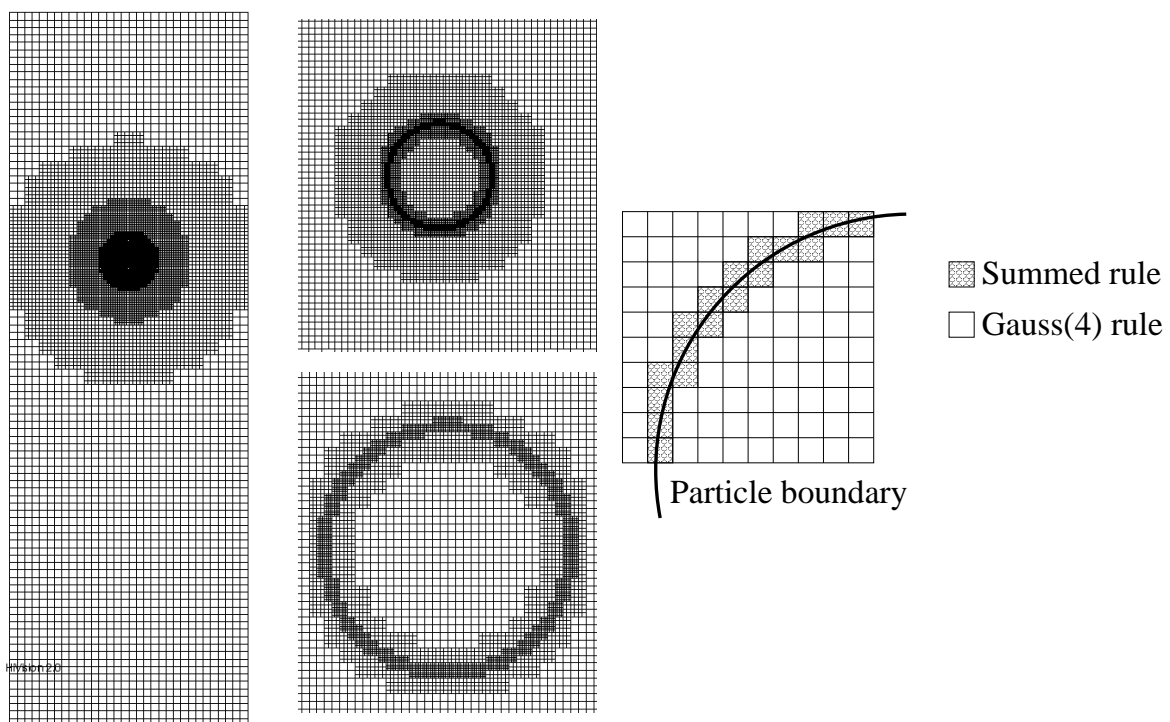

Figure 5.1: **Left:** A typical computational grid for the simulation of a single moving particle of circular shape (see also Section 5.3.1). Several refinement stages lead to a discretization which is both, economic and accurate. **Right:** A 'selective' quadrature rule is used to integrate functions over the particle domain. A summed Newton-Cotes rule is employed for boundary cells, while for all other cells a standard Gauss formula of high order is used.

Boundary approximation

As mentioned in Remark 5.3, the projection step (5.2.7) is very cheap. On the other hand, the accuracy of the integrations in (5.2.8) cannot be expected to be high since the particle boundaries and the underlying grid do not match. Of course, our local refinement strategy increases the accuracy. Another significant improvement can be achieved by using a 'selective quadrature rule': By a 'boundary cell' we wish to understand a cell which has non-empty intersection with the boundary of a particle. We want to integrate numerically $\int_S f(x)\, dx = \sum_i \int_{K_i} \chi_S(x) f(x)\, dx$, where $\{K_i\}$ denotes the mesh cells of a triangulation. Since $\chi_S(x) f(x)$ is, in general, a non-smooth function on boundary cells, it makes no sense to use a quadrature rule of high order for these cells. So while standard Gauss formulæ of high order are well-suited for non-boundary cells, it is better to employ a summed Newton-Cotes formula for boundary cells. This idea is also depicted in Figure 5.1 and validated quantitatively in Table 5.1.

Table 5.1: This table shows the discrete volume of a disk S with diameter $d = 0.25$. The exact value is $(d/2)^2 \pi \approx 0.0490874$. The result of the numerical integration of $\int_S 1\, dx$ with two different quadrature rules is shown: $\mathrm{vol}^h_G(S)$ refers to the use of a standard Gauss rule of order 4 for all cells. $\mathrm{vol}^h_\Sigma(S)$ refers to the use of a summed tensor midpoint formula for boundary cells, cf. Fig. 5.1.

h	$\mathrm{vol}^h_G(S)$	rel. error	$\mathrm{vol}^h_\Sigma(S)$	rel. error
2^{-4}	0.0498047	1.4613e-02	0.0491562	1.4016e-03
2^{-5}	0.0493164	4.6651e-03	0.0490866	1.6297e-05

Computation of the particle volume fraction ϕ

In the second fractional step (5.2.7) the fluid velocity is corrected in the particle domain. The straightforward implementation of this correction step would be to update the velocity at a grid point x if and only if $x \in S(t)$. However, numerical evidence suggests (see e.g. Patankar [Pat01]) that the accuracy of the projection step can be increased by weighting the velocity updates in the following way: We associate with each grid point x a value $0 \leq \phi(x) \leq 1$, the so-called 'particle volume fraction'. For vertices x which are 'properly' outside the particle domain, $\phi(x)$ should be equal to zero, while for vertices x which are 'properly' inside the particle domain, $\phi(x)$ should be equal to one. For vertices x which are located in the 'boundary layer' (i.e. which belong to 'boundary cells', see above), $\phi(x)$ should take a value between zero and one, depending on how close they are to the boundary.

The volume fraction $\phi(x)$ of a vertex x is computed as follows (see Figure 5.2): First, we determine all boundary cells $\{K^\partial\}$ and compute the particle volume fraction $\varphi(K^\partial)$ for these cells, $\varphi(K^\partial) := \mu(K^\partial)^{-1} \int_{K^\partial} \chi_S(x)\, dx$. The integral is approximated numerically by using a summed Newton-Cotes quadrature rule, see above. As the 'particle volume fraction' $\phi(x)$ of a vertex x we then simply take the mean value $\phi(x) = \sum_{i=1}^N \varphi(K_i)/N$, where $\{K_i\}_{i=1}^N$

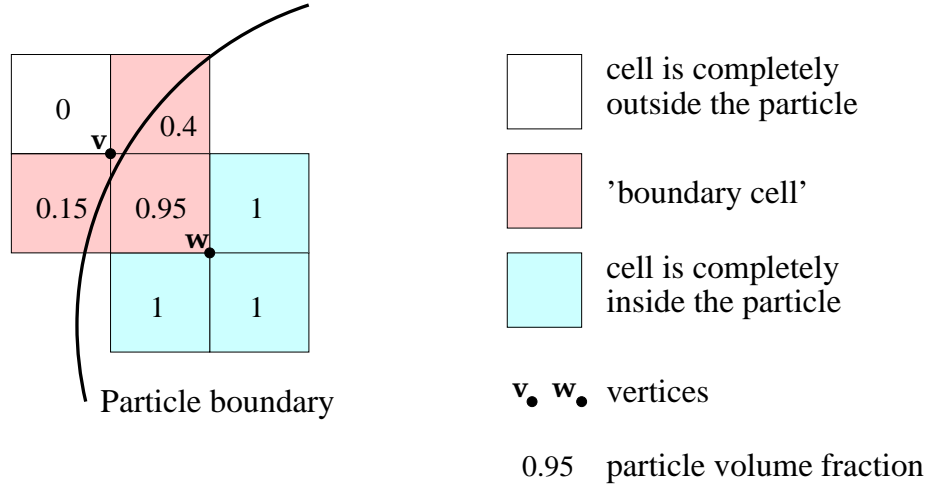denotes all cells to which the vertex x belongs. This procedure is also illustrated in Figure 5.2.

Figure 5.2: Computation of the 'particle volume fraction' ϕ. The first step consists in computing $\varphi(K^{\partial})$ for all boundary cells. The mean value of φ taken over the cells surrounding a vertex x determines $\phi(x)$. In the shown example, the fractions of the vertices **v** and **w** would be: $\phi(\mathbf{v}) = (0 + 0.15 + 0.4 + 0.95)/4 = 0.375$ and $\phi(\mathbf{w}) = (0.95 + 1 + 1 + 1)/4 = 0.9875$.

Space discretization and solver details

Until now we have not yet specified how we discretize and solve the PDE (5.2.6). The key ingredients of our solver technology shall be listed now. (For more details see also Section 4.3 and Bönisch et al. [BDR06].)

- We use the Galerkin finite element method (FEM) on locally refined meshes consisting of quadrilateral cells. As elements for velocity and pressure we take 'equal-order' Q_1 elements. This spatial discretization needs stabilization in order to compensate for the lacking 'inf-sup stability'. As an alternative to the usual SDLS (Streamline Diffusion Least-Squares) or SUPG (Streamline Upwinded Petrov Galerkin) stabilization of Hughes et al. [HB82, HFB86], we suggest the LPS (Local Projection Stabilization) method proposed in Becker/Braack [BB01] and Braack/Burman [BrB06] which has several advantages over the other stabilization methods.

- The nonlinear convective term is linearized by Newton's method.

- The system is solved in a fully-coupled manner; the resulting saddle-point problems are solved by the Generalized Minimal Residual Method (GMRES) with preconditioning by a geometric multigrid method with block-ILU smoothing.

- All simulations were done using the finite element simulation package **Gascoigne3D** (see [BB⁺05]). The visualization of the results was done with **HiVision** (see [BH06]).

Collision modeling

For simulating the motion of more than one particle, a collision model is needed to prevent the particles from penetrating each other or rigid walls. There is theoretical evidence that particle-particle or particle-wall collisions cannot take place in finite time in the continuous system since there are lubrication forces which prevent these collisions in the case of viscous fluids. However, particles can contact each other in numerical simulations. If the distance becomes smaller than the spatial resolution scale of the numerical method, truncation errors may (and do) lead to collisions or even to overlapping of particles unless special precautions are taken. Particle collisions pose severe difficulties in direct simulations of particulate flows. Even near-collisions can significantly increase the cost of a simulation, because the flow in the narrow region between the approaching particles must be accurately resolved. As a consequence, one has to employ extremely small mesh cells which corresponds to a significantly increased number of unknowns.

To handle this problem numerically, several collision models have been proposed in the literature. For simplicity, most of them assume that the collisions are 'smooth'. This means that if two rigid bodies collide under the effect of gravity and hydrodynamical forces, the velocities of the particles in question coincide at the points of contact. Glowinski, Joseph and coauthors [GPH+01] proposed a collision strategy which relies on the introduction of an artificial short-range repulsive force between the particles. The purpose of this force is to ensure that different particles always keep a positive distance. In this model, overlapping of the regions occupied by the rigid bodies is forbidden. However, in numerical calculations slight overlapping of particles can easily happen. Therefore, Joseph and coworkers [SHJ03] suggested a modified collision model in which the particles are allowed to come arbitrarily close and even to slightly overlap. Both models employ a short-range repulsion force between particles which are in near contact; the formulæ for these forces involve unknown scaling and stiffness parameters, the adequate choice of which is very important. Therefore, the models introduced by Glowinski, Joseph and coworkers [GPH+01, SHJ03] are commonly referred to as *parametric* models. In general, there is no rigorous theory to determine the ideal values for these parameters. In order to circumvent the delicate task of adjusting parameters, Minev et al. [DMN03] proposed another, *nonparametric* collision treatment. In Minev's model, the first step is to check if the distance between the particles is larger than a given threshold which correlates with the size of the particles and with the mesh width. If the distance is less than this threshold, then a repulsive force is calculated iteratively such that both particles move along the line that passes through the respective centers of mass and such that the minimum distance is still maintained. In the spirit of Minev's nonparametric model, Turek et al. [WT06] proposed another collision model which cannot only prevent the particles from getting too close, it can also deal with the case of slightly overlapping particles.

For our simulations we adopted the collision model of Turek et al. [WT06], but without allowing for particle overlapping. For particle-particle collisions of circular particles, the repulsive force is calculated as

$$
F_{ij}^{pp} := \begin{cases} 0, & \text{for } d_{ij} > r_i + r_j + \rho, \\ \frac{1}{\varepsilon}(x_C^i - x_C^j)(r_i + r_j + \rho - d_{ij})^2 & \text{for } r_i + r_j \leq d_{ij} \leq r_i + r_j + \rho, \end{cases}
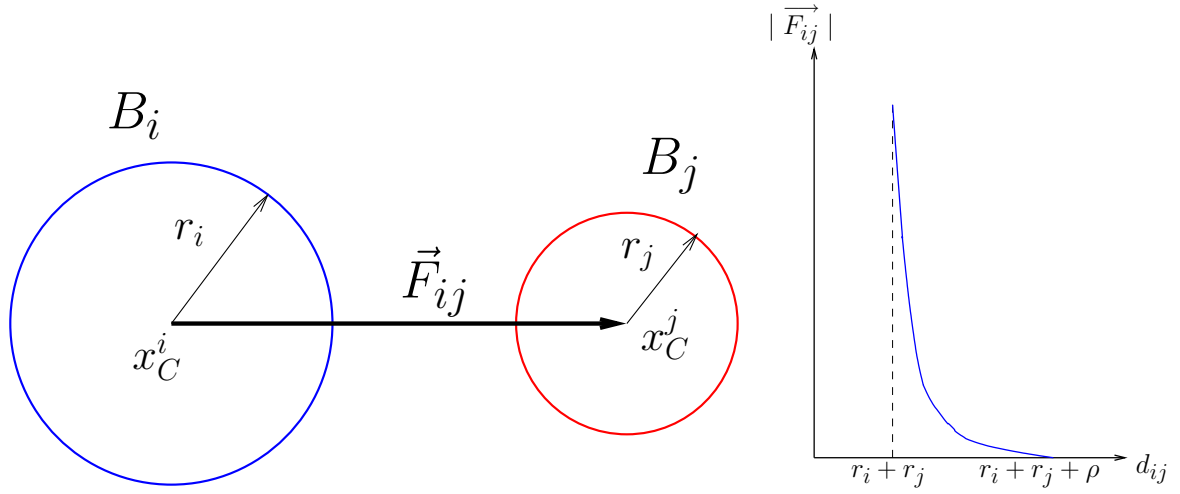\tag{5.2.11}
$$

Figure 5.3: Left: Illustration of the definitions needed for the description of the repulsive force F_{ij}. **Right:** Sketch of the qualitative behavior of the repulsive force F_{ij}.

where r_i and r_j are the radii of the ith and jth particle. x_C^i and x_C^j are the respective coordinates of the centers of mass and $d_{ij} := |x_C^i - x_C^j|$. ρ is the range of the repulsive force and is usually taken as $\rho \approx 0.5h$ with h the local mesh width. $\varepsilon \approx h^2$ is a small positive stiffness parameter. Figure 5.3 illustrates these definitions. For particle-wall collisions, we define for each particle S a 'virtual' or 'mirror' particle $\tilde{S}$ as the particle of the same size as S which is nearest to S and touches the respective wall from outside. Let us denote by $\tilde{x}_C^i$ the mass center of the 'mirror' particle of the ith particle and define $d_i := |x_C^i - \tilde{x}_C^i|$. Then the repulsive force reads as follows:

$$F_i^{pw} := \begin{cases} 0, & \text{for } d_i > 2r_i + \rho, \\ \frac{2}{\varepsilon}(x_C^i - \tilde{x}_C^i)(2r_i + \rho - d_i)^2 & \text{for } 2r_i \leq d_i \leq 2r_i + \rho. \end{cases} \tag{5.2.12}$$

The total repulsive forces exerted on the ith particle by the other particles and the walls are thus given by:

$$F_i := \sum_{j \neq i} F_{ij}^{pp} + F_i^{pw}. \tag{5.2.13}$$

Explicit update of the particle position and orientation

The final task in each timestep is, of course, the update of the position and the orientation of the particles. This is done explicitly. In two-dimensional simulations, the orientation of a particle is simply given by an angle α and the new orientation is obtained by integrating the (scalar) angular velocity, $\alpha^{n+1} = \alpha^n + \Delta t\,\omega$.

The update of the position x_C of the center of mass of a particle is achieved by the following sub-cycling procedure, cf. e.g. Patankar et al. [PSJ$^+$00]:

Set $x_C^{n+1,0} := x_C^n$. For $k = 1, \ldots, K$:

$$x_C^{*n+1,k} = x_C^{n+1,k-1} + \frac{\Delta t}{2K}\big(V_C^n + V_C^{n-1}\big),$$

$$x_C^{n+1,k} = x_C^{*n+1,k} + \frac{\Delta t^2}{2K^2}\frac{1}{2m_s}\big(F(x_C^{n+1,k-1}) + F(x_C^{*n+1,k})\big). \tag{5.2.14}$$

Set $x_C^{n+1} := x_C^{n+1,K}$, and

$$A_c^{n+1} := \frac{2}{\Delta t^2}\Big(x_C^{n+1} - x_C^n - \frac{\Delta t}{2}\big(V_C^n + V_C^{n-1}\big)\Big).$$

Here, F denotes the repulsive force introduced above, cf. (5.2.11-5.2.13). A_c is the acceleration of the particle due to collision. This term provides an additional body force acting on the particle and is included in the combined momentum equation (5.2.6) to be solved in the subsequent step.

Remark 5.5. The role of the sub-cycling procedure described above is that of a *predictor-corrector* method with the local time step size $\Delta t/K$ to determine the new particle positions. It is used in an almost identical way in all major variants of fictitious-domain methods for particulate flow problems, cf. [GPH+01, Pat01, PSJ+00, SP05, WT06].

5.3 Numerical experiments

In this section we present computational results using our adaptive fictitious-domain algorithm. We start with solving a well-known benchmark problem for a single moving particle (Section 5.3.1). Then we proceed to multiple particles (Section 5.3.2 and 5.3.3). The issue of non-smooth particle geometries is addressed in Section 5.3.4.

5.3.1 A benchmark problem

To validate our adaptive scheme, we first consider a benchmark problem which has been used by several authors to test their computational techniques (see e.g. Patankar et al. [PSJ+00], Wan/Turek [WT06]). We want to simulate the fall of a rigid disk in a bounded, rectangular cavity Ω filled with an incompressible Newtonian fluid. The setup of this problem is as follows:

- $\Omega = (0, 2) \times (0, 6)$
- The diameter of the disk is $d = 0.25$.
- At time $t = 0$ the disk is located at $(1, 4)$.
- The fluid as well as the disk are at rest initially; the fluid is at rest at the boundary of the cavity.
- The fluid density is $\rho_f = 1$, the disk density is $\rho_s = 1.25$.
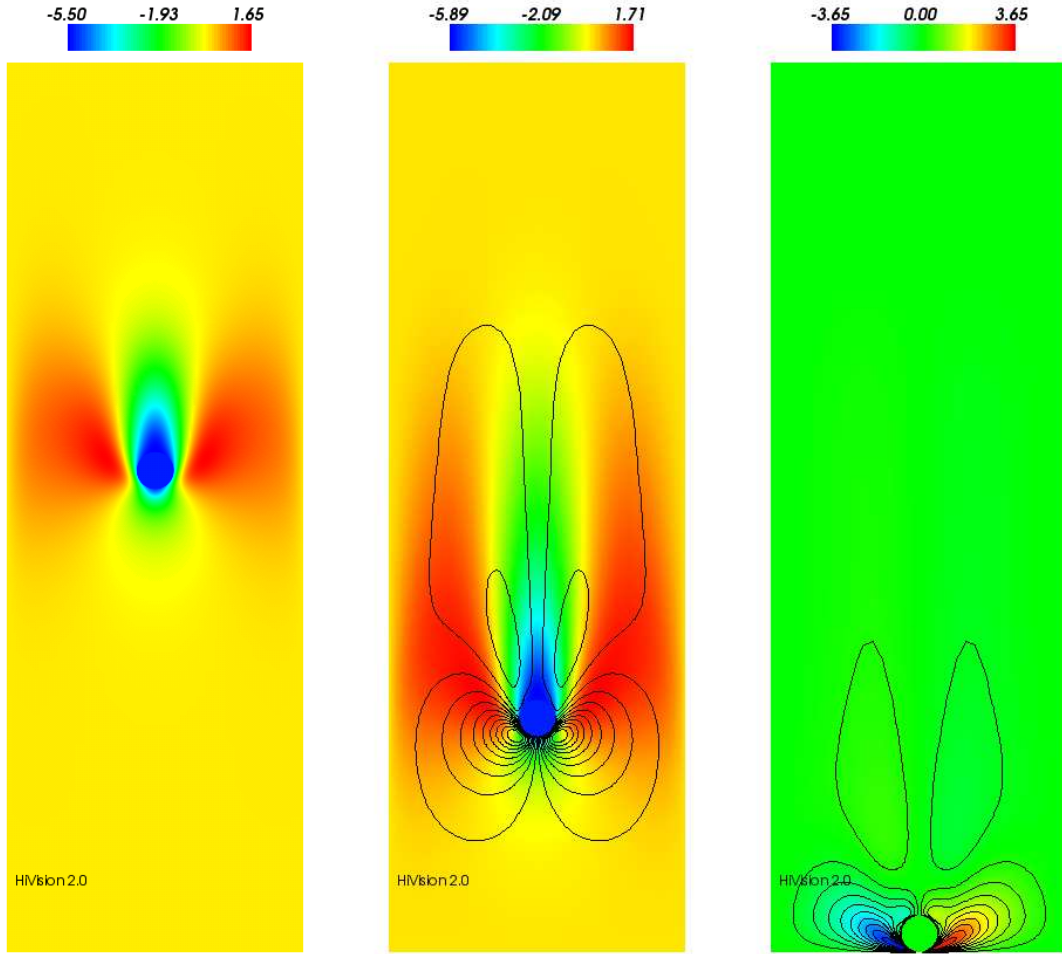- The fluid viscosity is $\mu = 0.1$.

Figure 5.4: **Left**: vertical component of the velocity field at $t = 0.2s$; **Middle**: vertical component of the velocity field at $t = 0.5s$ with isolines of the horizontal component; **Right**: horizontal component of the velocity field and isolines at $t = 0.77s$, just before 'contact'.

The results of the numerical simulation are shown in Figure 5.4, see also Figure 5.1. Figure 5.5 shows the temporal evolution of the y-component of the mass center of the disk and of the vertical component of the particle velocity. The disk starts from rest and accelerates until it reaches its maximum velocity. At $t \approx 0.77s$, it hits the bottom of the cavity. (More precisely, it reaches a terminal distance from the wall which is of the order of the local mesh width, cf. the discussion in Section 5.2.3. A quantitative comparison of our findings with the results described in Glowinski et al. [GPH$^+$01] is given in Table 5.2. We obtain a maximum value of the Reynolds number of the particle which is very close to the reference value provided by Glowinski et al. [GPH$^+$01]. However, due to the use of adaptive mesh refinement, we achieve huge savings in terms of the number of needed grid cells.
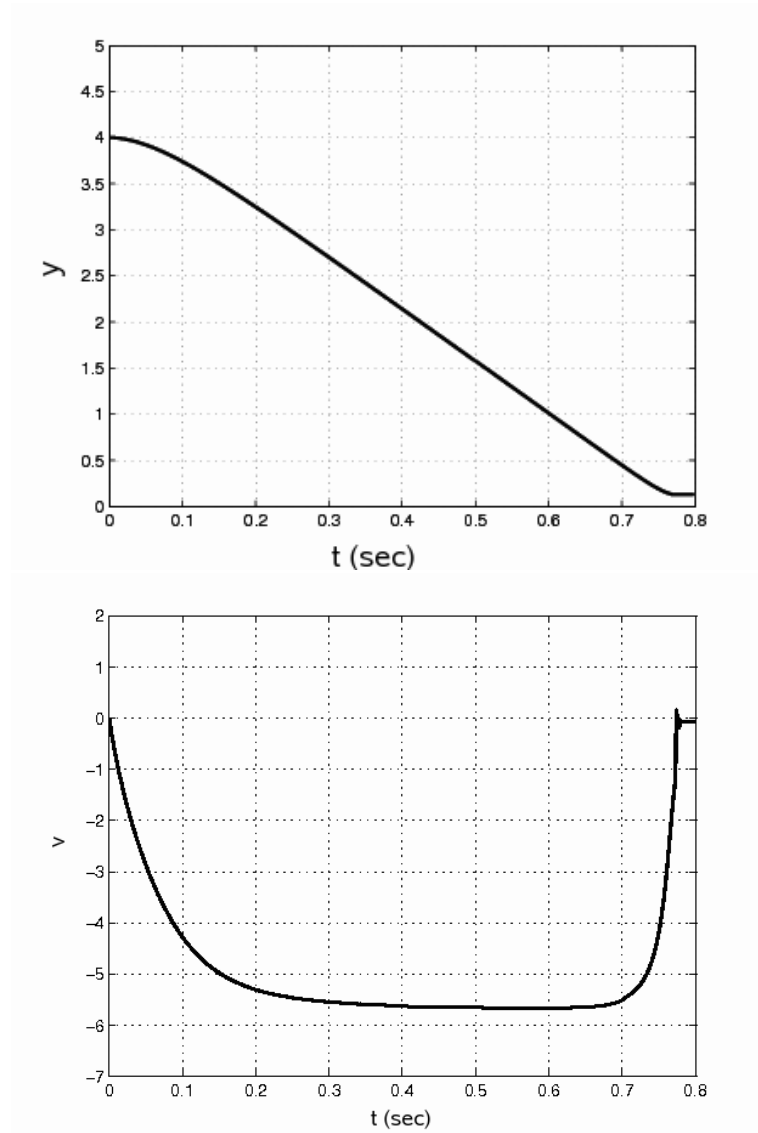
Figure 5.5: **Top:** y-component of the mass center of the disk vs. time; **Bottom:** vertical velocity component v vs. time.

Table 5.2: **Left:** Maximum Reynolds number obtained by Glowinski et al. [GPH$^+$01]. $Re_{\max}^{(1)}$ and $Re_{\max}^{(2)}$ refer to two different numerical schemes, both employing globally refined meshes. **Right:** Maximum Reynolds number obtained with our adaptive method. The agreement with the reference value provided by Glowinski et al. [GPH$^+$01] is very good; only a fraction of mesh cells is needed.

# cells	$Re_{\max}^{(1)}$	$Re_{\max}^{(2)}$
$\approx 440{,}000$	17.27	17.44
$\approx 780{,}000$	17.31	17.51

# cells	$Re_{\max}$
$\approx 12{,}000$	17.62
$\approx 18{,}000$	17.71
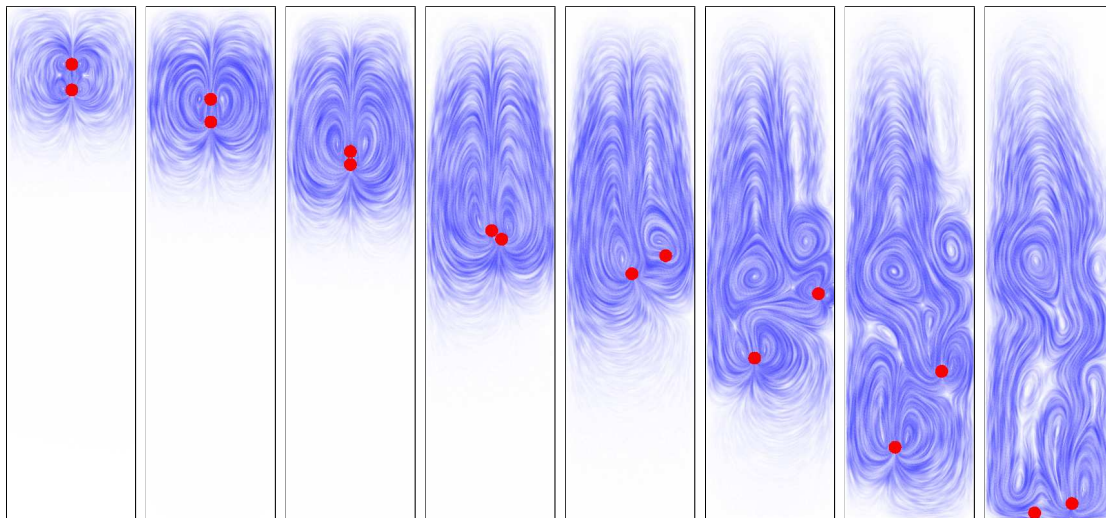
Figure 5.6: The typical 'drafting,kissing,tumbling' phenomenon can be observed (cf. [GPH+01]): The lagging particle falls faster than the leading one because it experiences less drag ('drafting'). The two particles touch ('kiss'). But since this is an unstable configuration in a Newtonian fluid, they separate and 'tumble' apart.

5.3.2 Interaction of two circular particles

We now consider the simplest situation involving more than one particle. We simulate the fall of two rigid circular particles in a bounded, rectangular cavity Ω. The setup of this problem is as follows (cf. Wan/Turek [WT06]):

- $\Omega = (0, 2) \times (0, 8)$

- The diameter of the disks is $d = 0.2$.

- At time $t = 0$ the disks are located at $(1, 7.2)$ and $(1, 6.8)$, resp.

- The fluid density is $\rho_f = 1$, the disk density is $\rho_s = 1.01$.

- The fluid viscosity is $\mu = 0.01$.

Figure 5.6 shows the result of the simulation. The well-known phenomenon of 'drafting, kissing and tumbling' is clearly reproduced (cf. e.g. Glowinksi et al. [GPH+01]). A quantitative comparison with Wan/Turek [WT06] is also very promising (see Figure 5.7 and compare with Figure 19 in [WT06]).

5.3.3 Configurations with many particles

Now we proceed to configurations with more than two particles. Unfortunately, to date there is no commonly accepted benchmark problem for this case. We therefore defined and simulated two model configurations without being able to compare our results with the literature.
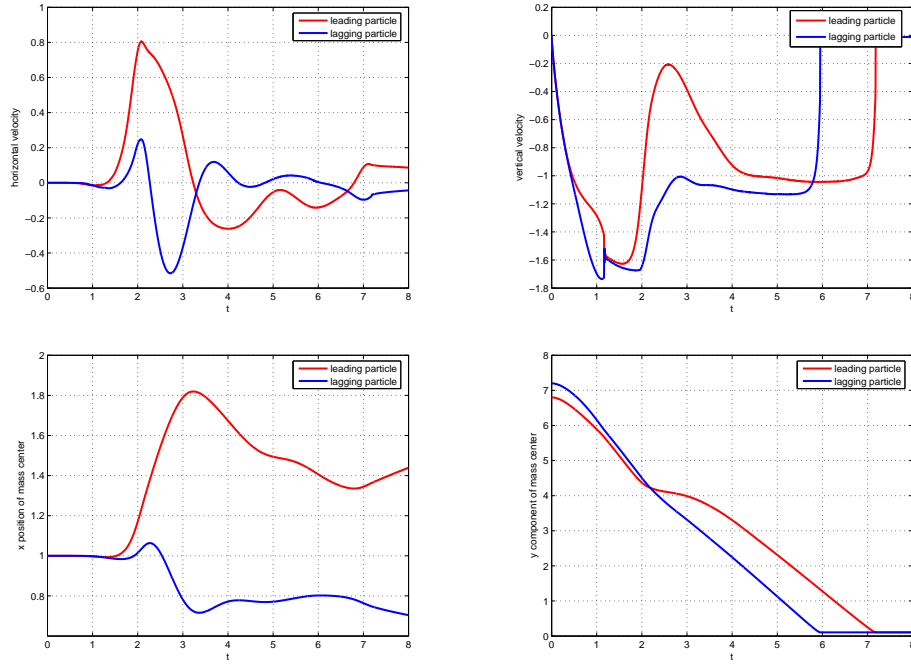
Figure 5.7: First row: horizontal (**left**) and vertical (**right**) component of the translational velocity. **Second row:** x-position (**left**) and y-position (**right**) of the mass centers.

a = 0,   b = $^5/_6$,   c = $^7/_6$,   d = 2

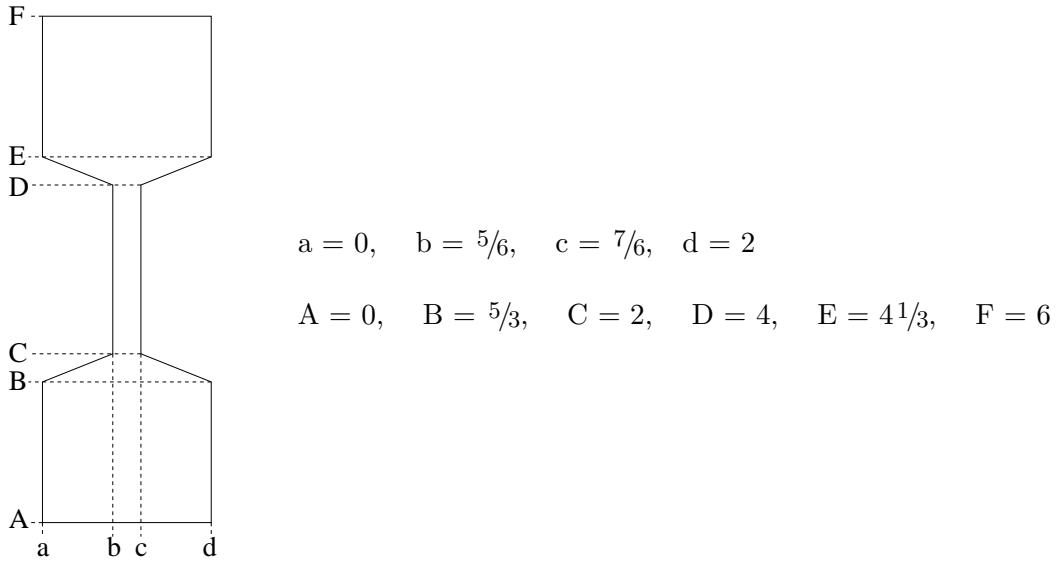A = 0,   B = $^5/_3$,   C = 2,   D = 4,   E = $4^1/_3$,   F = 6

Figure 5.8: Specification of the 'sand glass'-geometry for Problem B.

Problem A: free fall of 41 circular particles through a constriction

Figures 5.9 and 5.10 show the 2D motion of a number of circular particles subject to gravity in a vertical channel with a constriction. The geometry of the domain Ω and the initial positions of the particles as well as the other relevant parameters are as follows (see also Figure 5.9):

- $\Omega = [(0,2) \times (0,6)] \setminus \left\{ [(0, \frac{2}{3}) \times (4, 4\frac{2}{3})] \cup [(\frac{4}{3}, 2) \times (4, 4\frac{2}{3})] \right\}$
- The diameter of the disks is $d = 0.1$.
- The fluid density is $\rho_f = 1$, the disk density is $\rho_s = 1.25$.
- The fluid viscosity is $\mu = 0.1$.

The initial 'pyramid-like' positioning of the particles is depicted on the left-hand side of Figure 5.9. The setup is slightly asymmetric (One particle on the right is missing.) in order to avoid that the symmetry-breaking is triggered by numerical instabilities. The simulation was done on dynamically adapted meshes with about $20,000 - 40,000$ cells and minimal mesh width $h_{\min} \approx 0.005$. The finest mesh was obtained by 4 global and 3 additional local refinement steps. This finest mesh would correspond to a globally refined mesh with about $440,000$ cells. The (uniform) time step was $\Delta t = 0.005$, i.e., 2000 time steps were needed for the computation over the relevant time interval $[0, 10]$. The whole simulation took about 1 day on an AMD Athlon64 3500+ computer. This time could be significantly reduced by optimizing the components of the multigrid solver used within each time step.

Problem B: free fall of 64 circular particles through a 'sand glass'

We want to simulate the 2D motion of 64 circular particles through a domain with a 'sand glass' geometry, see Figure 5.8. Initially, the particles are closely packed in a regular array of 8×8 particles; the center of the array is the point $(1, 5)$. Besides the geometry and the particle positions, the setup is identical with that of Problem A (same fluid and particle densities, particle diameter, viscosity). The result of the simulation is shown in Figure 5.11.

5.3.4 Non-smooth particle geometry

We wish to conclude this section by pointing out that the use of locally refined meshes is even more crucial when simulating the motion of particles with non-smooth boundaries. In the context of fictitious-domain methods it is inevitable that sharp corners are smeared out on the length scale of the local mesh size. Therefore it is advisable to refine very strongly around such corners. In Figure 5.12 a snapshot of a simulation of a moving triangle is shown. The resolution of the particle geometry is excellent. It would have been practically impossible to get a similar result with uniform grid refinement.
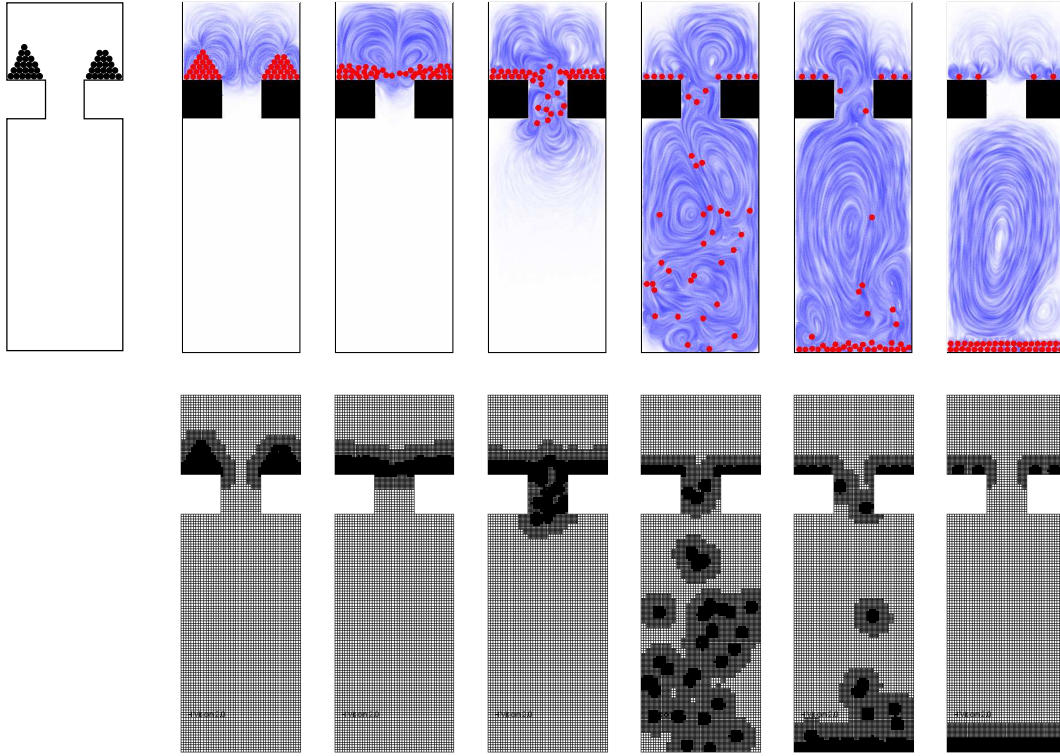
Figure 5.9: Free fall of multiple particles in a viscous Newtonian liquid (Problem A). Sketch of the initial positions of the particles (**top left**), temporal evolution of the flow field and particle positions (**upper row**) and corresponding adapted meshes (**lower row**). The pictures correspond to the following points in time: 0.01, 0.25, 1.0, 2.55, 4.0, 8.5.
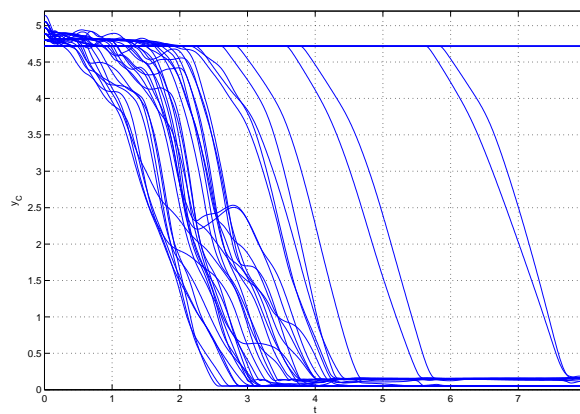

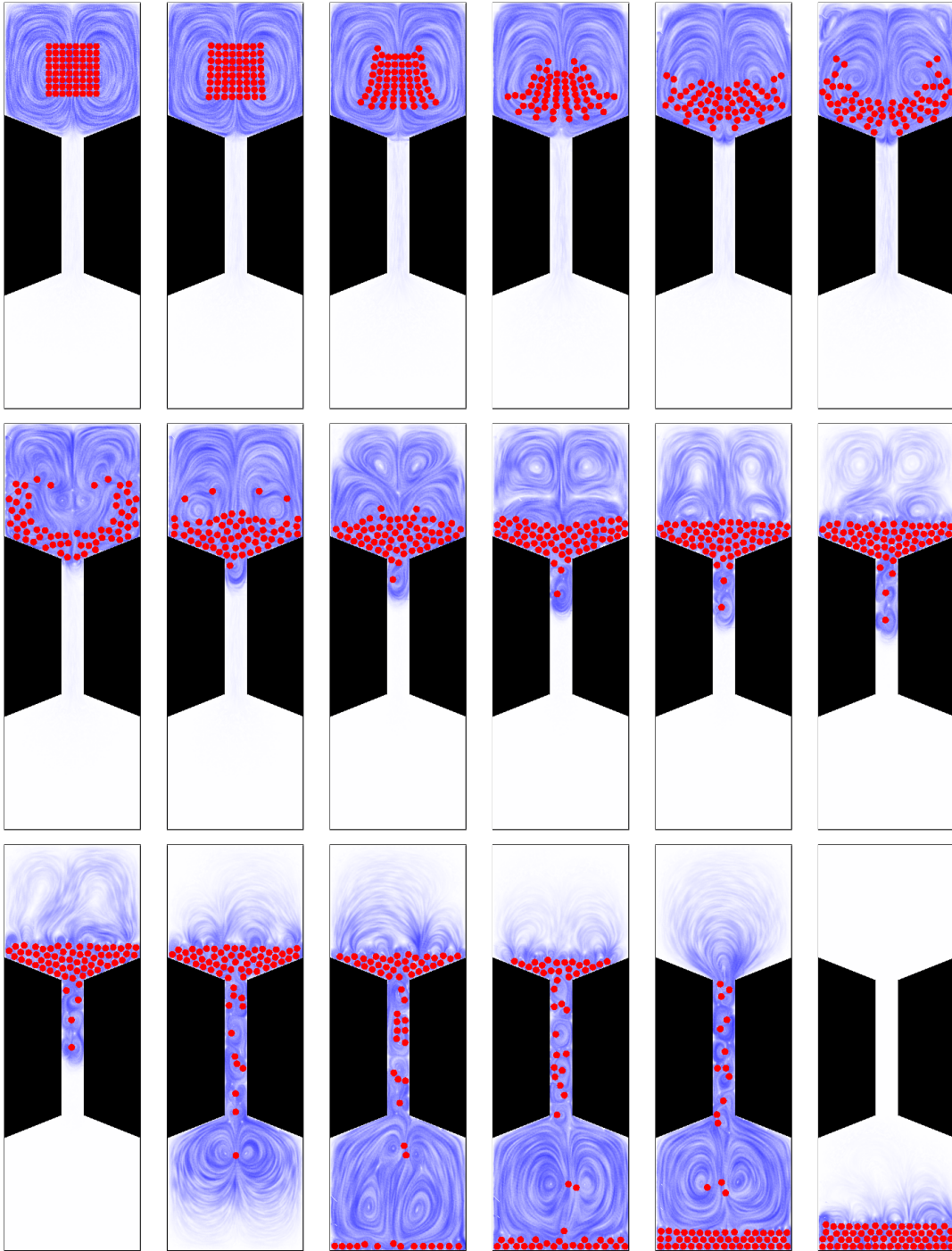**Figure 5.10:** Temporal evolution of the y-component of the mass centers for Problem A.

Figure 5.11: Temporal evolution of the flow field and particle positions for Problem B. The pictures correspond to the following points in time: 0.01, 0.05, 0.1, 0.15, 0.2, 0.25 (**upper row**), 0.4, 0.6, 0.8, 1, 1.2, 1.4 (**middle row**) and 1.5, 3, 7, 10, 15, 20 (**lower row**).
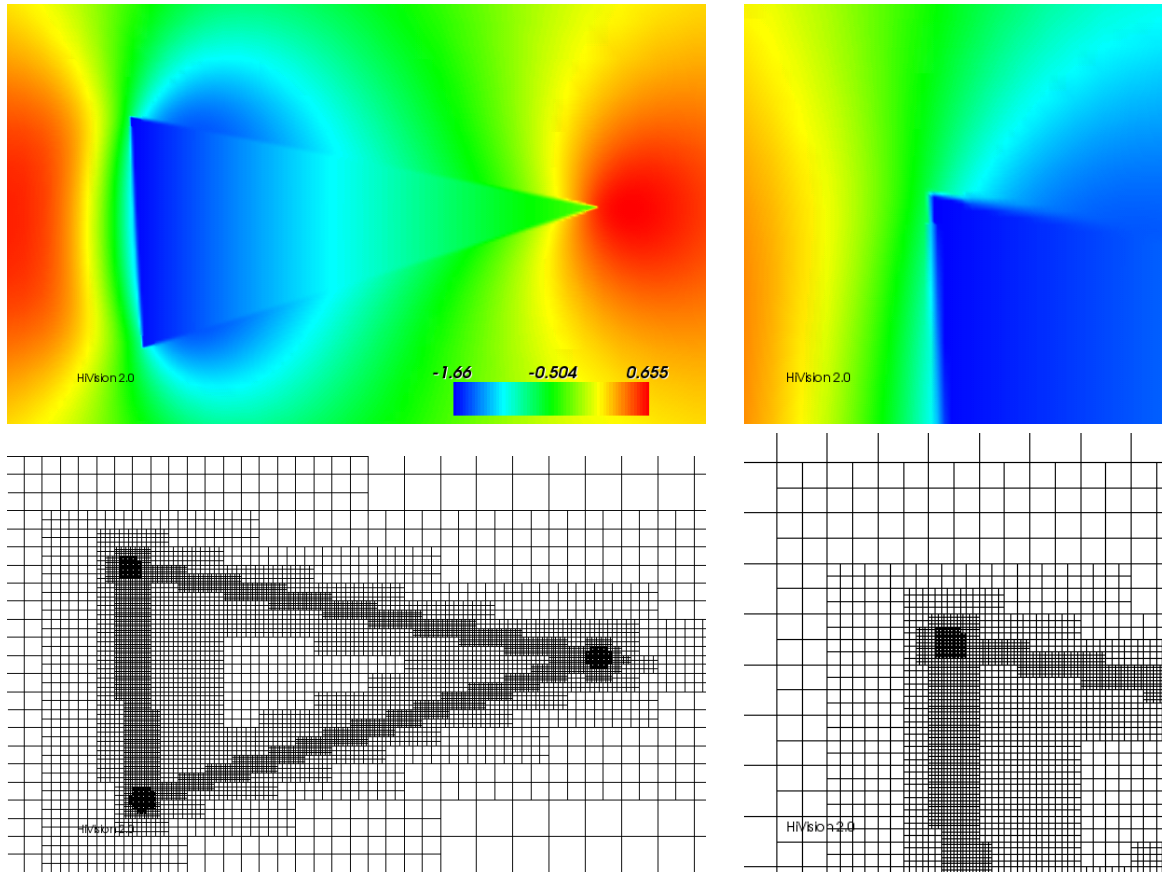
Figure 5.12: Top: The flow around a moving triangular particle is shown (**left**). A zoom on one of the sharp corners shows that the resolution of the highly non-smooth particle geometry is very satisfying (**right**). **Bottom:** Corresponding finite element grids. Local mesh refinement is crucial for the accurate resolution of the sharp corners.

Acknowledgments

Bibliography

[All84]   J.R.L. Allen, *Experiments on the settling, overturning and entrainment of bi-valve shells and related models.* Sedimentology **31**(1984), 227–250.

[Asm99]   E. Asmolov, *The inertial lift on a spherical particle in a plane Poiseuille flow at large channel Reynolds number.* J. Fluid Mech **381**(1999), 63–87.

[BM84a]   I. Babuška and A. Miller, *The post processing approach in the finite element method, part 1: calculation of displacements, stresses and other higher derivatives of the displacements.* Inter. J. Numer. Meth. Engrg. **34**(1984), 1085–1109.

[BM84b]   I. Babuška and A. Miller, *The post processing approach in the finite element method, part 2: the calculation of stress intensity factors.* Inter. J. Numer. Meth. Engrg. **34**(1984), 1111–1129.

[BM84c]   I. Babuška and A. Miller, *The post processing approach in the finite element method, part 3: a posteriori estimates and adaptive mesh selection.* Inter. J. Numer. Meth. Engrg. **34**(1984), 1131–1151.

[Bat67]   G.K. Batchelor. *An Introduction to Fluid Dynamics.* Cambridge University Press, 1967.

[BB01]   R. Becker, M. Braack, *A Finite Element Pressure Gradient Stabilization for the Stokes Equations Based on Local Projections.* Calcolo **38**(2001), 173–199.

[BB+05]   R. Becker, M. Braack et al.: *Gascoigne: A C++ numerics library for scientific computing.* Institute of Applied Mathematics, University of Heidelberg, URL `http://www.gascoigne.uni-hd.de/` .

[BD98]   E. Bänsch and W. Dörfler, *Adaptive finite elements for exterior domain problems.* Numer. Math. **80** (1998), 497–523.

[BaR03]   W. Bangerth and R. Rannacher, *Adaptive Finite Element Methods for Differential Equations.* Lectures in Mathematics, ETH Zürich, Birkhäuser, Basel 2003.

[BeHR02]   R. Becker, V. Heuveline, and R. Rannacher, *An optimal control approach to adaptivity in computational fluid mechanics.* Int. J. Numer. Meth. Fluids **40**(2002), 105–120.

[BKS96]   L.E. Becker, G.H. McKinley, H.A. Stone, *Sedimentation of a sphere near a plane wall: waek non-Newtonian and inertial effects.* J. Non-Newtonian Fluid Mech. **63**(1996), 201–233.

[BeR01]   R. Becker and R. Rannacher, *An optimal control approach to error estimation and mesh adaptation in finite element methods.* Acta Numerica 2000 (A. Iserles, ed.), pp. 1-102, Cambridge University Press, 2001.

Bibliography

[BEM98]   A. Belmonte, H. Eisenberg, and E. Moses, *From flutter to tumble, Inertial drag and Froude similarity in falling paper.* Phys. Rev. Lett. **81** (1998), 345–348.

[Boe06]   S. Bönisch, *An adaptive fictitious-domain method for quantitative studies of particulate flows.* Submitted to Proc. Int. Conf. on High Performance Scientific Computing (HPSCHanoi 2006).

[BDR06]   S. Bönisch, Th. Dunne, R. Rannacher, *Numerics of fluid-structure interaction.* In: Hemodynamical Flows: Aspects of Modeling, Analysis and Simulation, (A.M. Robertson, G.P. Galdi, R. Rannacher, S. Turek, eds), to appear 2006.

[BG06]   S. Bönisch and G.P. Galdi, *Sedimentation of particles through a Poiseuille flow in a vertical channel.* In preparation, 2006.

[BH04a]   S. Bönisch and V. Heuveline, *On the numerical simulation of the unsteady free fall of a solid in a fluid. I. The Newtonian case.* Computers and Fluids, to appear, 2006.

[BH04b]   S. Bönisch and V. Heuveline, *On the numerical simulation of the free fall of a solid in a fluid. II. The viscoelastic case.* SFB Preprint 2004-32, University of Heidelberg, 2004.

[BH06]   S. Bönisch and V. Heuveline, *Advanced flow visualization with HiVision.* Abschlußband SFB 359, Reactive Flows, Diffusion and Transport (W. Jäger et al., eds), Springer, Berlin-Heidelberg-New York, 2006.

[BHR05]   S. Bönisch, V. Heuveline, R. Rannacher, *Numerical simulation of the free fall problem.* Proc. Int. Conf. on High Performance Scientific Computing (HPSCHanoi 2003), Hanoi, March 2003, (H.G. Bock, et al., eds), Springer, Berlin-Heidelberg, 2005.

[BHW05]   S. Bönisch, V. Heuveline and P. Wittwer: *Adaptive boundary conditions for exterior flow problems*, J. Math. Fluid Mech. **7** (2005), 85–107.

[BHW06]   S. Bönisch, V. Heuveline and P. Wittwer: *Second order adaptive boundary conditions for exterior flow problems: non-symmetric stationary flows in two dimensions*, J. Math. Fluid Mech. **8**(2006), 1–26.

[BrB06]   M. Braack and E. Burman: *Local projection stabilization for the Oseen problem and its interpretation as a variational multiscale method*, SIAM J. Numer. Anal. **43**(2006), 2544–2566.

[BS94]   S.C. Brenner and R.L. Scott, *The mathematical theory of finite element methods.* Springer, Berlin-Heidelberg-New York, 1994.

[BF91]   F. Brezzi and R. Falk, *Stability of higher-order Hood-Taylor methods.* SIAM J. Numer. Anal. **28**(1991), 581–590.

[BLW01]   R. Burger, R. Liu, and W.L. Wendland, *Existence and stability for mathematical models of sedimentation-consolidation processes in several space dimensions.* J. Math. Anal. Appl. **264**, 288–310.

[Chh93]   R.P. Chhabra, *Bubbles, drops and particles in non-Newtonian fluids.* Chemical Industries Series, Vol. **113**, CRC Press, 1993.

[CMT00]   C. Conca, J.S. Martin, and M. Tucsnak, *Existence of the solutions for the equations modelling the motion of rigid body in a viscous fluid.* Commun. Partial Differ. Equations **25** (2000), 1019–1042.

[CB68]   R.G. Cox and H. Brenner, *The lateral migration of solid particles in Poiseuille flow. I. Theory.* Chem. Engng. Sci. **23**(1968), 625–643.

[DE99]   B. Desjardin and M. Esteban, *Existence of weak solutions for the motion of rigid bodies in viscous fluids.* Arch. Rational Mech. Anal. **46** (1999), 59–71.

[DJ03]   C. Duchanoy and T.R.G. Jingen, *Efficient simulation of liquid-solid flows with high solids fraction in complex geometries.* Computers and Fluids **32**(2003), 1453–1471.

[DMN03]   C. Diaz-Goano, P. Minev, K. Nandakumar, *A fictitious-domain/finite element method for particulate flows.* J. Comp. Phys. **192**(2003), 105–123.

[ES64]   R. Eichhorn and S. Small, *Experiments on the lift and drag of spheres suspended in a Poiseuille flow.* J. Fluid Mech **20**(1964), 513–527.

[FKM⁺97]   S. B. Field, M. Klaus, M. G. Moore, and F. Nori *Chaotic dynamics of falling disks.* Nature **388** (1997), 252–254.

[Gal98a]   G. P. Galdi, *An introduction to the mathematical theory of the Navier-Stokes equations: Linearized steady problems.* Springer Tracts in Natural Philosophy, Vol. **38**, Springer-Verlag, 1998.

[Gal98b]   G. P. Galdi, *An introduction to the mathematical theory of the Navier-Stokes equations: Nonlinear steady problems.* Springer Tracts in Natural Philosophy, Vol. **39**, Springer-Verlag, 1998.

[Gal99]   G. P. Galdi, *On the steady self-propelled motion of a body in a viscous incompressible fluid.* Arch. Rational Mech. Anal. **148** (1999), 53–88.

[Gal01]   G. P. Galdi, *On the motion of a rigid body in a viscous liquid: A mathematical analysis with applications.* Handbook of Mathematical Fluid Mechanics (S. Friedlander and D. Serre, eds), Elsevier, 2001.

[GH06]   G.P. Galdi and V. Heuveline, *Lift and sedimentation of particles in the flow of a viscoelastic liquid in a channel.* Proc. Workshop on Free and Moving Boundaries, Houston TX, Dec. 2-4, 2004, (R. Glowinski and J.P. Zolesio, eds), 2006.

[GV01]   G. P. Galdi and A. Vaidya, *Translational steady fall of symmetric bodies in a Navier-Stokes liquid, with application to particle sedimentation.* J. Math. Fluid Mech. **3** (2001), 183–211.

[GVP⁺02]   G.P. Galdi, A. Vaidya, M. Pokorny, D. D. Joseph, J. Feng, *Orientation of bodies sedimenting in a second-order liquid at non-zero Reynolds number.* Math. Models Methods Appl. Sci. **12** (2002),1653-1690.

[GLL⁺97]   M. Giles, M. Larson, M. Levenstam, and E. Süli, *Adaptive error control for finite element approximations of the lift and drag coefficients in viscous flow.* Technical Report NA-97/06, Oxford University Computing Laboratory, 1997.

[GR86]   V. Girault and P.-A. Raviart, *Finite Element Methods for the Navier-Stokes Equations.* Springer: Berlin-Heidelberg-New York, 1986.

[GPH+01]   R. Glowinski, T. Pan, T. Hesla, D.D. Joseph, J. Périaux, *A fictitious-domain approach to the direct numerical simulation of incompressible viscous flow past moving rigid bodies: application to particulate flow.* J. Comp. Phys. **169**(2001), 363–426.

[Gra68]   J. Gray, *Animal locomotion.* Weidenfels and Nicolson, London, 1968.

[GS90]   P.D. Grossman and D.S. Soane, *Orientation effects on the electrophoretic mobility of rod-shaped molecules in free solution.* Anal. Chem. **62**(1990), 1592–1596.

[GLS00]   M.D. Gunzburger, H.C. Lee, and G.A. Seregin, *Global existence of weak solutions for viscous incompressible flows around a moving rigid body in three dimensions.* J. Math. Fluid Mech. **2**(2000), 219–266.

[Heu06]   V. Heuveline, *HiFlow: A multi-purpose finite-element package*, Rechenzentrum, Universität Karlsruhe, URL `http://hiflow.de/` .

[HR06]   V. Heuveline and R. Rannacher, *Adaptive FEM for eigenvalue problems with application in hydrodynamic stability analysis.* Preprint, Inst. of Applied Mathematics, Univ. of Heidelberg, 05/2006, to appear in special issue of J. Numer. Math., 2006.

[HL74]   B.P. Ho and L.G. Leal, *Inertial migration of rigid spheres in two-dimensional unidirectional flows.* J. Fluid Mech. **65**(1974), 365–400.

[HL76]   B.P. Ho and L.G. Leal, *Migration of rigid spheres in two-dimensional unidirectional shear flow of a second-order fluid.* J. Fluid Mech. **76**(1976), 783–799.

[HS00]   K. H. Hoffmann and V. N. Starovoitov, *Zur Bewegung einer Kugel in einer zähen Flüssigkeit.* Doc. Math. **5**(2000), 15–21.

[HT73]   P. Hood and C. Taylor, *A numerical solution of the Navier-Stokes equations using the finite element technique.* Computers and Fluids **1**(1973), 73–100.

[Hu96]   H. H. Hu, *Direct simulation of flows of solid-liquid mixtures.* Int. J. Multiphase Flow **22**(1996), 335–352.

[HJC92]   H. H. Hu, D. D. Joseph, and M. J. Crochet, *Direct simulation of fluid particle motions.* Theor. Comp. Fluid Dyn. **3**(1992), 285–306.

[HB82]   T.J.R. Hughes and A.N. Brooks, *Streamline upwind/Petrov–Galerkin formulations for convection dominated flows with particular emphasis on the incompressible Navier-Stokes equation.* Comput. Meth. Appl. Mech. Engrg. **32**(1982), 199–259.

[HFB86]   T.J.R. Hughes, L.P. Franc, and M. Balestra, *A new finite element formulation for computational fluid mechanics: V. Circumventing the Babuska-Brezzi condition: A stable Petrov-Galerkin formulation of the Stokes problem accommodating equal order interpolation.* Comput. Meth. Appl. Mech. Engrg. **59**(1986), 85–99.

[HPZ01]   H.H. Hu, N.A. Patankar, M.Y. Zhu, *Direct numerical simulations of fluid solid systems using Arbitrary Lagrangian-Eulerian technique.* J. Comp. Phys. **169**(2001), 427–462.

[JP65]   R.C. Jeffrey and J.R.A. Pearson, *Particle motion in laminar vertical tube flow.* J. Fluid Mech. **22**(1965), 721–735.

[JT96]   A. Johnson, T.E. Tezduyar, *Simulation of multiple spheres falling in a liquid-filled tube.* Comp. Meth. Appl. Mech. Engng., **134**(1996), 351–373.

[Jos90]   D.D. Joseph, *Fluid dynamics of viscoelastic liquids.* Applied Mathematical Sciences, Vol. **84**, Springer, 1990.

[Jos00]   D.D. Joseph, *Interrogations of direct numerical simulation of solid-liquid flows.* *www.aem.umn.edu/people/faculty/joseph/interrogation.html*,   Online   book, 2000.

[Kaj82]   M. Kajikawa, *Observation of the falling motion of early snowflakes.* J. Meteorol. Soc. Jpn. **60**, 797–803.

[Lad94a]   A.J.C. Ladd, *Numerical simulation of particulate suspensions via a discretized Boltzmann equation. I. Theoretical foundation.* J. Fluid Mech. **271**(1994), 285–309.

[Lad94b]   A.J.C. Ladd, *Numerical simulation of particulate suspensions via a discretized Boltzmann equation. II. Numerical results.* J. Fluid Mech. **271**(1994), 311–339.

[LV01]   A.J.C. Ladd and R. Verberg, *Lattice-Boltzmann simulations of particle fluid suspensions.* J. Stat. Phys. **104**(2001), 1191–1251.

[LBH+96]   C.L. Ladson, C.W. Brooks, A.S. Hill Jr., and D.W. Sproles, *Computer program to obtain ordinates for NACA airfoils.* NASA Technical Memorandum 4741 (1996).

[LYH+97]   S.C. Lee, D.Y. Yang, J. Ko, J.R. You, *Effect of compressibility on flow field and fiber orientation during the filling stage of injection molding.* J. Mater. Process. Tech. **70**(1997), 83–92.

[LJ93]   Y.J. Liu and D.D. Joseph, *Sedimentation of particles in polymer solutions.* J. Fluid Mech, **255**(1993), 565–595.

[LR81]   M. Luskin and R. Rannacher, *On the smoothing property of the Galerkin method for parabolic equations.* SIAM J. Numer. Math. **19**(1981).

[NS03]   S.A. Nazarov and M. Specovius-Neugebauer, *Nonlinear artificial boundary conditions with pointwise error estimates for the exterior three dimensional Navier-Stokes problem.* Math. Nachr. **252**(2003), 86–105.

[Pat01]   N. A. Patankar, *A formulation for fast computations of rigid particulate flows.* Center Turbul. Res., Ann. Res. Briefs, 185–196 (2001).

[Pat05]   N. A. Patankar, *Physical interpretation and mathematical properties of the stress-DLM formulation for rigid particulate flows.* Int. J. Comp. Meth. Engrg Sci. Mech. **6**(2005), 137–143.

[PJ01a]   N. A. Patankar and D. D. Joseph, *Modeling and numerical simulation of particulate flows by the Eulerian-Lagrangian approach.* Int. J. Multiphase Flow **27**(2001), 1659–1684.

[PJ01b]   N. A. Patankar and D. D. Joseph, *Lagrangian numerical simulation of particulate flows.* Int. J. Multiphase Flow **27**(2001), 1685-1706.

[PJB+02]   T.W. Pan, D.D. Joseph, R. Bai, R. Glowinski, V. Sarin, *Fluidization of 1204 spheres: simulation and experiment.* J. Fluid Mech. **451**(2002), 169–191.

[PSJ+00]   N.A. Patankar, P. Singh, D.D. Joseph, R. Glowinski, and T.-W. Pan, *A new formulation of the distributed Lagrange multiplier/fictitious domain method for particulate flows.* Int. J. Multiphase Flow **26**(2000), 1509–1524.

[Poz97]   C. Pozrikidis, *Introduction to theoretical and computational fluid dynamics.* Oxford University Press, 1997.

[Ran84]   R. Rannacher, *Finite element solution of diffusion problems with irregular data.* Numer. Math. **43**(1984), 309–327.

[Ran00]   R. Rannacher, *Finite element methods for the incompressible Navier-Stokes equations.* In 'Fundamental Directions in Mathematical Fluid Mechanics' (G. P. Galdi et al., eds), pp. 191–293, Birkhäuser, Basel, 2000.

[Rus85]   K.J. Ruschak, *Coating flows.* Ann. Rev. Fluid Mech. **17**(1985), 65–89.

[Saa96]   Y. Saad. *Iterative methods for sparse linear systems.* Computer Science/Numerical Methods. PWS Publishing Company, 1996.

[SW69]   H. Schmid-Schönbein and R. Wells, *Fluid drop-like transition of erythrocytes under shear.* Science **165**(1969), 288–291.

[SP05]   N. Sharma and N. A. Patankar, *A fast computation technique for the direct numerical simulation of rigid particulate flows.* J. Comp. Phys. **205**(2005), 439–457.

[SS61]   G. Segrè and A. Silberberg, *Radial particle displacements in Poiseuille flow of suspensions.* Nature **189**(1961), 209–210.

[SS62]   G. Segrè and A. Silberberg, *Behaviour of macroscopic rigid spheres in Poiseuille flow.* J. Fluid Mech. **14**(1962), 136–157.

[SHJ03]   P. Singh, T. Hesla, D.D. Joseph, *Distributed Lagrange multiplier method for particulate flows with collision.* Int. J. Multiphase Flow **27**(2001), 1829–1858.

[Ste57]   K. Stewartson. *On asymptotic expansions in the theory of boundary layers.* J. Maths Physics **36**(1957), 173–191.

[Tra90]   G.L. Trainor, *DNA sequencing, automation and the human genome.* Anal. Chem. **62**(1990), 418–426.

[Tur99]   S. Turek, *Efficient solvers for incompressible flow problems: an algorithmic and computational approach.* Springer, Heidelberg-Berlin-New York, 1999.

[TWR03]   S. Turek, D. Wan, L. Rivkind, *The fictitious-boundary method for the implicit treatment of Dirichlet boundary conditions with applications to incompressible flow simulations.* Challenges in Scientific Computing, Lecture Notes in Computational Science and Engineering, Vol. 35 (2003), Springer, 37–68.

[Tsy98]   S.V. Tsynkov, *Numerical solution of problems on unbounded domains. a review.* Appl. Numer. Math. **27**(1998), 465–532.

[Tsy99]   S.V. Tsynkov, *External boundary conditions for three-dimensional problems of computational aerodynamics.* SIAM J. Sci. Comput. **21**(1999), 166–206.

[UT92]   S.O. Unverdi and G. Tryggvason, *Computations of multi-fluid flows.* Physica D **60**(1992), 70–83.

[VC76]   P. Vasseur and R.G. Cox, *The lateral migration of a spherical particle in two-dimensional shear flows.* J. Fluid Mech. **78**(1976), 385–413.

[VC77]   P. Vasseur and R.G. Cox, *The lateral migration of spherical particles sedimenting in a stagnant bounded fluid.* J. Fluid Mech. **80**(1977), 561–591.

[WT06]   D. Wan and S. Turek, *Direct numerical simulstion of particulate flow via multigrid FEM techniques and the fictitious boundary method.* Int. J. Numer. Meth. Fluids **51**(2006), 531–566.

[WBL⁺04]   J. Wang, R. Bai, C. Lewandowski, G.P. Galdi, and D.D. Joseph, *Sedimentation of cylindrical particles in a viscoelastic liquid: shape-tilting.* China Particuology **2**(2004), 13-18.

[Wei73]   H.F. Weinberger, *On the steady fall of a body in a Navier-Stokes fluid.* Proc. Symp. Pure Mathematics **23**(1973), 421–440.

[Wes92]   P. Wesseling. *An introduction to multigrid methods.* Wiley, Chichester, 1992.

[WFS83]   J.C. Wigle, J.P. Freyer, R.M. Sutherland, *Use of a sedimentation column to obtain uniformly sized populations of multicell spheroids.* In Vitro **19**(1983), 361-366.

[Wit02]   P. Wittwer, *On the structure of stationary solutions of the Navier-Stokes equations.* Commun. Math. Phys. **226**(2002), 455–474.

[Wit03]   P. Wittwer, *Supplement: On the structure of stationary solutions of the Navier-Stokes equations.* Commun. Math. Phys. **234**(2003), 557–565.

[Wit05]   P. Wittwer, *Leading order down-stream asymptotics of stationary Navier-Stokes flows in three dimensions.* J. Math. Fluid Mech. **7**(2005), 147–186.

[WH05]   P. Wittwer and F. Haldi, *Leading order down-stream asymptotics of non-symmetric stationary Navier-Stokes flows in two dimensions.* J. Math. Fluid Mech. **7**(2005), 611–648.